In Situ Study of Polymorphism and Melting of Metals and Compounds under Extreme Conditions of High Pressure and High Temperature

Submitted in partial fulfillment of the requirements for the degree of Doctor of Philosophy at University College London.

December 2012

Richard Briggs

Declaration

I hereby declare that the work described within this thesis is entirely my own, except where specifically acknowledged in the text.

Richard Briggs – Thesis submitted December 2012

Abstract

This thesis presents the experimental investigation of structure and melting of three important materials under extreme conditions of high pressure and high temperature. The melting points of elements and compounds are of fundamental importance for the study of planetary interiors and for fundamental and applied physics. The high pressure apparatus used in this thesis is the diamond anvil cell, which has been used to reach pressures of up to 137 GPa and temperatures up to 6000-7000 K *via* laser-heating techniques. The melting point has been determined at high pressure by the first onset of liquid scattering in X-ray diffraction patterns that are collected *in situ*. At temperatures towards the melting point, important information on the crystalline state of these materials has been extracted.

The polymorphism of Sn has been studied into the megabar range (P > 100 GPa) at room temperature. The equation of state of Sn has been determined up to 137 GPa. A previously unreported structural transformation occurs at 32 GPa into a body centered orthorhombic structure (spacegroup *Immm*). Coexistence of this polymorph with a body centered cubic structure (spacegroup: *Im-3m*) is observed over a wide pressure range. These new findings for this important element are reported within.

The melting relations of Sn have been determined to beyond 1 megabar in pressure and reveal a dip in the melt slope followed by a sudden sharp rise between 40 and 70 GPa. High temperature experiments using resistive-heating and laser-heating in the diamond anvil cell reveal the observation of multiple X-ray diffraction signatures at high temperatures. The results are discussed and overlap with the discoveries from the room temperature investigation of Sn.

TaC and MgO are two important refractory materials and have also been investigated using laser-heated diamond anvil cell techniques combined with *in situ* synchrotron X-ray diffraction. TaC has the highest ambient melting temperature of any binary compound. MgO constitutes approximately 37 % of the Earth's lower mantle and the melting temperature as a function of pressure can provide us with information on the melting behaviour, phase relations and rheology of the Earth's lower mantle. The results and their impact on current high pressure research are discussed.

Table of Contents

Appendix A: List of Publications:

List of Figures

List of Tables

Table of Abbreviation

ADXRD	Angular Dispersive X-ray Diffraction
APS	Advanced Photon Source
AWE	Atomic Weapons Establishment
CCD	Charged Couple Device
DAC	Diamond Anvil Cell
DLS	Diamond Light Source
E	Energy
EDXRD	Energy Dispersive X-ray Diffraction
ESRF	European Synchrotron Radiation Facility
ISP	Institute of Shock Physics
LH-DAC	Laser-heated Diamond Anvil Cell
P	Pressure
SXS	Synchrotron X-ray Scattering
T	Temperature
T_m	Melting Temperature
UCL	University College London
XRD	X-ray Diffraction

Units

Å	Ångtroms	($1x10^{-10}$ metres)
cm-1	wavenumber	
˚C	Celsius	
eV	electron volts	
GPa	giga pascal	($1x10^{9}$ pascal)
TPa	tera pascal	($1x10^{12}$ pascal)
K	Kelvin	
Mbar	megabar	($1x10^{6}$ bar)
m	metre	
mm	millimetre	($1x10^{-3}$ metre)
μm	micrometre	($1x10^{-6}$ metre)
nm	nanometre	($1x10^{-9}$ metre)
mW	milliwatt	($1x10^{-3}$ Watt)
W	Watt	

Acknowledgements

First, I would like to thank my supervisor Prof. Paul F. McMillan for all his support, guidance and encouragement during my PhD. I am very grateful for the chance to carry out these studies and for the countless opportunities working in the McMillan research group has given me. I would also like to thank my second supervisor Dr. Furio Corà for his support throughout my PhD and for useful discussions on theoretical papers and results. Thank you to Ms. Melissa Cutler for working with me on all things relating to Sn, I wish you all the best for your own PhD thesis.

A special thank you goes to Dr. Dominik Daisenberger for teaching me everything I know with the diamond anvil cell and for being there with me working well into the night during the many synchrotron runs. You have been an excellent friend since I first moved to London and exceptional counsel during that time. Another thank you goes to Dr. Ashkan Salamat for teaching me the joys of refinement and the depth of data analysis, as well as what it takes to write a scientific paper. Thank you to Emma McBride for being an excellent friend and for all the science chat during the last few years. I would like to acknowledge in no particular order those who have helped within the McMillan research group Dr. Ana Bélen Jorge, Dr. Edward Bailey, Dr. Raul Q. Cabrera, Dr. Aisha Rahmen and Dr. Katherine Woodhead.

A personal thank you to my friends from office 320 of old (Leon Cavanagh, Stuart Turner, Simon Jacques); office 320 of new (Elspeth Latimer, Emma Newton, Nadia Karim, Mark Fields); and the many new additions who are too many to name. I'd also like to extend this thank you to others within the chemistry department (Dr. Russell Binions, Ralph Leech, Michael Ward, Sofia Elouali, Anna Roffey, Penny Carmichael). Most importantly from 320 is that chap Michael Warwick for bringing the best out of me always.

To all my close friends who have supported me over the years I thank you all with the credit you deserve: James, Sal, Luke, Gill, Esta, Scott, Jó, Claire, Hayley, Lisa, Will, Ceri, Johnny, Shaz and Pierre, Sarah, Christine, Fergy, Mark and Karen.

I am especially grateful to Ms. Alice Pyne for her love and support and for helping me through the last year of my PhD and my time in London. Thank you.

I would like to dedicate this thesis to my family Gary, Sandra and Lauren. I could not have done it without your love and support. Finally I'd like to pay tribute to my undergraduate lecturer, Tudor Jenkins who sadly passed away as my PhD started. I would not be here without his teaching and wisdom.

Publications

R. Briggs, D. Daisenberger, A. Salamat, G. Garbarino, M. Mezouar, M. Wilson, P. F. McMillan. *Melting of Sn to 1 Mbar.* Journal of Physics Conference Series, **137**, 012035 (2012)

In preparation

R. Briggs, D. Daisenberger, A. Salamat, G. Garbarino, M. Mezouar, M. Wilson, P. F. McMillan. *Unusual melting properties of tin at megabar pressures.*

R. Briggs, A. Belén Jorge, M. Bojdys, P. F. McMillan, *High-pressure structural properties of layered carbon nitrides containing halogens using in situ synchrotron X-ray diffraction*

D. Daisenberger, **R. Briggs**, P. F. McMillan, *High-pressure melting curve of TaC*

D. Daisenberger, **R. Briggs**, P. F. McMillan, *High-pressure melting curve of Xe*

A. Salamat, **R. Briggs**, P. Bouvier, S. Petitgirard, G. Garbarino, D. Daisenberger, A. Dewaele, P. F. McMillan, *High-pressure structural transformations of tin up to 137 GPa*

Chapter 1. **Foreword**

How materials behave under combined conditions of extremely high pressure (P) and high temperature (T) is of fundamental interest to a wide range of scientific research areas, from the study of planetary interiors to the effects of shockwaves on substances following explosive detonation. Even though these conditions can be found occurring naturally, scientists are limited by the instrumentation that can probe these areas (for example, in the deep Earth we are mostly dependent on seismic wave analysis). In the early 1900's, high-pressure apparatus were capable of reaching pressures of up to 2000 times atmospheric pressure (0.2 GPa[1]), significantly smaller than the pressures found at the centre of the Earth (~ 340 GPa). Pioneering work by Percy W. Bridgman pushed the pressure limits of such apparatus to ~ 2 GPa with further development and improvements over the next 50 years bringing high pressure research up towards 10 GPa and beyond [1]. The rapid development of static high-pressure apparatus and the contributions made by Bridgman led to him receiving the 1946 Physics Nobel Prize. One of the most significant advances following Bridgman's work was the introduction of the diamond anvil cell (DAC), a small hand held device that pushed the pressure limits even higher towards 100 GPa [2].

Dynamic high pressure and high temperature conditions can be created from the resultant shockwave following high velocity impacts (usually triggered by an explosive device). Specific P-T conditions are accessed following a shockwave, which are dependent on the initial conditions such as the impact velocity and the initial densities of materials involved. Through the laws of energy conservation and by analyzing the

---

[1] 1 GPa = 9,869.2 atm.

starting conditions and particle velocities of the sample as the shock wave passes through, we can determine the P conditions that have been reached by the shock. The particular P-T conditions that are accessed during a shockwave are known as the shock *Hugoniot*.

The Institute of Shock Physics (ISP)[2] was initiated in 2008 by a contract from the Atomic Weapons Establishment (AWE)[3] to Imperial College London (ICL) to help revive the UK hydrodynamics science community, or the fundamental study of materials under dynamic high P-T conditions. Static high-P research is an essential complement to dynamic shock studies, enabling precise studies under high P-T conditions that cannot be achieved by shock. Static high P-T conditions achieved in the DAC can be used to establish equilibrium phase relations and study structure and bonding properties using a variety of spectroscopy and synchrotron X-ray diffraction techniques. These data can then be used to interpret the results of shock studies and can even suggest new dynamic compression experiments. University College London (UCL) was designated as a spoke institution of the ISP in 2009 to develop static high-P-T studies using laser-heated DAC techniques, specifically looking at melting studies of critical materials. These experiments become increasingly important when recreating the conditions found following nuclear detonation, as part of the UK's progressive work for the stewardship of its nuclear stockpile.

The determination of melting points of elements and compounds up to and beyond pressures in the megabar (1 Mbar = 100 GPa) range is of fundamental importance for planetary sciences and fundamental physics. The melting temperatures (T_m) as a function of P can tell us vital information on the properties of an element / compound. Alongside melting, it is important for us to understand the physical properties of

---

[2] http://www3.imperial.ac.uk/shockphysics

[3] http://www.awe.co.uk

materials over a wide P-T range, with underlying solid-solid phase transitions having an important effect on the shape of the melting curve and the behaviour of the material. As an example, the melting temperature of the lower mantle is assumed to lie near a ternary eutectic in the MgO-SiO_2-FeO system [3]. By understanding the melting curve of these three important minerals we can determine the melting behaviour, phase relations and rheology of the lower mantle. To reach these extreme conditions experimentally, dynamic shock techniques have led the way [4]. However, the high temperatures generated during a shock usually only allow us to look at one particular area of the melting curve that is heavily dependent on the Hugoniot conditions reached during shock compression. An alternative method to studying the melting relations is by *ab initio* calculations of the solid-liquid equilibrium conditions [5]. In this case the large numbers of atoms that are required to correctly represent the equilibrium between solid/liquid phases makes the resulting calculations computationally expensive.

In the DAC, melting can be detected by several methods: (1) by looking for abrupt changes in the absorption of the laser radiation; (2) by detecting changes in the reflectivity of the sample; (3) by heating to specific temperatures and visually look for signs of melt afterwards; (4) observing abrupt changes in resistivity. However, there exist two stand out techniques that have been used for the determination of the melting point: optically determined laser speckle experiments [6] and synchrotron X-ray scattering (SXS) experiments [7,8]. In laser speckle experiments an incident laser (e.g. 514.5 nm Ar^+) is focused upon the surface of the sample, creating an interference pattern between the scattered coherent beams due to the surface roughness of the sample. Continuous motion of this speckle patterns is inferred as the melting point due to a molten sample. However, there is no way of studying the sample *in situ* for chemical reactions with the sample and environment. In SXS melting experiments, the crystalline structure of the sample is followed upon increasing the laser power up until the point of melting. Liquid S(Q) / diffuse scattering are reliable indications that the sample has reached a liquid state, with the melting point determined by the first observation of diffuse scattering in the X-ray patterns.

The materials investigated in this thesis have been chosen due to their particular importance and potential impact to the high-pressure community. The SXS method for studying melting relations relies upon the successful award of synchrotron time following a call for proposals that are sent twice a year. An academic panel reviews each proposal for scientific merit, experimental methods that are realistic and for high impact results. Sn was chosen as the first target metal to study as it has high strategic value as well as important bonding effects due to its position in the periodic table, straddling the boundary between semiconducting and metallic behaviour. There had been no static high-pressure investigations, using diamond anvil cell techniques, on the melting of Sn at the start of this research programme. The room temperature behaviour of Sn was not well known and would be crucial in interpreting the melt results. The final two materials studied (TaC and MgO) are important refractory compounds that have very high ambient melting temperatures (~ 4000 K). The melting of TaC system uses the same experimental procedure as for the melting of Sn. However, MgO is an insulating material and required a new experimental setup to be implemented with the same procedure and diagnostic for determining melting temperatures. A further introduction to the materials chosen are provide in each of the proceeding chapters.

Chapter 2. **Experimental Methods**

2.1. Introduction

This chapter introduces and discusses the experimental techniques that have been used to carry out the investigations held within. High-pressure conditions have been generated using the diamond anvil cell (DAC), a small device that uses two opposing diamond anvils to compress samples between the anvil tips. DACs can reach the same pressure conditions that are found at the centre of the Earth. Maximum pressures of > 1,000,000 atmospheres (1 Mbar) and temperatures up to and around 6000 - 7000 K have been attained. The components and methods used for the diamond anvil cell are discussed first, including the various ways of generating and determining high pressure and high temperature.

The optical properties of diamond allow spectroscopic techniques as well as X-ray diffraction to be performed *in situ*. However, the very small sample sizes (~ a few μm) require very intense X-rays to ensure strong diffraction signatures that can be used to determine the crystal structure. Specialist user facilities, known as synchrotron radiation sources, generate high energy X-ray light at high fluxes. A description of synchrotron light and the different synchrotrons visited in this thesis follows a section on analytical X-ray diffraction techniques.

2.2. Diamond Anvil Cell

High pressure conditions have been generated using the diamond anvil cell (DAC), a hand held device that was developed in a collaborative effort by Weir *et al.* and Van

Valkenberg [9]. This device followed the pioneering work in high pressure by Percy W. Bridgman [10]. The optical properties of diamond make it an ideal tool for high-pressure techniques, allowing spectroscopic measurements to be taken *in situ*. The DAC works on the principle of 'opposed anvil' designs (Figure 2.1), using much smaller and significantly harder diamond anvils instead of the traditionally used tungsten carbide anvils. Pressure at the tip is much higher than at the back of the anvil as force multiplication occurs through area reduction.

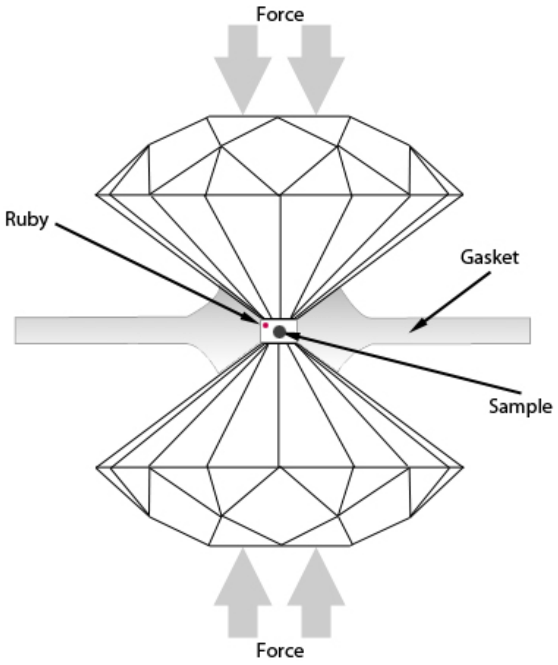

Figure 2.1 Schematic of the diamond anvil cell. Two opposing diamond anvils compress a metallic gasket between the culets (flattened tip) of the anvils, with a small sample chamber containing a sample surrounded by a pressure transmitting medium. A small amount of ruby is added as a pressure gauge.

Experiments using DACs are now reported to reach pressures well into the megabar range [11] attaining perhaps 560 GPa in some cases [12].

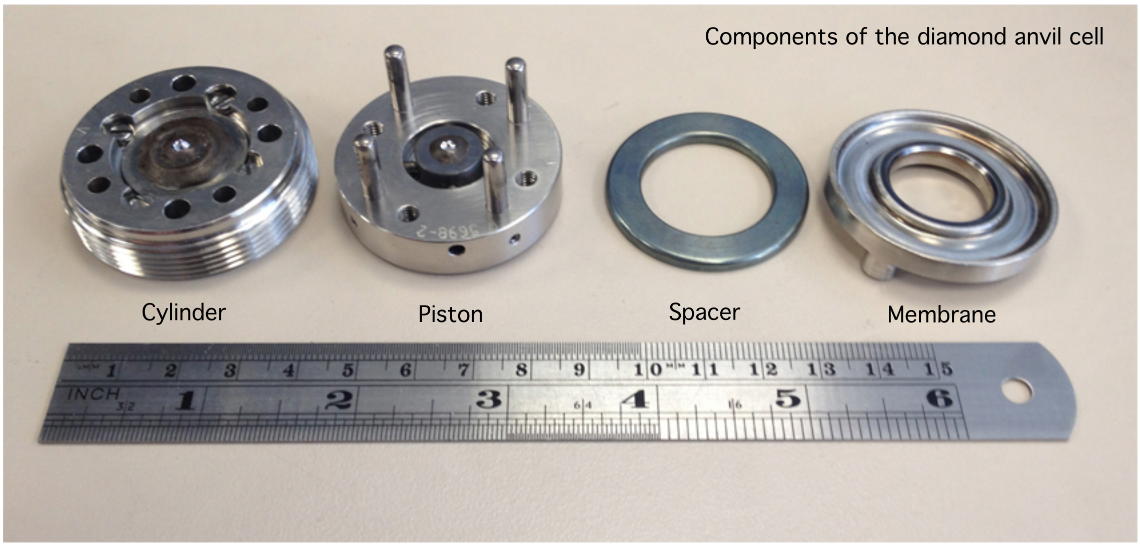

Figure 2.2 Components of a membrane driven diamond anvil cell. The piston connects directly through the cylinder, with the force applied via a gas filled membrane that expands and pushes the spacer against the back of the piston.

The DAC works by compressing a sample between the tips (polished to create a flat surface called the culet) of the two opposing diamond anvils (Figure 2.1). By applying relatively small forces to the back of the diamond, referred to as the table, pressure multiplication is applied through area reduction at the culet. The diamonds sit on backing plates that are fixed in the metal body of the DAC itself. The pressure can be raised either by hand using screws to bring the two parts of the DAC further together (Figure 2.3), or by applying a force through a membrane on one side of the cell (Figure 2.2). The membrane fills with gas that pushes a metallic spacer against the piston component of the DAC, bringing the two diamond anvils together. This is preferred for experiments, since the force is applied uniaxially to the piston. With screw diamond anvil cells, there are 4 screws that can turn imperfectly together and the force in the diamond cell can be spread away from the centre. One method to ensure an evenly applied force is to measure the height of all screws using calipers. Both membrane and screw DACs were used in these studies.

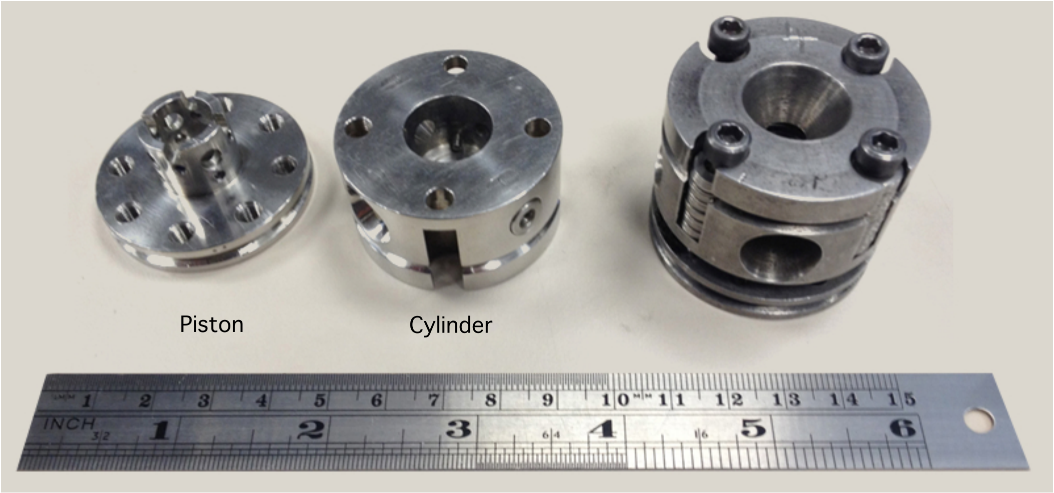

Figure 2.3 Components of a symmetrical screw driven DAC. Four screws (right hand side) are used to drive the piston part into the cylinder part of the DAC.

2.2.1. Diamond Anvils

Diamond anvils must endure severely high strain during high pressure experiments. The type of diamond must be chosen carefully as the 'make-up' of the diamond anvil heavily affects the outcome of experiments. For example, diamonds with impurities can cause optical paths to shift in spectroscopic measurements and can be the centre for fractures under large strain. A useful tool for selecting anvils is the well-established classification of the '4cs' of diamond: *cut, carat, clarity and colour*. *Cost* is also an important characteristic and is often considered the '5th c'. Each of these parameters is important in defining the choice of diamonds for DAC experiments.

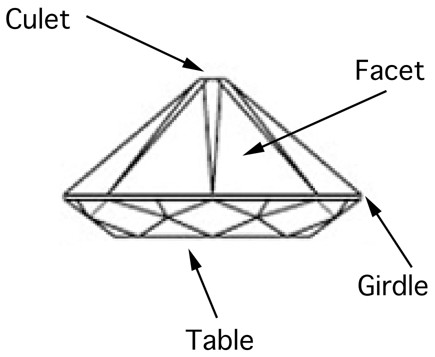

Figure 2.4 Schematic drawing of a diamond anvil.

Over the last 10 years we have seen changes to the *cut* of the diamond anvil and the introduction of the Boehler-Almax design (Figure 2.5) [13]. This cut significantly increase the aperture at the back of the backing plate (Figure 2.6). For X-ray diffraction experiments this greatly improves the accessible 2θ range diffracted from the sample. However, this particular cut initially requires a much larger diamond to polish and cut into this design and so tends to be more expensive. The most familiar cut used over the past 10 years has been the modified brilliant cut, a traditional cut used by many jewelers with the table ground closer to the girdle (the widest part of the diamond) to allow a larger area for force application.

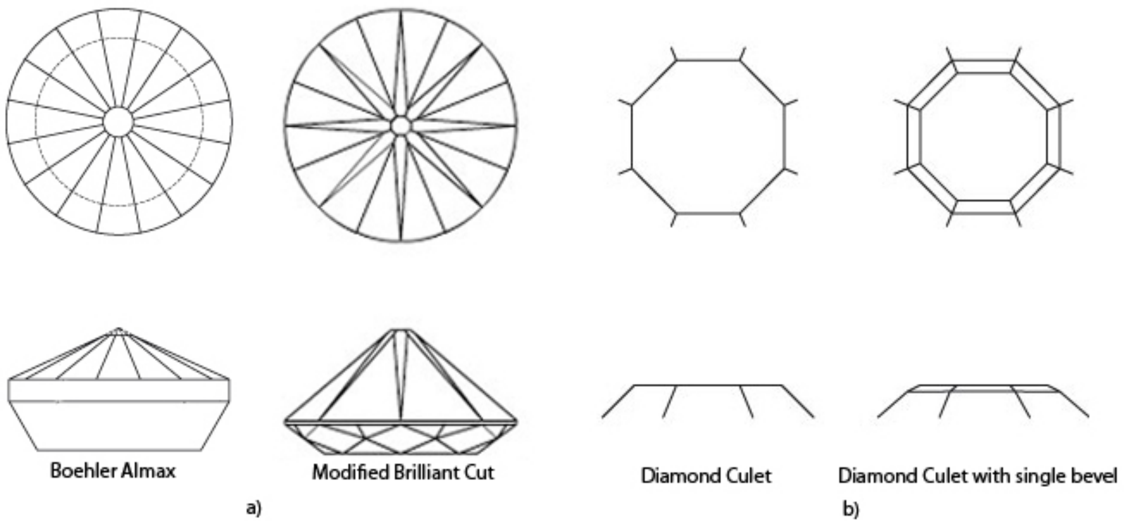

Figure 2.5 Top Panel: Top down view. Bottom Panel: Profile view (a) Schematic diagram of Boehler-Almax and the modified brilliant cuts of diamond (b) Culets of general diamond anvil and single-bevelled anvil.

In DAC experiments the size of the culet defines the maximum attainable pressure, as it is the ratio between the table and culet that defines the pressure magnification. When the force applied to the diamond increases so much that the strain becomes too high, the diamond can break. In my experience I have found that the maximum attainable pressure from a particular culet diameter can be given by the following equation:

$$P_{max}(GPa) \sim \frac{20}{d}, \text{ d = culet diameter in mm.}$$

At very high pressures, the diamond culets begin to bend inwards from the centre (where the pressure is highest). Further attempts to increase the pressure no longer result in a change in pressure at the culet and further application of force will result in diamond failure. A beveled diamond anvil has a second culet polished at a bevel (usually of ~ 8˚) that compensates for this effect (Figure 2.5*b*). As the inner culet begins to contract inwards, the outer bevel becomes flat and there is less strain at the culet tip and the pressure can be increased further.

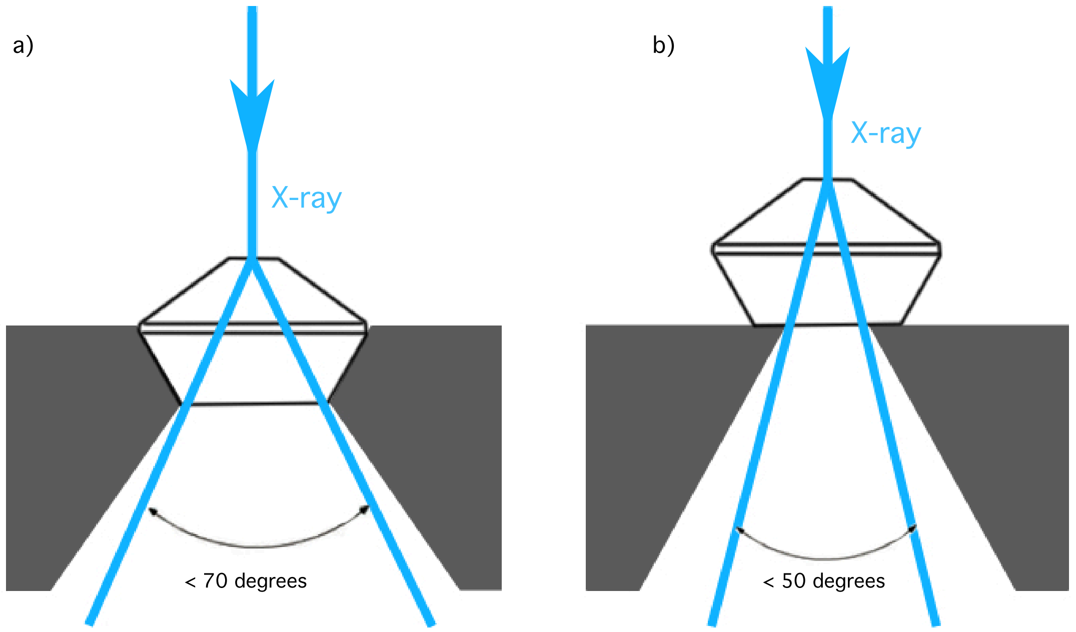

Figure 2.6 Diagram showing the difference between (a) Boehler-Almax backing plates where the diamond sits inside the backing plate increasing the aperture and (b) normal backing plates where the diamond sits on the top with reduced aperture.

The *carat* is a unit of mass that is used specifically for gemstones and pearls (1 carat = 200 mg). Diamonds used in this thesis were usually on the order of 1/3 of a carat with a table size of 4.1 mm and a height of 2.64 mm.

For X-ray diffraction experiments it is important to chose anvils with as few flaws as possible since impurities can lead to parasitic peaks in the X-ray diffraction patterns. Impurities in the diamond can also act as a nucleus for anvil cracks when approaching high levels of strain. The *clarity* of a diamond is a measure of the level of impurities. A diamond clarity chart is shown in Figure 2.7. Flawless (F) and internally flawless (IF) are the most expensive diamonds that show no flaws under 10 times magnification. These stones are therefore the perfect choice for spectroscopic measurements. At UCL, we tend to use very very slightly included (VVSI) or very slightly included (VSI) diamonds, where the inclusions are away from the centre of the diamond and so do not affect spectroscopic measurements.

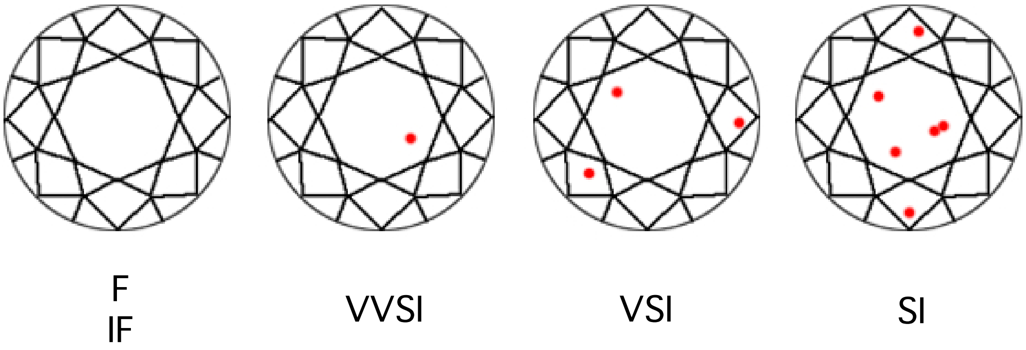

Figure 2.7 Diamond clarity chart showing schematics of flawless (F), internally flawless (IF), very very slightly included (VVSI), very slightly included (VSI) and slightly included (SI). Inclusions are shown in red.

The *colour* of the diamond is defined according to the Gemological Institute of America (GIA) scale. The scale ranges from *D* (completely colourless) to *Z* (pale yellow / brown). These are the most common colours found in naturally occurring diamonds, though blue and pink diamonds exist but are extremely rare and more expensive. The colour of the diamond is a crucial feature of spectroscopic experiments. Any fluorescence from the diamond will increase the background level and could potentially drown out the signal from the sample. Low fluorescence diamonds (Type *IA*) are chosen for Raman experiments. To test the fluorescence an incident green laser (Ar^+) is used to look at the diamond's second order Raman spectra. Figure 2.8 shows two diamonds with different fluorescent signatures. The red line in shows an example of a poor diamond choice, with high fluorescence from the stone, whereas the alternate diamonds spectra (black line) shows a flat level background at a lower intensity. The second order Raman spectrum should also be well pronounced compared to the background. By taking the signal to noise ratio from the second order peak, we are able to assign each diamond we test a ratio (a ratio of 10:1 is a suitably good diamond for Raman experiments).

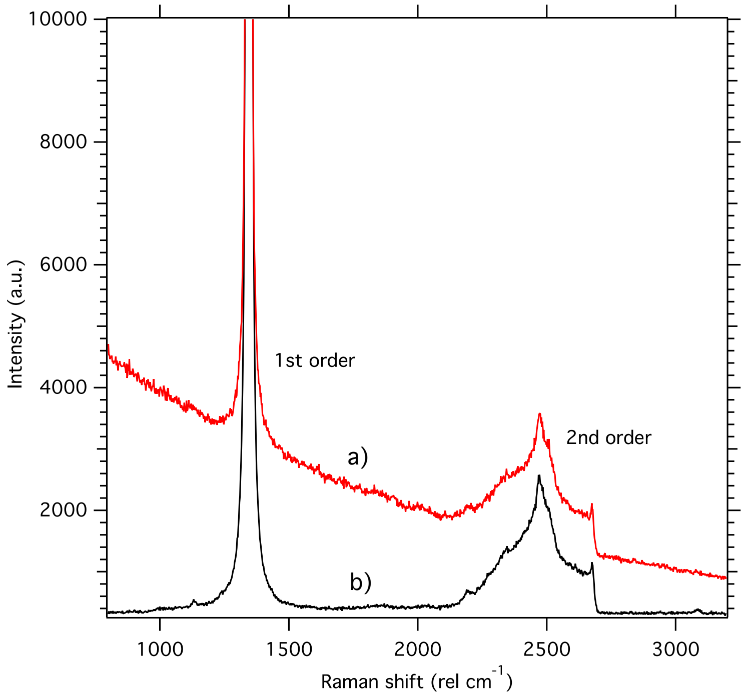

Figure 2.8 Raman spectra of two different Type Ia diamonds. Diamond a) shows a strong fluorescence from the incident laser and would not be a suitable diamond for Raman experiments.

2.2.2. Preparation of the DAC

The DAC is made up of several components that work together to ensure the diamond anvils are perfectly aligned, secured to backing plates to take the strain that is applied and to ultimately raise the pressure in the sample. This section explains the individual components as well as the methods that are used to prepare the DAC and load samples ready for experiments.

2.2.2.1.Backing Plates

Diamond anvils are fixed onto tungsten carbide backing plates using a high temperature epoxy compound (Hysol 9437). This particular epoxy ensures the diamonds remain fixed even at very high temperatures, which they may experience in resistive and laser heating experiments. Other epoxies, such as STYCAST, are used to glue diamonds for room temperature and also low temperature experiments. When gluing the diamond, it is essential that the culet of the diamond anvil is perfectly centred over the aperture of the backing plate. This ensures one can maximize the accessible angle for experimental measurements without the backing plate cutting out a portion of the signal. A mounting device is used to centre and maintain the position of the diamond and backing plate during glueing. It is essential that both the backing plate and back of the diamond are cleaned thoroughly. Any dust particles or dirt remaining on the diamond can be a nucleus for diamond fracture at very high P. Gluing of Boehler-Almax diamonds is significantly easier since the diamonds are cut to sit perfectly inside the backing plate (Figure 2.6) and no centring is required. However, the anvils can tilt slightly in the backing plates and it must be ensured that they sit evenly.

The main role of the backing plates is to provide support to the diamonds. The opening in the backing plate defines the 2θ range that is accessible for X-ray diffraction experiments. A larger opening improves the 2θ range, however, would not provide enough support to the diamond and the anvil may crack and fracture. The Boehler-Almax [13] design allows the diamond anvils to sit inside the backing plate, increasing the accessible 2θ range to ~ 70˚ (typical backing plates allow ~ 50 degrees) as shown in Figure 2.6.

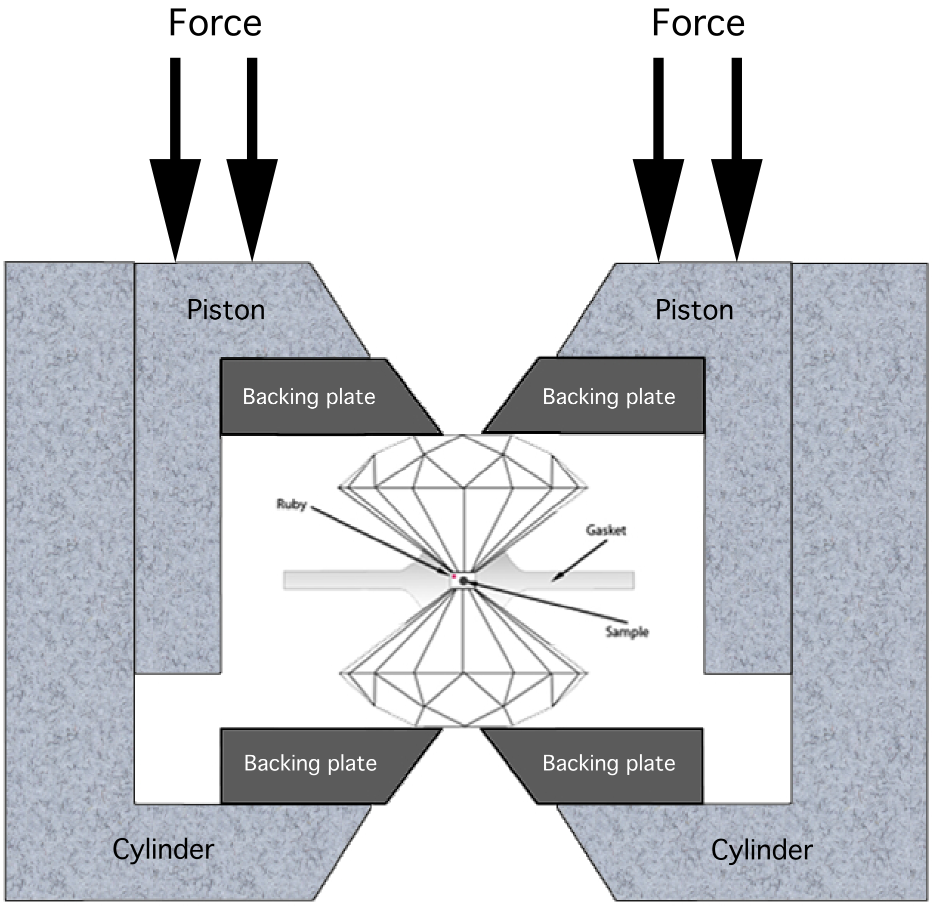

Figure 2.9 Schematic of the diamond anvil cell. Force is applied to the piston component of the DAC, which pushes down into the cylinder bringing the two diamond anvils together.

2.2.2.2.Alignment of the diamonds

After diamonds are stuck to backing plates and introduced into the DAC body, it is essential that the two diamond anvil culets are perfectly aligned and parallel. Any misalignment (through tilt or x- and y- displacement) can cause pressure gradients to build up in the diamonds and anvil failure could occur. Once the culets are aligned we can check to see if they are parallel using two different methods. One method is to squeeze a small amount of silver iodide (AgI) between the culets and observe the phase transition in AgI that occurs at low pressures (Figure 2.10). The change from bright yellow to black is very obvious and spreads from where the two diamonds first make contact. This allows us to identify if the diamonds are parallel (with the phase change from the centre of the culet).

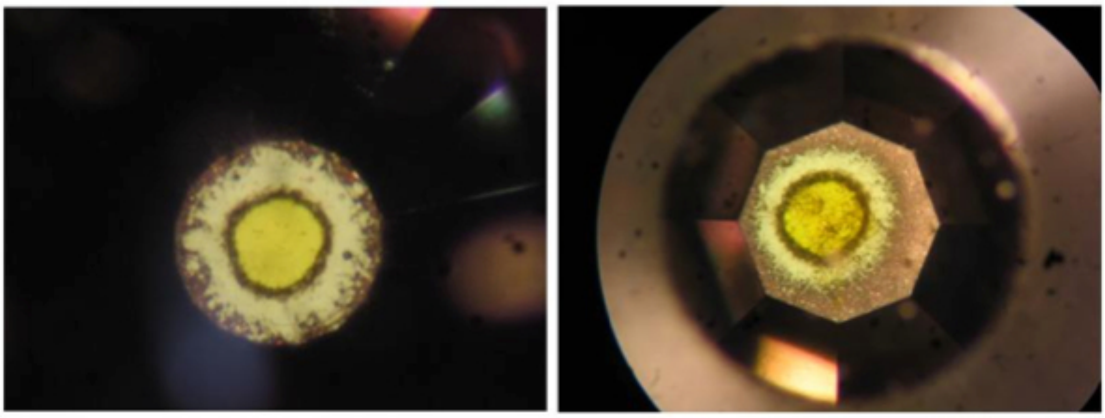

Figure 2.10 Top view through diamonds showing the phase transition in AgI as pressure is increased at the culets. The left photograph shows the transition spreading out from the centre in concentric rings, indicating the diamonds are parallel. The right photograph shows the diamonds are not parallel. Photographs taken by Dr. R. Quesada-Cabrera.

Another method is to apply a small amount of grease to the diamond culets (simply done from the grease from your finger tips) and bringing the diamonds gently together. Birefringence indicates that the diamonds are not parallel, with the source of the fringes an indication that the diamonds are touching from that particular side first (Figure 2.11). The diamonds are parallel once there is no interference pattern observed.

After alignment of the diamonds it is good practice to check the diamonds remain aligned after application of moderate pressure. ‘Dummy’ indents are performed that compress a metallic foil (~ 0.2 mm thick) between the anvils. A small amount of ruby is placed on one anvil to determine the P, achieving up to P = 10 GPa is sufficient to check alignment. Pressure is raised in the DAC (by membrane or screw) and then released back to ambient P. The alignment procedure is then repeated to check if the diamonds are still aligned.

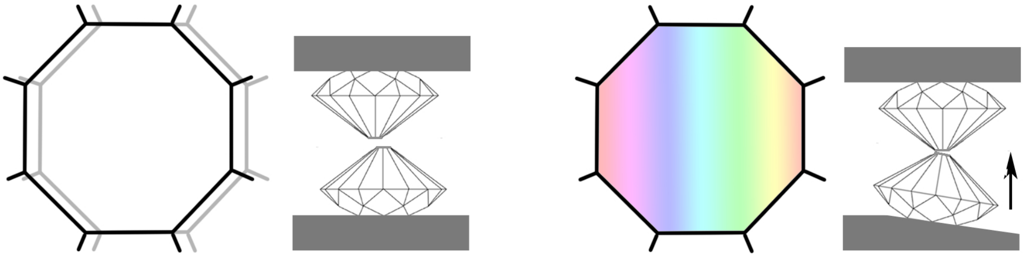

Horizontal alignment

Tilt alignment

Figure 2.11 Alignment of diamonds in horizontal direction (left) and for tilt alignment (right). The anvils are aligned when the birefringence 'rainbow' disappears and the culets overlap perfectly.

2.2.2.3. Gasket

Though diamond is the hardest naturally occurring material it is also very brittle. A slight shock when two diamonds are in contact with each other can cause fractures in one or both anvils. A metallic gasket is used to prevent the two diamonds from touching. The development of the metallic gasket allowed the first DAC experiments to be carried out on liquids and gases. The gasket also extrudes around the anvils and provides extra support at the point where they experience most strain (at the culet edge).

The gasket material should be suitably hard but must maintain the ability to be compressed in order that pressure can increase in the sample chamber. In all of the experiments presented in this thesis, rhenium (Re) gasket material has been used. It is important to pre-indent the gasket before experiments to reduce the flow of gasket material away from the sample chamber and to prevent the gasket hole from opening or collapsing during experiment. The size of the indent depends on the type of experiment being performed, with thinner indents for higher-pressure experiments and larger indents to allow better insulation for laser-heating experiments. To indent the gasket to a predefined thickness, we use a small amount of ruby applied to the diamond to determine pressure versus indent thickness. The pressure in the DAC is then increased.

For an indent of ~ 30 µm, a pressure of ~ 18 GPa is required (for 200 µm diamonds). A load diagram can be constructed for each diamond anvil size and initial thickness of the gasket material (Figure 2.12).

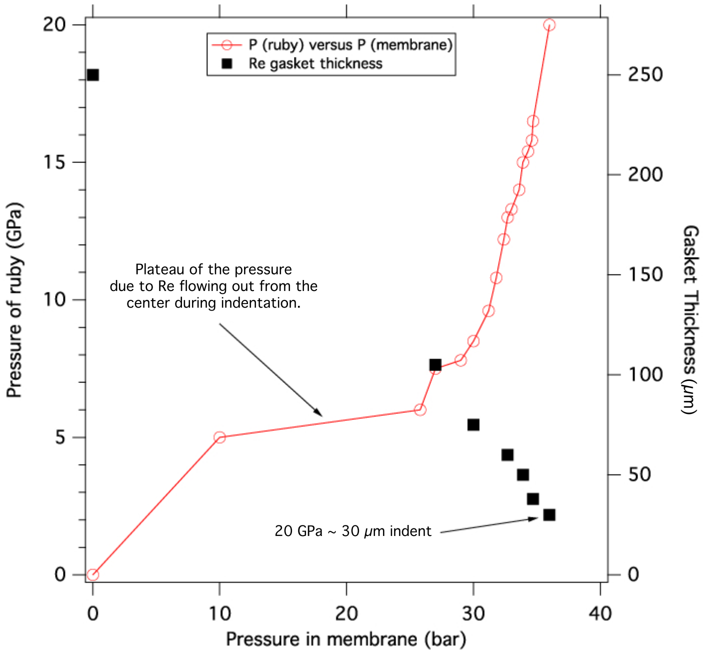

Figure 2.12 Load diagram for a rhenium gasket of initially 250 µm thickness. By increasing the pressure in the membrane of the DAC, pressure increasing and compresses the gasket. Between 10 and ~ 23 bar Re flows easily from the centre before behaving uniformly with increasing pressure.

The drilling of the gasket to create a sample chamber is an important process of DAC preparation. A hole too large may not allow the DAC to reach the highest pressures one aims for. A hole too small may cause X-ray contamination of the gasket material in the diffraction patterns. As a general guide a hole of approximately one third to one half the size of the diamond culet should be used. For gas loadings the hole shrinks by up to 50% and so the initial hole of twice the required size must be drilled. Holes are drilled using a spark eroder (where an electric discharge produces a spark which melts through the metal) or using a laser drill (that melts the gasket as it's rotated in a perfect circle).

For smaller hole sizes, laser drilling is the more reliable method for ensuring the hole is in the centre of the indent and of correct size.

2.2.2.4. Loading of the sample

With the diamonds aligned and gasket prepared and drilled accordingly, the sample can be loaded into the sample chamber. Powdered samples are initially ground into a fine powder before being compressed into thin disks using either tungsten carbide cubes or between two diamond anvils with large culets. This creates a foil with thickness of between 5 and 10 μm. Using micro tipped needles one can break the foil apart into smaller pieces of appropriate size for loading into the sample chamber. Typically a 15 x 15 x 5 μm^3 sample is preferred. The size of the sample should cover approximately half of the gasket hole but should be kept away from the gasket. Figure 2.13 shows a top down view of the gasket and sample chamber as viewed through a microscope.

Due to the small size of the samples it is critical that samples that are air or moisture sensitive are loaded in an inert atmosphere. A glovebox is a sealed container that is designed to contain an inert atmosphere (usually N_2 or Ar) following removal of oxygen and water (conditions inside glovebox are typically O_2, $H_2O < 0.1$ parts per million). Gloves are attached to the glovebox to allow the manipulation of samples and tools in the glovebox by the user. For diamond anvil cell experiments a specially modified glovebox must be used to accommodate microscopes and stages for sample loading (Figure 2.14).

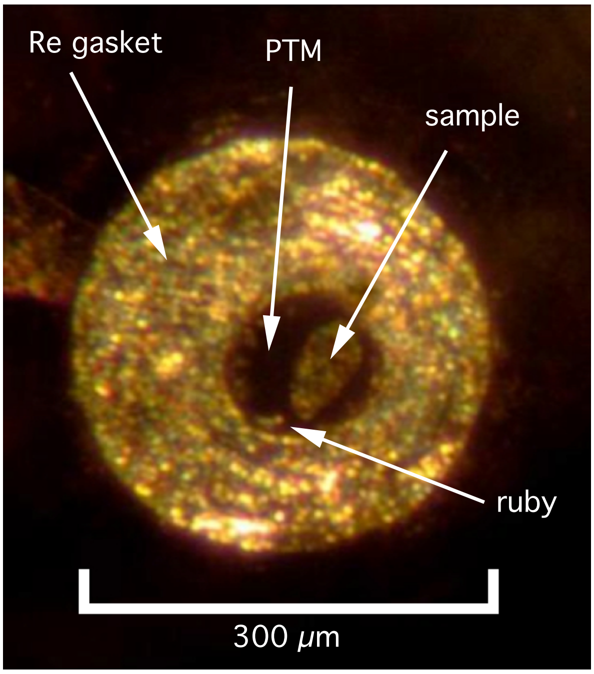

Figure 2.13 Birds eye view of the gasket and sample chamber. The sample has migrated slightly to the right during the loading process and is surrounded by the pressure-transmitting medium, which compresses the sample inside the sample chamber.

Figure 2.14 Glovebox at the ESRF. The right hand side of the box shows the DAC loading area (built in microscope).

For laser-heating loadings, it is essential that the sample is surrounded by insulating material (usually NaCl or KBr). The insulating material is packed into the sample chamber and compressed slightly to ensure the hole is full. A small amount of material is then removed from the centre of the hole to create space for the sample. Using the needle the sample is carefully placed into this space before more insulating material covers the sample and the cell is then closed.

When loading gases into the DAC as pressure transmitting medium, a different loading strategy is required for laser heating experiments. To keep the sample away from the diamond culets it is positioned on a triangle of ruby spheres during gas loading. This is sufficient to allow the gas to fill the chamber and surround and isolate the sample from the culets.

2.2.2.5. Pressure Transmitting Medium

The pressure-transmitting medium (PTM) is a material that is contained in the gasket hole, which surrounds the sample. There are several features required of a PTM, these include: hydrostaticity, chemical inertness, high compressibility, high softness and simple crystal structures to avoid contamination of X-ray diffraction lines from the sample. Some example materials that fulfill these requirements are the noble gases helium, neon and argon.

Hydrostatic conditions exist up to the point at which the pressure medium no longer support shear stress. Above this hydrostatic limit we expect to see pressure gradients in the sample chamber due to deviatoric stress and the sample is said to be under non-hydrostatic conditions. This can lead to anomalies in data collection where stress and shear start to have an effect on phase transitions. Phase transitions can occur at pressures that differ from the true thermodynamic pressure of phase transitions. Helium has one of the highest hydrostatic limits (11.6 GPa at ambient temperature [14]) maintaining a 'quasi'-hydrostatic state even into the megabar range where no pressure gradients are observed [15,16]. Helium is therefore considered the most preferable PTM for equation of state studies and for ensuring a near to hydrostatic environment in the DAC.

Loading a solid or liquid PTM is relatively straightforward; on the other hand, loading gases such as He becomes more difficult. Simply loading He gas into the sample chamber at ambient pressure would not provide a sufficiently dense environment and any application of pressure to the gasket will cause the sample chamber to collapse. Cryogenic loadings of gases like N_2 or Ar have previously been carried out to allow more of the PTM to enter the chamber. However, these loadings can cause unwanted materials to enter the sample chamber as the liquid N_2 or Ar flushes dirt into the sample chamber. New and sophisticated gas loading systems now exist that take a gaseous sample to high pressure (P ~ 1400 bar) before loading it into the sample chamber, preventing a major collapse of the gasket.

The gas loading system at University College London has been designed and built by Sanchez Technologie.[4] The PTM gas of choice can be filled into two large piston driven pumps at bottle pressure (P ~ 180 bar). The pumps are connected to a pressure bomb (that houses the DAC) by pressure circuits and remote controlled valves (Figure 2.15). The system is designed to work with H_2 as well as other gases such as He, Ne and Ar. By driving the piston and decreasing the volume in the chambers, the chosen gas is taken to high pressure (max P ~ 1500 bar). A small gap between the sample chamber and the top diamond allows the gas to fill into the sample chamber and a ΔP is generated between the chamber and the DAC membrane, which then closes the cell trapping the gas in the sample chamber. The system maintains this difference in

---

[4] Sanchez Technologie, ZA de l'Orme, BP37, 95270, Viarmes, France

pressure as the piston cylinders approach ambient pressure, leaving positive pressure in the membrane. A microvalve attached to the membrane allows us to preserve the membrane pressure and keeps the PTM trapped inside the sample chamber. The ΔP should be generated such that the DAC closes and traps the PTM but does not generate high pressures in the sample chamber. For equations of state studies pressures close to ambient P are ideal to extract an accurate V_0 value. Starting pressures using the gas loading system tend to be between 0.2 and 0.8 GPa.

Figure 2.15 Sanchez Technologie gas loading system at UCL. The two pistons take a chosen gas (e.g. He) to high pressure (~ 1400 bar) and into the DAC. The system then closes the DAC and brings the surrounding cylinders to ambient pressure, trapping the gas inside the DAC sample chamber.

Melting experiments require a PTM with an adequately high melting point, usually higher than the melting point of the sample we wish to investigate. Alkali halides (NaCl, KBr, etc.) have been used as general PTM for some time, though are now becoming increasingly important for melting experiments due to their high melting points. Equation of state studies on the alkali halides are well established and are an ideal tool for assisting with determining pressures in the diamond cell during X-ray diffraction experiments [17,18].

2.2.3. Heating techniques

To generate high temperatures in DAC experiments two main techniques are used: resistive heating and laser heating. Resistive heating techniques are divided into internal (using heaters that are fabricated onto the anvils) or external (using heaters that raise the temperature of the whole gasket & sample area). Laser-heating techniques use incident IR or near IR lasers that couple with the sample directly. The limit of resistive techniques is < 3000 K with laser heating achieving up to 6000-7000 K.

2.2.3.1.Resistive Heating

Resistive heating (RH) requires specialized DACs that are designed to accommodate furnaces into the body of the DAC itself. The upper temperature limit of RH-DAC experiments is around 3000 K [19], though most cells work in the RT to 1500 K temperature range. The temperatures generated through resistive techniques are much more stable than laser-heating methods with homogenous heating across the whole sample area and stability through direct monitoring and control over the voltage applied to the furnace. Recently, resistive heating materials have been fabricated directly onto the diamond anvils, which provide both internal resistive heating < 3000 K and resistivity measurements to be taken from the sample [20].

At UCL we use the Diacell®HeliosDAC (M7G) which is a membrane driven DAC that uses an external ceramic furnace for generating temperatures towards 1000 K. A reducing gas mixture (for example, 5 % H_2 / 95 % Ar) must flow through the DAC to prevent oxidation of the cell components. Traditionally resistive heating experiments used wires wrapped around the gasket or backing plates, through which a current is passed to generate heat [21]. The DAC itself can become quite hot during heating and a special stage was designed so that the cell can be used at the synchrotron without damaging the equipment. The membrane drive allows us to make pressure adjustments without removing the cell from the stage. An externally heating DAC has been used to study the melting curve of the alkali metal potassium (K) below 600 K using synchrotron X-ray diffraction [22].

2.2.3.2.Laser Heating

Laser-heating (LH) is a well established technique for generating temperatures of up to 6000 K [6]. The main requirements for LH are high power, stability and an appropriate wavelength of laser light for sample absorption. The transparency of diamond in the IR region allows the use of continuous near IR lasers such as neodymium doped yttrium aluminium garnet (Nd^{3+}:YAG), neodymium doped yttrium lithium fluoride (Nd^{3+}:YLF) as well as mid IR CO_2 lasers.

Near IR lasers are targeted at semiconductors and metals, which absorb through light scattering mechanisms or through charge transfer. The Nd^{3+}:YAG laser emits with a wavelength of 1064 nm and interacts only with the surface of the sample due to a low penetration depth. It is therefore necessary to build a LH system that incorporates double-sided LH to ensure there are reduced temperature gradients within the sample chamber. This is particularly important when using X-ray diffraction to probe the state of the sample as X-rays interact with the bulk. However, near IR lasers are not absorbed by insulating materials such as MgO. This led to the development of CO_2 LH by Boehler and Chopelas [23]. CO_2 lasers have a much greater penetration depth as a consequence of their longer wavelength (10.6 μm) and tend to have single-sided heating setups.

2.2.4. Temperature Measurements

Measuring the temperature of the sample during heating is crucial. Data collected at high P-T conditions are only valid if accurate P-T measurements can be made. In resistive heating experiments T can be measured directly from the heating element using thermocouples, however, for LH-DAC experiments T is measured by recording the thermal emission spectra of the sample. A variable pinhole is used to select a small area (~ 1-5 μm) for taking measurements at the sample center. This ensures thermal emission spectra are only recorded from the same area as X-ray data. The incandescent light is collected by a spectrometer in the wavelength range usually between 400 to 950 nm. The optical system is first calibrated using a lamp with a known intensity versus wavelength distribution. The pre-calibrated lamp allows us to determine the response curve of the optical system. Once known, we can use the Planck radiation function to calculate T from the signal collected by the spectrometer (Figure 2.16):

$$I(\lambda) = \frac{\epsilon C_1 \lambda^{-5}}{e^{C_2/\lambda T} - 1} C_1$$

where I is the intensity, $C_1 = 2\pi hc^2$, $C_2 = hc/k$ and ε is the emissivity (equal to 1 for a black body). The emissivity is wavelength dependent but is only known for a small number of materials (e.g. tungsten). In high-pressure experiments we assume that the emissivity is wavelength independent. At high pressure this can introduce errors of ~ 100 K near 3000 K.

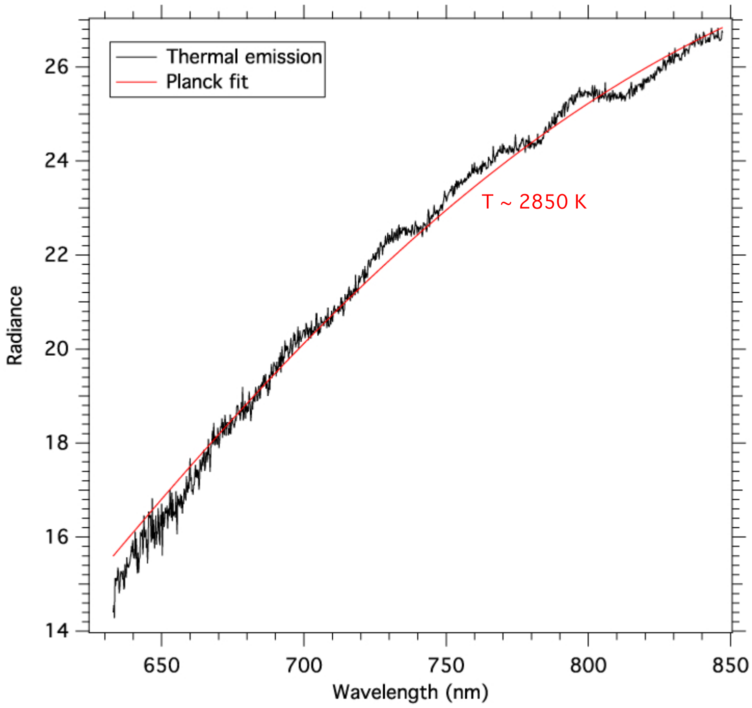

Figure 2.16: Blackbody Planck fit to thermal emission data at T ~ 2850 K.

2.3. Pressure Measurements in the DAC

In the years leading up to 1970 the diamond anvil cell had been through major improvements in its design and experimental capabilities. However, at this time the DAC was not widely accepted as a scientific instrument as there was no well-established way of quickly (and accurately) determining the pressure. The first P measurements were done using X-ray diffraction by determining the volume of a pressure calibrant with a well-known equation of state (determined by shock wave experiments). The first candidate was the NaCl equation of state that had been studied extensively [24-26]. However, the exposure times for diffraction studies resulted in P measurements taken every 15-20 hours. A group of high-P scientists discussed the possibilities and it was suggested that fluorescence spectroscopy could be a viable option. Many samples were tested and exhibited observable shifts with P, but ruby was the most promising. The shift of ruby's main fluorescence peaks became the new standard for determining pressure and is discussed below.

2.3.1. Ruby Fluorescence

Corundum is a thermodynamically stable form of aluminium oxide (α-Al_2O_3) that exists under ambient conditions. The well-known term *ruby* refers to corundum that contains sufficient quantities of chromium (Cr) that give ruby its red colour. The luminescence of ruby has been studied extensively in the 1950s and 1960s since the invention of the first solid state laser [27]. Figure 2.17 shows the calculated energy levels of Cr in ruby as a function of pressure. The R1 and R2 lines (R and R' in figure 2.17) of ruby were found to increase approximately linearly with increasing pressure. With the rapid increase in knowledge of the optical properties of ruby during the 1960's, thanks to the invention of the ruby laser, the natural progression for pressure determination in the diamond anvil cell looked to optical spectroscopy and in particular, the fluorescence of ruby as a function of pressure.

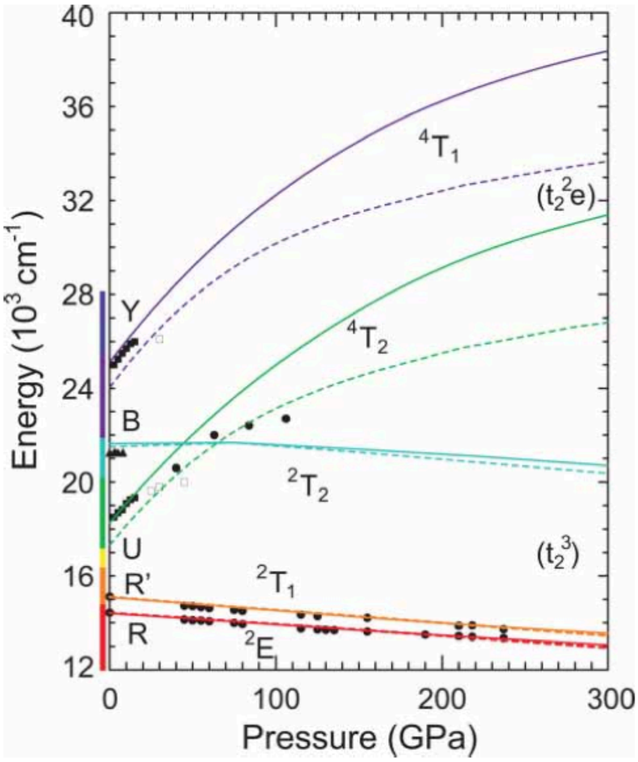

Figure 2.17 Calculated energy levels of Cr in ruby as a function of pressure (from [28]). The R and R' lines shift linearly with increasing pressure.

The ruby scale is one of the most important and commonly used pressure scales in diamond anvil cell research even today over 50 years later. Barnett *et al.* [29] and Piermarini *et al.* [2] first introduced the ruby scale with calibrations against the Decker EOS for NaCl [24]. These two works provided the inspiration for future investigations looking to calibrate and improve the simplistic system that ruby fluorescence is able to offer. The majority of these calibrations are based upon well-established EOS of metals, determined by ultrasonic and shockwave techniques. Static calibrations have also been carried out in which the choice metals are introduced into the DAC and calibrated with ruby. Mao *et al.* calibrated ruby under non-hydrostatic P conditions to up to 100 GPa by comparing with shock determined EOS of different metals [30], following up in 1986 in quasi-hydrostatic P conditions up to 110 GPa [31,32]. As the ruby scale is a secondary P scale (calibrated against other P standards), it is no more reliable than the scales it was calibrated against. However, the ease of use and extended work on calibrating the ruby scale makes it an excellent P standard for P < 1 Mbar experiments. An empirical expression that combines many of the different ruby calibrations into one equation is shown below [33],

$$P = 1870\varepsilon[1 + 5.9\varepsilon],$$

$$\varepsilon = \frac{\lambda}{\lambda_0} - 1$$

where λ is the wavelength of the R1 line at pressure and λ_0 is the wavelength of R1 line at ambient pressure.

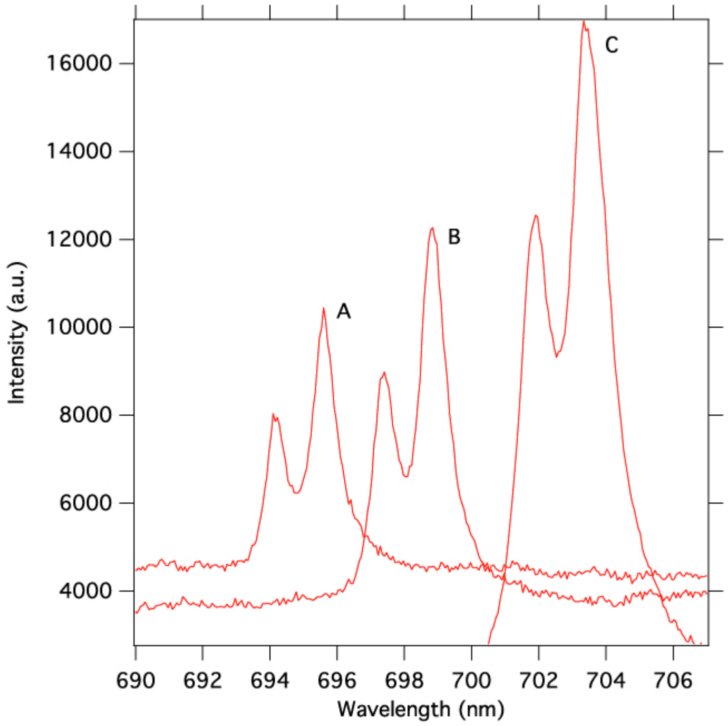

Figure 2.18 Three different spectra showing the fluorescence of ruby. The shift of the R-line increases linearly with pressure. The R1 peak is right peak with larger intensity. A, B and C represent ruby at P = 4, 13 and 26 GPa respectively.

Small ruby grains (~ 1 μm) are sufficient for fluorescence measurements. A series of fluorescence spectra are shown in Figure 2.18 that represent pressures of 4, 13 and 26 GPa. The FWHM and separation of R1 and R2 peaks also give an indication of the hydrostatic (or non-hydrostatic) conditions in the sample chamber. As the pressure environment becomes less hydrostatic, the two peaks begin to merge with the signal becoming broad. In Figure 2.18 the peaks are still resolved separately and indicate a quasi-hydrostatic environment (a PTM of Ar was used). A small amount of ruby powder is typically used, however, modern techniques have allowed the machining of ruby spheres between 2 and 10 μm in size. Ruby spheres are much easier to manipulate into specific positions in the sample chamber. A grid of spheres in the sample chamber can provide important information on the pressure gradients, which may be present due to the type of PTM, by measuring the pressure at different parts of the chamber.

2.3.2. Equations of State

An equation of state (EOS) is the relationship between the volume, pressure and temperature of a particular phase of a substance. Hooke's law specifies that the strain exhibited by a solid is proportional to the applied stress, with the resulting strain equal to the fractional volume change $\Delta V/V_0$. The isothermal EOS under hydrostatic pressure is:

$$P = -K_0 \frac{\Delta V}{V_0}$$

where K_0 is the bulk modulus and V_0 is the volume at ambient pressure [34]. In high-pressure studies we define the bulk modulus along with its pressure derivatives K'_0 and K''_0, where the subscript refers to the bulk modulus evaluated at zero pressure. From Hooke's law it is obvious to see that the bulk modulus changes with pressure and so we must introduce a new equation of state based on finite strain.

The aim of experiments designed to determine the EOS of a solid is to measure the P and V relations directly. There are several EOS available that describe the relationship between P and V using parameters such as V_0, K'_0 and K''_0. The choice of EOS is not so important so long as the EOS accurately describes the P-V relations of the particular sample. However, some EOS models cannot describe the data beyond compressions smaller than $V/V0 < 0.9$ (Murnaghan). The two most regularly chosen EOS are the Vinet [35] and Birch-Murnaghan EOS [36]. The Vinet EOS uses interatomic potentials to give the following EOS:

$$P(V) = 3K_0 \left(\frac{V_0}{V}\right)^{1/3} \left(1 - \left(\frac{V_0}{V}\right)^{1/3}\right) e^{\frac{2}{3}(K_0{}'-1)\left(1-\left(\frac{V_0}{V}\right)^{1/3}\right)}$$

The Birch-Murnaghan EOS to the third order relies on the change in distance between neighboring points during deformation and is shown below:

$$P(V) = 3K_0 f(1+2f)^{\frac{5}{2}}(1+\frac{3}{2}(K_0' - 4)f)$$

$$f = \frac{1}{2}\left[\left(\frac{V_0}{V}\right)^{2/3} - 1\right]$$

where f is the Eulerian strain.

A linearized version of the P(V) relation exists that compares the normalized pressure F (shown below) with the Eulerian strain. This is known as an F-*f* plot and lets us determine K_0 and K'_0 values using a linear fit to the data.

$$F = P[3f(1-2f)^{\frac{5}{2}}]^{-1}$$

If we introduce a material into the sample chamber of a DAC in hydrostatic conditions, we can measure the change in unit cell parameters using X-ray diffraction and map the relationship between the volume and pressure. In this thesis the third order Birch-Murnaghan EOS has been used to fit data for EOS studies, with the linearized F-*f* plot used to fit the data using a linear fit.

To determine pressure in the diamond anvil cell *via* X-ray diffraction we use a well-calibrated sample and use the appropriate EOS to determine pressure from the volume of the sample. Most pressure standards that are used today are secondary pressure scales determined by comparison to primary pressure scales (e.g. Cu, Au, Pt or NaCl) where the pressure is determined from shock-wave experiments. Dewaele *et al.* determined the EOS of several metals (Ta, Au, Pt, Al, Cu and W) up to P > 94 and up to ~ 153 GPa [37]. The improvements in hydrostatic conditions in the DAC have led to the improvement of these secondary pressure scales and ultimately the recalibration of other standards such as ruby fluorescence.

2.3.3. High Pressure Raman systems

For high pressure experiments at UCL we have a dedicated system for DAC experiments that was built in 2000 by E. Soignard and P. F. McMillan [38]. The system was specifically designed for Raman studies (and for ruby fluorescence measurements), but later adjusted to implement a new laser heating setup. An overview of the Raman system is shown in Figure 2.20. An Ar^+ ion laser (514.5 nm) is used, providing up to 50 mW of laser light. This laser emits at other wavelengths along with the strong 514.5 nm line and so a Kaiser® transmission grating is used to transmit all other wavelengths and reflect only the 514.5 nm line. The grating is a holographic grating mounted between two prisms, with the unwanted transmitted light blocked by beam dumps and a light shield following transmission.

One of the most important optics on the high pressure Raman table is the Kaiser® SuperNotch-Plus™ holographic filter (Figure 2.19). This optic acts as a mirror for the incident laser (514.5 nm) if the incident angle is less than 5° but transmits all other wavelengths. This allows us to select only Raman scattered information from the sample and blocking out the much higher intensity Rayleigh scattered light. A second notch filter at the end of the optical path cuts out any remaining Rayleigh signal that the first notch filter could not remove. Al coated mirrors are used to reflect the incident laser path and the transmitted signal from the sample to the spectrometer. The incident laser light is focused onto the sample using a Mitutoyo® objective lens with working distance of 21 mm and magnification of 10x, 20x or 50x. The Raman scattered signal reflects back through the objective, passing through the Notch filters along the optical path to the spectrometer. A confocal spatial filter refocuses the signal onto a variable aperture (where we can select a small μm sized area of the sample and is then made parallel by a second spatial filter. A flip mirror allows us to view the sample chamber and make adjustments to the position and focus of the cell before removing the mirror from the path, allowing signal to reach the spectrometer.

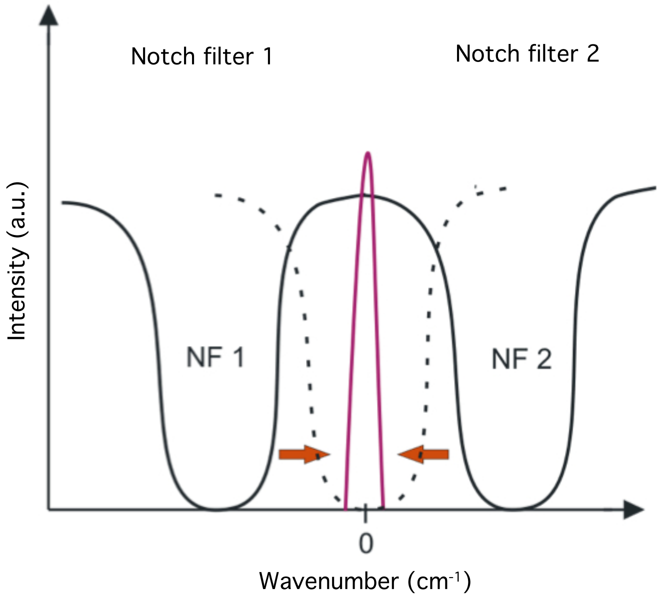

Figure 2.19 Two notch filters are used on the Raman system to block the Rayleigh scattered light from the sample. This is achieved by adjusting the angle, near to 5 °, of each notch filter along the beam path, which shifts the blocked light from the notch filter left or right (arrows) until it blocks the scattered light around 0 cm^{-1} (dash spectrum). Two notch filters are used (NF1 and NF2) to provide a wider range of Rayleigh scattered blocked light. NF1 is shifted to near 0 cm^{-1} from negative wavenumber and NF2 is shifted to near 0 cm^{-1} from positive wavenumber.

The spectrometer (Acton Research SpectraPro® 500i spectrometer) has three possible gratings that define the resolution (and wavelength range) of the measured signal. The highest resolution and shortest range is the 2400 lines/cm grating with a spectral range of 80 cm^{-1}. We use a 300 lines/cm^{-1} grating for measurements such as thermal emission where a wide spectral range is required. The CCD detector is cooled using a liquid nitrogen chamber attached to the spectrometer body. A neon lamp is used to calibrate the pixel number to wavelength for the spectrometer before each experiment, with further calibration of the wavenumber shift using the well-established Raman signal of Silicon (with the most intense peak at 520 cm^{-1}). It is important that the calibration is checked before each experiment due to varying conditions in the laboratory.

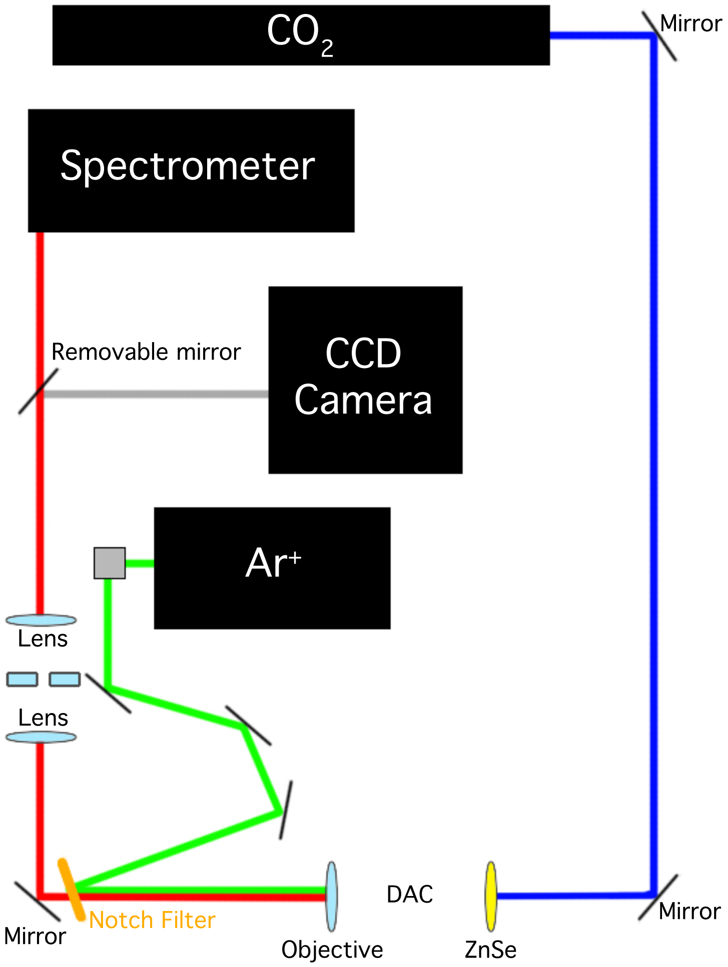

Figure 2.20 High-pressure Raman system schematic including CO_2 laser heating. The green line is the path of the Ar$^+$ laser (514.5 nm), the blue line is the CO_2 laser path and the red line is the reflected optical path that passes into the spectrometer. The notch filter (see Figure 2.19) is shown in orange.

2.3.4. CO_2 laser heating system

The high pressure Raman system also includes the capability for CO_2 laser heating. The CO_2 laser has an infrared wavelength of 10.6 μm and is used to heat oxides, minerals and organic / insulating materials *via* direct coupling of the laser. Since the CO_2 laser is invisible to the naked eye a red diode laser is used to align the laser to the Raman optical path. SiO_2 is usually used as focusing lenses but absorbs the CO_2 laser light and so a ZnSe lens is used instead to focus the CO_2 beam to the sample. The CO_2 laser has a much greater penetration depth than YAG or YLF laser-heating (> 20 μm) and so single sided laser heating is sufficient to heat the sample throughout without large temperature gradients. As shown in Figure 2.20 the CO_2 path comes from the back and so does not interfere with the Raman optics. This makes a very simple setup for laser heating.

2.3.5. Double-sided Nd:YLF laser-heating

In order to study the melting of metals and to ensure that loadings in the diamond anvil cell are successful and heat uniformly, a second laser system was designed and installed at UCL (Figure 2.21). A Nd*:YLF near-IR laser (λ = 1053 nm) is used to couple with metallic samples. Due to the low penetration depth of the near-IR laser, the laser-heating beam is split into two paths that heat the sample from both sides, helping to reduce temperature gradients in the sample. This system was designed with the capability of also performing speckle studies [6]. For speckle experiments, the visible laser (Ar^+) shines upon the surface of the metallic sample and creates a speckle patterns due to the surface roughness of the sample. The image is captured *in situ* from a CCD video camera attached to the computer and time-synced with the spectrometer. Thermal emission data is collected alongside a recorded video of the speckle pattern and we are able to determine the melting point by matching the appropriate timestamp to the onset of melting.

The laser-heating system has a similar design to that used at high pressure beamlines at synchrotron radiation facilities (discussed later) so that heating experiments can be carried out in a familiar environment. This is crucially important to maximize the total amount of time available at the synchrotron and to ensure the samples are known to heat correctly and are ready for melting experiments as soon as beamtime begins.

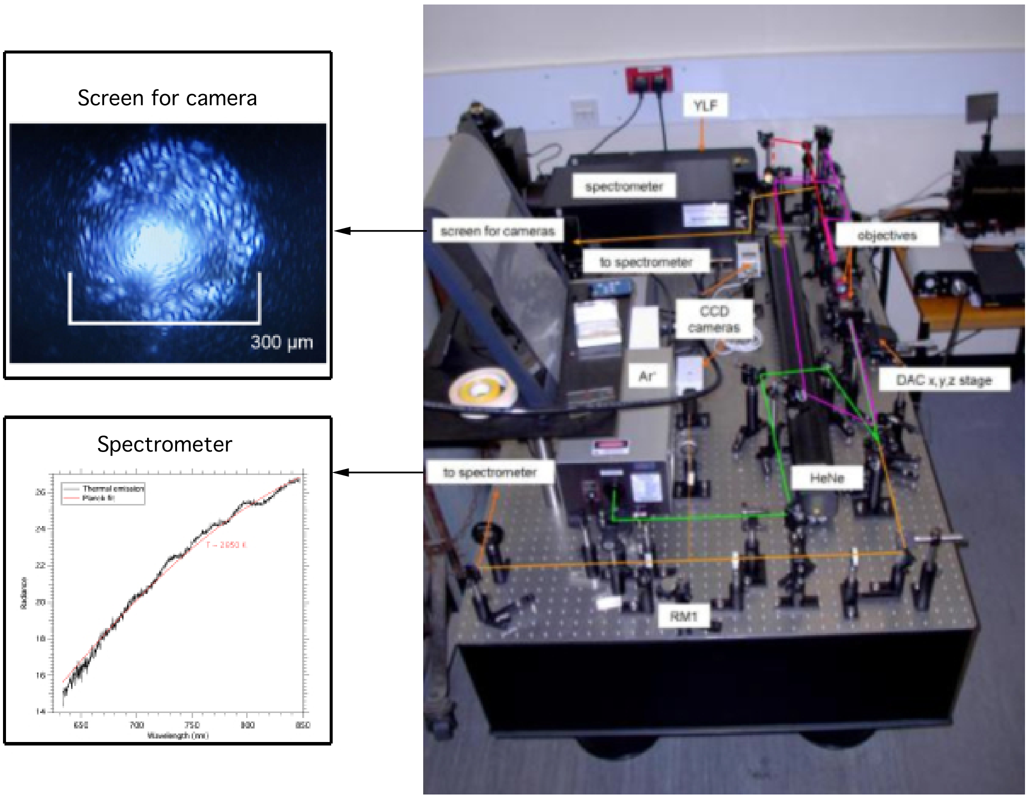

Figure 2.21 Double-sided laser heating setup for speckle experiments. The speckle motion is monitored simultaneously with thermal emission measurements

2.4. X-ray Diffraction

X-ray diffraction (XRD) is a well-established technique for studying the crystal structure of materials [39,40]. Diffraction occurs for all waves and is most pronounced when the wavelength is on the same scale as the distances between diffracting objects. Atomic distances are on the same length scale as the wavelength of X-rays and so XRD is a perfect tool for studying crystals. Research laboratories use X-ray sources to probe samples in large quantities (a few mg) to obtain strong powder diffraction data. However, the intensities of laboratory X-ray sources tend to be low and so exposures can take several hours. In diamond anvil cell experiments sample sizes are significantly smaller and exposures would take several days to provide the same X-ray intensity. Usual laboratory sources (for example, CuK-alpha) are also not suitable for diamond cell experiments as diamond heavily absorbs X-rays of that wavelength (Figure 2.22) [41]. For DAC experiments we therefore require X-ray sources with much higher brilliance and higher energy in order to successfully probe the samples on a more convenient timescale.

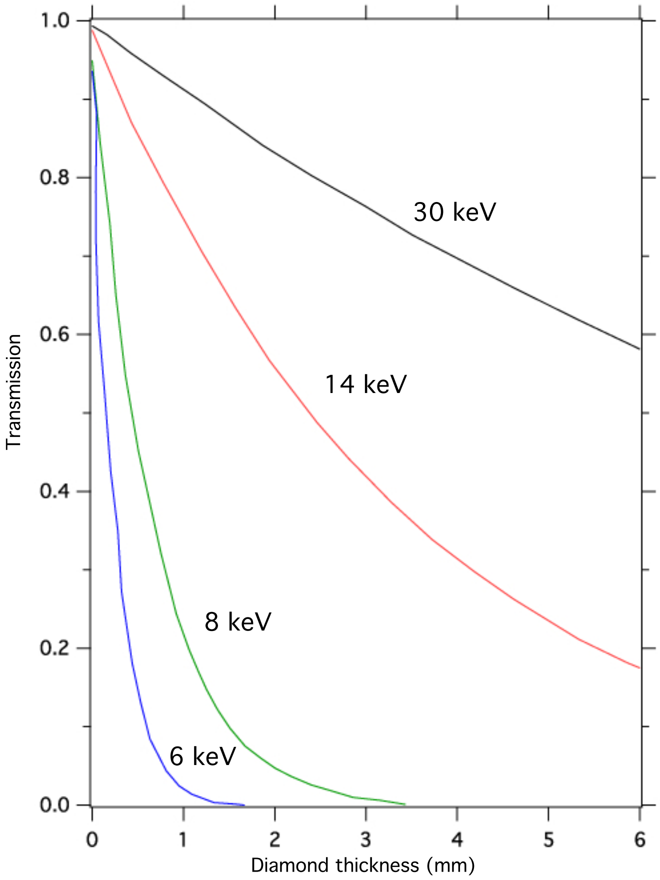

Figure 2.22 Relative X-ray transmissions through diamond of varying thickness for different energies. Lower energy X-rays found in most laboratories are heavily absorbed by diamond of just 1 mm in thickness.

2.4.1. Synchrotron X-ray Diffraction

From electromagnetic theory it is known that accelerating charged particles emit radiation. When electrons (or positrons) are accelerated to relativistic speeds the wavelength of the emitted radiation extends to the high energy X-ray region of the electromagnetic spectrum. This is the principle behind synchrotron radiation facilities, where electrons are accelerated to relativistic speeds by a series of high power magnets. The electrons are generated by an electron gun and accelerated up to very high speeds through a series of three accelerators: the linear accelerator (Linac), the booster synchrotrons and finally the storage ring. ‘Bending’ magnets are used to deflect the electrons thus generating radiation that runs tangential to the path of the electron. The electrons are confined in the storage ring by the strong magnets that are separated by straight sections leading into experimental beamline stations.

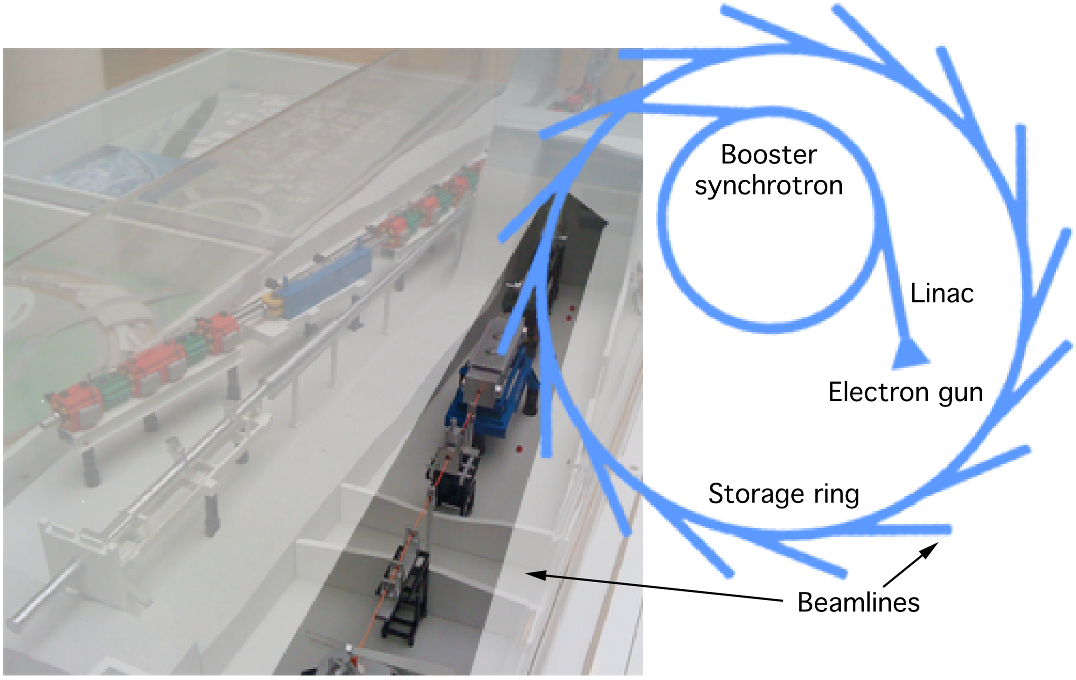

Figure 2.23 Schematic of a synchrotron facility with model beamline following on from the path of the X-rays from the storage ring.

Although the brilliance of the X-rays generated from a synchrotron is already many times greater than from standard laboratory sources it can be improved further by the use of insertion devices. The X-rays produced by synchrotrons can be tuned to higher energies at the individual beamline stations. Typically high-pressure experiments work between 20 and 50 keV ($0.2 < \lambda < 0.8$ Å). Brilliance is approximately defined by the flux per unit area and per unit of opening angle and time. In order to provide suitable brilliance for diamond anvil cell experiments insertion devices are used between the bending magnets of the storage ring. Wigglers [42] or undulators [43] are used that shift the electron path to create a higher X-ray photon energy. Both insertion devices consist of a series of alternating magnetic poles that the electron beam passes through. As the electrons pass through the alternating magnets there is emission from different positions that accumulate to give a significant increase in intensity. The shape of the emission from a wiggler is similar to the emission from the bending magnets. When there are many alternating magnets the emissions from different areas of the wiggler can interfere and provide a coherent beam with a much higher intensity (these devices are known as undulators).

2.4.2. Scattering by crystals

When X-rays pass through a material the photons can be either absorbed or scattered. Scattering occurs when the trajectory of the incident photon changes when encountering the atomic matter. If the deflected photon from the incident beam has the same energy it is coherent (or elastic) scattering. If there is a change in energy, resulting in a change in wavelength, it is known as incoherent (or Compton) scattering. Diffraction occurs when the coherently scattered photons interfere. A combination of all the scattered beams creates a diffraction pattern.

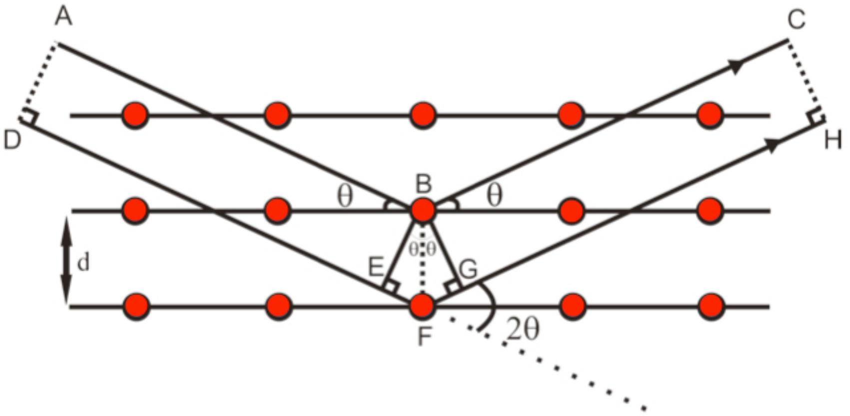

Figure 2.24 Diagram illustrating Bragg's law. Maximum constructive interference between the reflected waves will occur when the path difference is an integer multiple of the wavelength.

The crystal structure can be deduced using Bragg's law of diffraction. The X-rays that undergo constructive interference from the atoms in the crystal lattice give rise to diffraction spots. Bragg's law describes the relationship between the wavelength of the incident beam, the diffraction angle (or Bragg angle) and the inter planar spacing of the crystal. Once the X-ray has been scattered by the atoms in the different planes it travels at a different angle, defined by theta. The incident paths AB and DF are reflected to the paths BC and GH respectively by an angle 2θ and have travelled different distances as a result. This path difference explains the interference effect between reflected waves, as described by:

$$\delta = EF + FG = d\sin\theta + d\sin\theta = 2d\sin\theta$$

Maximum constructive interference between the reflected waves will occur when the path difference is an integer multiple of the wavelength. This is Bragg's law:

$$n\lambda = 2d\sin\theta$$

Diffraction of monochromatic X-rays by a crystal leads to a series of interference maxima at angles 2θ (from the incident beam), which satisfy the Bragg equation. A detector is positioned at a distance far enough away from the sample so that the scattered 2θ angles are suitably separated.

For solving crystal structures single crystals are much better than poly-crystalline powder samples, however there are several reasons why powder diffraction techniques can be preferred. In many cases, samples are simply not available in single-crystal form where as in other cases samples can undergo first order phase transitions with large volume changes where the single crystal does not survive the transformation.

There are two types of diffraction techniques that are available: angle dispersive X-ray diffraction (ADXRD) and energy dispersive X-ray diffraction (EDXRD). In EDXRD the X-ray source is polychromatic (covers a wide range of energies) and diffraction data are collected at a fixed angle and measured as a function of energy. With ADXRD the X-rays are monochromatic and data is measured as a function of theta. There are advantages to both techniques, with EDXRD a faster way of collecting data but with lower resolution.

In this thesis, we show data collected from powdered samples. To reduce the possibility of single crystals in the diffraction patterns, samples should be finely ground. Diffraction by a powdered sample leads to a series of interference maxima in the shape of rings, concentric with the incident beam at values of 2θ that satisfy the Bragg equation (Figure 2.25). The wavelength of the X-rays is known and so using the 2θ values we can determine the interatomic spacing's of the crystal. The unit cell shape and size can then be determined. The relative intensities of the diffraction peaks give information on the position of the atoms with the unit cell.

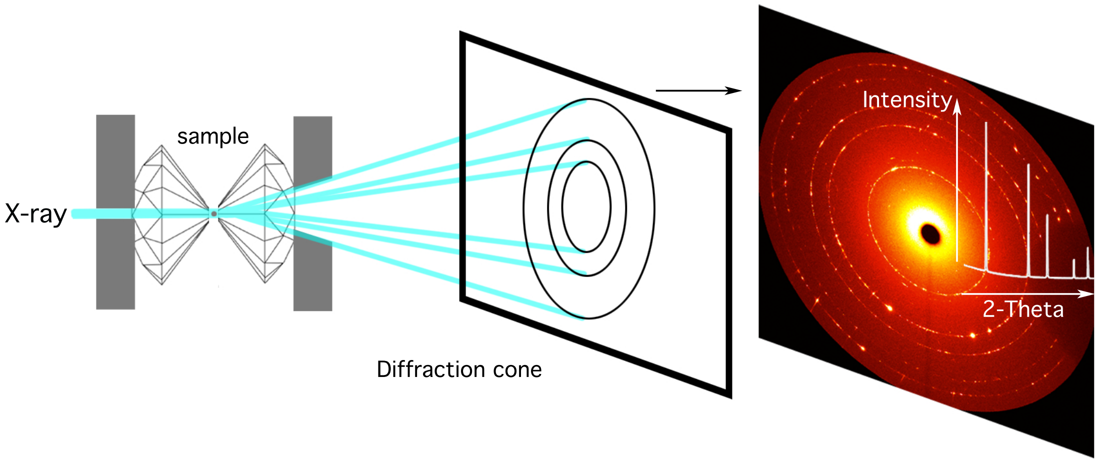

Figure 2.25 Illustration of angular dispersive X-ray diffraction in the diamond anvil cell. The image to the right shows the raw data representing the Debye-Scherrer diffraction rings, with the integrated diffraction pattern overlaid.

2.4.3. Beamlines

For each synchrotron X-ray experiment, a proposal must first be submitted that is reviewed by a committee and beam time is either accepted or rejected based on each scientific case. Usually, between 3 and 5 days of beamtime are provided to undertake and finish the experiments. The proposals must be focused on the experimental capabilities that the particular beamline can offer. For example, DAC melting studies require high flux, micro-focusing and laser-heating setups. Three synchrotrons have been used in this thesis:

- ID27 at European Synchrotron Radiation Facililty (ESRF), Grenoble, France
- GSECARS at the Advanced Photon Source (APS), Argonne National Laboratory, Argonne, IL, USA
- I15 at Diamond Light Source (DLS), Didcot, UK.

In this thesis melting experiments have been undertaken at ID27 & GSECARS, high-P,T experiments using resistive techniques at I15 and room temperature compression experiments up to very high pressures at ID27.

2.4.3.1. I15, Diamond Light Source, Didcot, UK

Diamond Light Source (DLS) opened in the UK for users in January 2007. The extreme conditions beamline (I15) is a dedicated station for high P-T experiments providing high energy and micro-focused X-rays (minimum beam size of 20 x 20 μm^2). A silicon (111) double crystal monochromator is used to provide a monochromatic beam with energies up to ~ 40-80 keV depending on focusing requirements. The focusing is achieved through Kirkpatrick-Baez mirrors that focus the radiation beam down to a large spot size and then focused down further using a collimator. The station is undergoing regular maintenance to implement new upgrades. Currently the X-ray beam is focused to a 20 x 20 μm^2 area using pin holes and does not have the capabilities for micro focusing < 10 μm at this time. This limits the maximum pressure that can be attained without gasket material causing parasitic peaks in diffraction data as the sample chamber in the DAC collapses. I15 now uses a Perkin Elmer flat panel 1621 EN detector (2048 x 2048) but also has a MAR 345 image plate (3450 x 3450 pixels). There are no laser-heating facilities available online at I15 and so we had to rely on resistive heating techniques to perform any high temperature experiments at the station.

2.4.3.2.ID27, European Synchrotron Radiation Facility, Grenoble, France

ID27 is a dedicated extreme conditions beamline that was commissioned specifically for high pressure and high temperature experiments [44]. The beamline has been running since 2006 and operates with a monochromatic beam with wavelength of $\lambda = 0.3737$ Å, though has the capabilities of running in energy dispersive mode. The monochromatic beam has a very high flux of X-rays that is ideal for ensuring short exposure times for rapid collection. The rapid read time of the MAR CCD detector enables diffraction patterns to be recorded every few seconds, an essential feature for looking at the state of a material during melting experiments. Another key component of the beamline is the micro-focusing capabilities, which provides an X-ray spot size of $\sim 2 \times 1$ μm^2 (Figure 2.26). For melting experiments, this allows us to probe the structure of the sample at the exact location of which we collect thermal emission. It also means we can perform mapping of the sample by using a square grid to probe different areas in the sample chamber without scattering from the Re gasket.

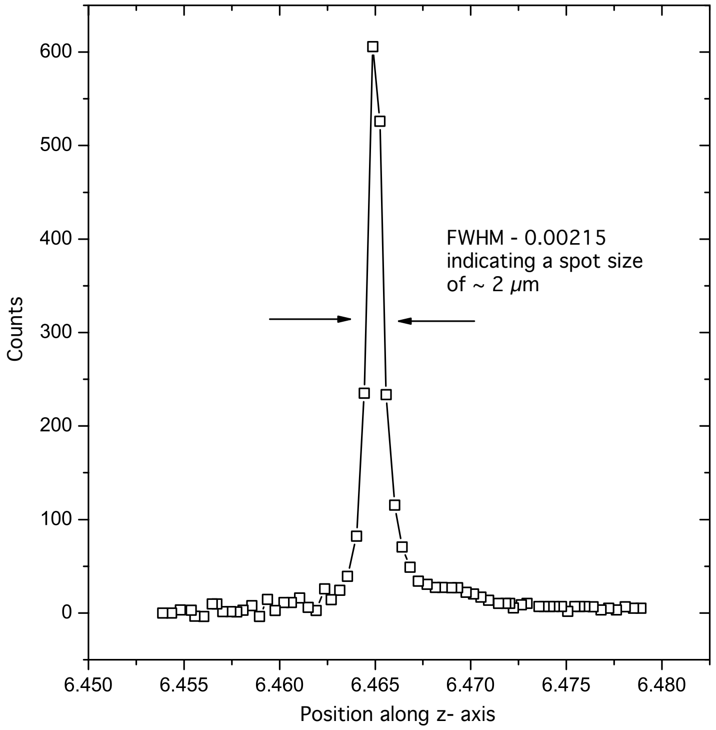

Figure 2.26 FWHM of the X-ray beam. Intensity counts were determined by a diode that scans the pinhole along the z-axis.

To generate the extreme conditions of high temperature the experimental hutch has an inbuilt double-sided laser heating system composed of a high-power diode-pumped Nd-YAG IR laser (Figure 2.27). Both lasers have a capability of producing up to 40 W of laser power each when running in continuous mode ($\lambda = 1.064$ μm). The lasers are guided to the diamond anvil cell, which is held within a water cooled jacket, by mirrors (shown by red paths in Figure 2.27) and are incident upon the sample from an angle of < 20°. The thermal emission signal is collected by specialized collecting optics (guided by the highlighted mirrors in Figure 2.27) and focused onto the spectrometer where the light is wavelength dispersed.

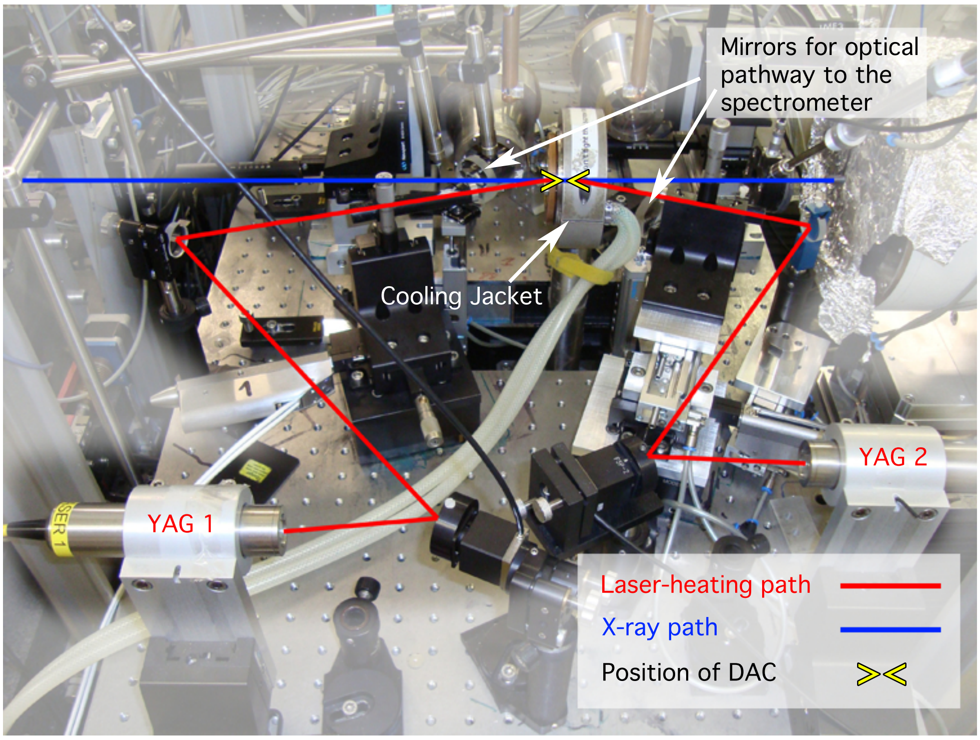

Figure 2.27 Optics bench at the ID27 beamline. Two Nd*:YAG IR lasers (red) are used to heat the sample from both sides and are aligned along the same optical path as the X-ray beam (blue).

2.4.3.3.13-ID, Advanced Photon Source, Argonne National Lab, Argonne, IL, USA

13-ID, or GeoSoilEnviroCARS (GSECARS), is part of the CARS consortium at APS dedicated to extreme conditions research. The station setup is very similar to ID27, ESRF but with the optical path for laser-heating and temperature measurements arriving from 90° to the path of the X-ray before reflecting off a carbon mirror onto the path of the X-ray beam and to the sample (Figure 2.28). The lasers used on the GSECARS beamline are two diode-pumped, single mode fiber lasers that are shaped using specialized beam shaping optics to create two flat top laser heating spots. The beamline is well suited for melting experiments and was used to study the melting curve of Ge up to 40 GPa [45].

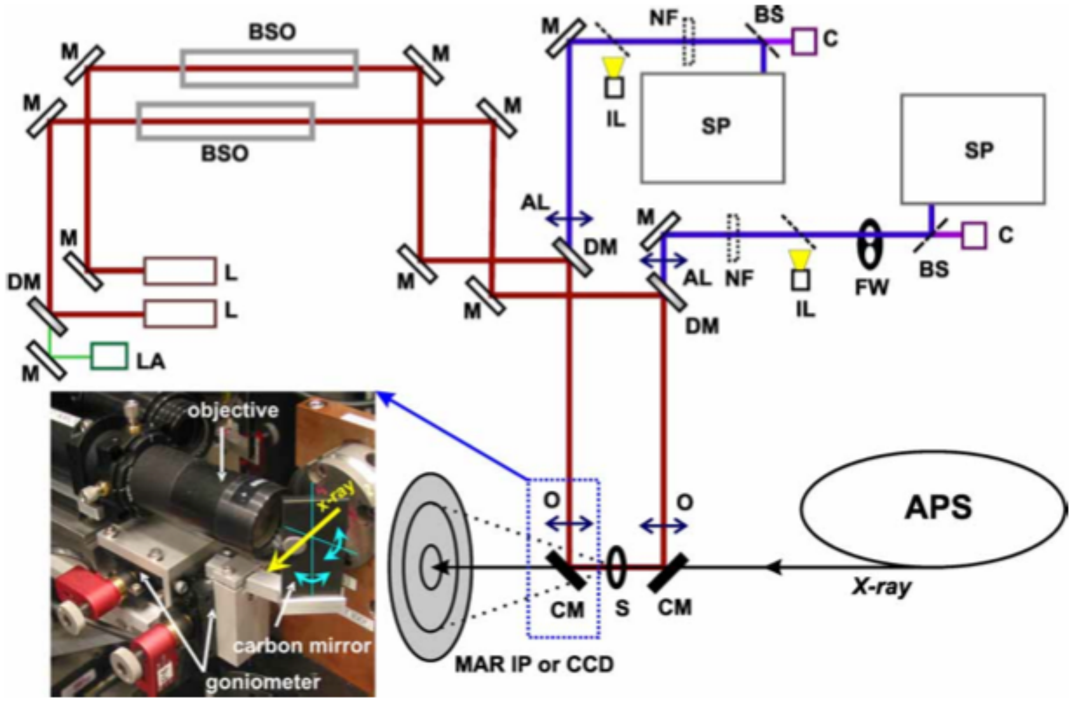

Figure 2.28 Optical schematic of the double-sided laser-heating facility at GSECARS, APS (image taken from [45]).

2.4.4. Data treatment of X-ray diffraction results

Several data processing programs are used to transform the raw X-ray diffraction patterns into useable formats where we can determine the crystal structure of a sample, determine temperatures from thermal emission data or visually looking at full data sets to look for signatures of melting. After collecting XRD data the whole diffraction pattern should be integrated to improve the powder averaging. Fit2D is a data analysis program that has been developed by Andy Hammersley over a number of years at the ESRF [46].

Before any data can be analyzed it is vital to determine the sample to detector distance. This constrains the 2θ range and the pixel to 2θ values that should be used. Moving the detector closer to the sample results in a smaller diffraction cone. By moving the detector away from the sample the diffraction cone is larger and peaks are better resolved (further apart from one another), though potentially cut off any higher reflections in the range. A standard material is used with many well-known Bragg peak positions that can be used to determine the pixel to 2θ calibration. Silicon is often used for this purpose though CeO_2 and $LaBr_5$ have also been used in this thesis.

With the sample to detector distance calibrated the raw data can be transformed into a useable format. Fit2D allows the manipulation of raw data by masking intense spots that greatly add to background signal. Single crystal spots or large diffraction spots originating from the diamond can be masked by polygons and are not included in the powder averaging during integration. Batch processing and macros have been used in this thesis to export diffraction patterns to .chi or .gsas formats for further analysis (though in some cases manual adjustments have been required to export data).

Once we have our integrated XRD pattern we can begin to analyze the data to determine the crystal structure of our sample. If the crystal structure is known, we can move straight to refinement of unit cell parameters using software packages such as POWDER CELL [47] or GSAS / EXPGUI [48,49]. However, indexing of the XRD peaks is good practice for confirmation of the correct crystal structure. When indexing XRD patterns, we use an accurate list of all 2θ or d-spacings determined using peak fit functions in analysis software (e.g. Origin by OriginLab©). Crysfire is used to index integrated XRD patterns by inserting a list of peaks into the program and using indexing packages such as Dicvol91 [50] or Treor90 [51,52]. It is important that only strong / peaks be entered with confidence to ensure a reliable solution. Following indexing, a list of possible solutions are given, with the solutions that are most stable or seem most reliable investigated further. Refinement of the lattice parameters will then reveal whether the solution is a good fit or not, with calculated reflections compared directly with observed peaks and a level of merit is given for that particular solution. A Le Bail fit to the X-ray data fits only peak positions and profiles along with the background. This provides a good way to determine the best fit to the data and for revealing the unit cell parameters. Following Le Bail refinements we can then attempt a full Rietveld refinement [53,54].

Rietveld refinement uses a least-squares method to minimize the differences between the calculated pattern (from our chosen crystal structure) and the observed pattern from our data. Atomic coordinates, background, lattice parameters and peak profiles are all taken into account for full refinement, though there are many other options that are included as a result of instrumentation / optics effects and from the sample itself (e.g. preferred orientation). It is a good idea to use the refined lattice parameters (and peak shapes) from the Le Bail refinement for an initial configuration. The Rietveld analysis is designed to give a 'best fit' to the data using our chosen crystal structure.

Chapter 3. **High Pressure Polymorphism of Crystalline Sn**

3.1. Introduction

The group 14 elements are situated in the periodic table on the boundary between non-metallic and metallic behaviour (Figure 3.1). The lighter group 14 elements are mostly covalently bonded semiconductors, with metallic structures formed for higher Z elements and upon application of high pressure [55-57]. Due to this position in the periodic table, these elements are capable of forming sp^3 bonded diamond-type crystals, as is the case for C, Si and Ge [58]. Mixing of one *s* orbital with three *p* orbitals creates the sp^3 hybridized bonds where one atom is surrounded by 4 atoms with bond angles of ~ 109.5°. With increasing atomic number the energy gained from sp^3 hybridization becomes significantly smaller as the outer electrons move further away from the nucleus. In the case of Sn, which straddles a boundary between semiconducting and metallic behaviour, the electrons are sufficiently far away from the nucleus such that the energy gained from hybridization is small, with the sp^3 diamond-type structure, *α-Sn* (grey tin), only existing at low temperatures ($T < 284$ K at ambient pressure) [59].

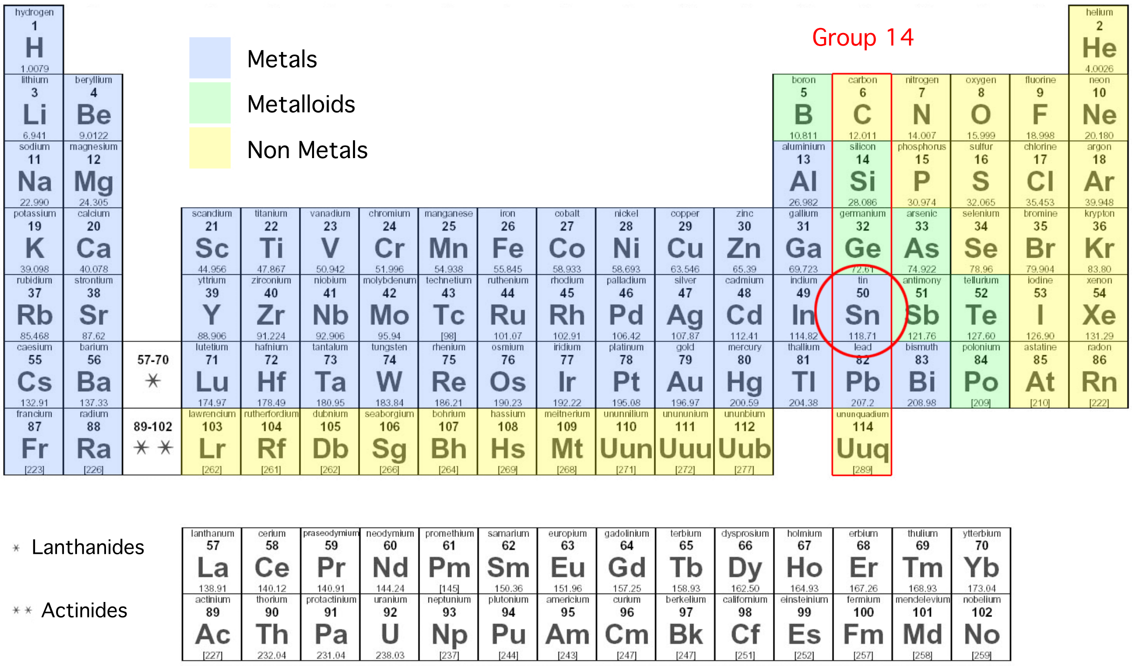

Figure 3.1 Periodic table of the elements. Group 14 and the element Sn are highlighted, revealing the change in metallic nature as atomic number Z increases. Sn sits on the boundary between metallic and semi-conducting behaviour.

The ambient pressure stable form of C is the hexagonal graphite structure, with the denser diamond structure (*cd*) formed at high pressure and high temperature due to its large activation energy. There also exist more exotic forms of C such as the C_{60} 'buckyball' structure [60] and carbon nanotubes [61]. Moving down the group, Si and Ge exist in the diamond structure under ambient conditions. Both Si and Ge are indirect band-gap semiconductors undergoing a series of high-pressure phase transitions from *cd* → *ß-Sn* → *Imma* → *sh* → *Cmca* → *hcp*. On the other hand, Pb is stabilized in the *fcc* phase under ambient conditions due to the relativistic effects of the 6*s* energy state dropping well below the 6*p* state preventing sp^3 hybridization [62].

At ambient P,T conditions, the metallic *ß-Sn* (white tin) is the stable phase with a body centred tetragonal (*bct*) structure. There is a remarkable difference in properties of the two ambient pressure phases. Most strikingly is the volume change associated with the transition from white tin to grey tin (~ 25%) and the change from a malleable nature to very brittle. There are several famous examples of this transition to grey tin, which is referred to as tin pest. When temperatures become sufficiently low, tin pest can cause the disintegration of tin organ pipes in churches as the grey tin becomes brittle and breaks down.

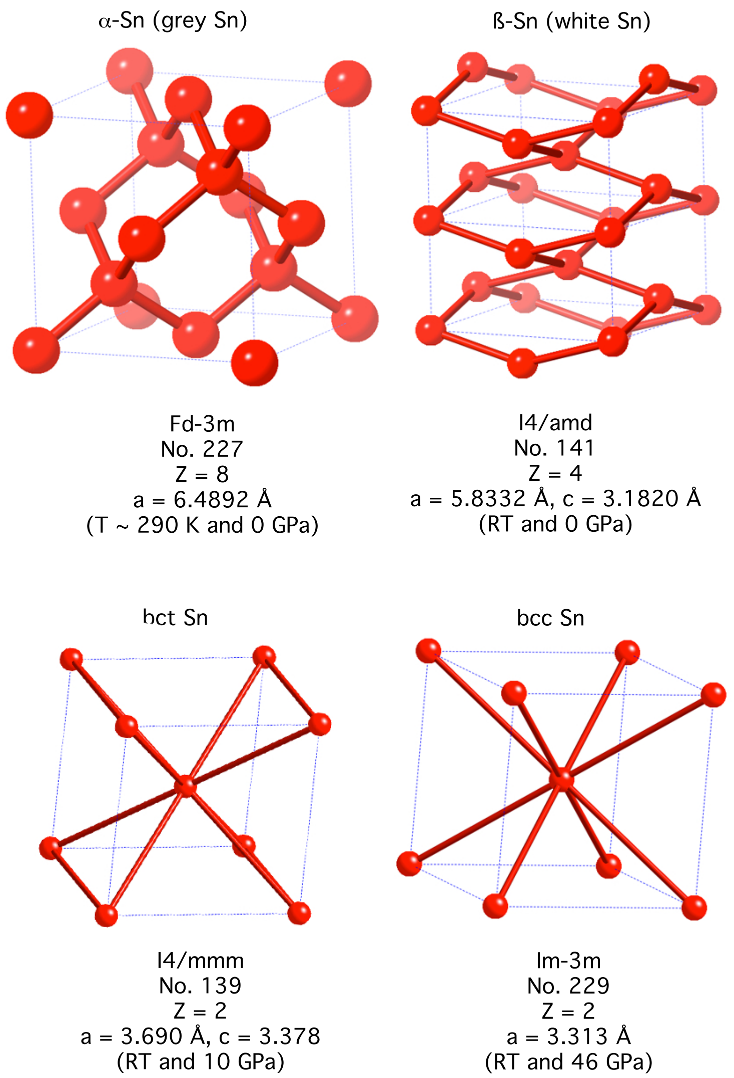

α-Sn (grey Sn)

Fd-3m
No. 227
Z = 8
a = 6.4892 Å
(T ~ 290 K and 0 GPa)

ß-Sn (white Sn)

I4/amd
No. 141
Z = 4
a = 5.8332 Å, c = 3.1820 Å
(RT and 0 GPa)

bct Sn

I4/mmm
No. 139
Z = 2
a = 3.690 Å, c = 3.378
(RT and 10 GPa)

bcc Sn

Im-3m
No. 229
Z = 2
a = 3.313 Å
(RT and 46 GPa)

Figure 3.2 Known crystal structures and unit cell parameters for Sn for different P,T conditions.

The first high pressure experiments on Sn indicated a body centred cubic (*bcc*) form occurring near 10 GPa [63]. Experiments by Bernett *et al.* later noted that the structure was not cubic, but actually had a body centred tetragonal (*bct*) structure with *c/a* ~ 0.91 [64]. As the pressure is increased, the axial ratio increases towards unity (*c/a* = 1), but never attains an axial ratio of greater than ~ 0.95 [65]. The first experimental observation of the *bcc* phase was found by Olijnyk & Holzapfel and Liu & Liu, who observed X-ray diffraction peaks indexed to a cubic phase occurring above 36 and 44 GPa [55,66]. Interestingly, these authors noted apparent co-existence between the *bct* and *bcc* structures over a wide pressure range extending between 40-56 GPa. The *bct* structure was observed at 56 GPa (the highest pressure attained) but had a significantly lower intensity as the pressure increased. Desgreniers *et al.* carried out energy-dispersive X-ray diffraction (EDXRD) experiments between 52-120 GPa and found that only the *bcc* structure was present [67]. These authors argued that the long exposure times (up to 90 hours) and non-hydrostatic stresses in the sample chamber (due to methanol:ethanol PTM) could be responsible for the observation of coexistence. Density-functional theory (DFT) calculations by Yao and Klug recently determined a transition to hexagonal close packed (*hcp*) structure occuring at P = 154 GPa [68]. The *hcp* structure of Sn was found experimentally to occur at P ~ 157 GPa by Salamat *et al.* [69]. This was supported by *ab initio* random structure search (AIRSS) [70] calculations carried out in the same paper matching well with the result from Yao and Klug. Simulated X-ray diffraction patterns for all known Sn crystal structures (below 140 GPa) are shown in Figure 3.3.

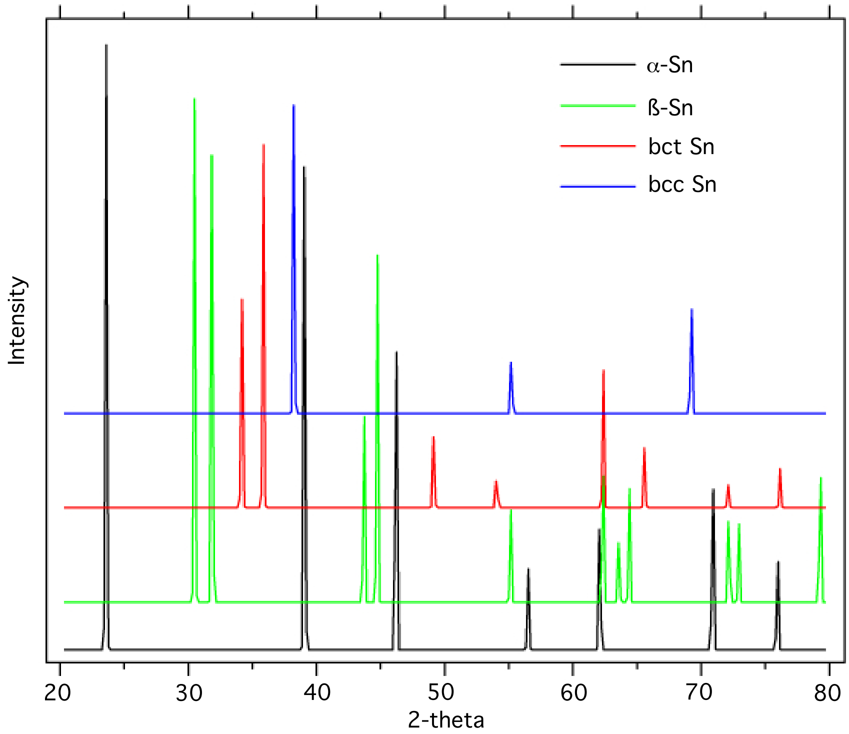

Figure 3.3 Simulated X-ray diffraction patterns for the known crystal structures of Sn (λ = 1.5418 Å).

Sn has been investigated over a large pressure range; however, the curious observation of coexistence of *bct* and *bcc* structures in some papers and not in others has never been investigated further or explained. With the improvements in synchrotron X-ray diffraction studies and near hydrostatic conditions in the diamond anvil cell using He PTM, the equation of state of Sn to beyond 1 Mbar will be investigated and the coexistence region will be carefully studied.

3.2. Experimental Methods

Experiments were conducted using membrane driven diamond anvil cells with culet sizes of 300, 200, 150 and 100 µm to attain pressures of up to 65, 81, 105 and 137 GPa respectively. Samples of Sn (99.9 %, Merck) were loaded into the DACs with He or Ne as pressure transmitting medium. He and Ne were loaded using the Sanchez Technologies high-pressure gas loading system. Re was used as gasket material and was pre-indented to between 30 and 15 μm depending on the diamond anvil sizes and the pressures we wished to hit. Holes were drilled into the sample chamber using laser drilling and were at 50-70 % the size of the culet at starting pressures. A small grain of W was added to the sample chamber as a pressure standard as well as ruby or $SrB_4O_7:Sm^{2+}$ (for lower pressure experiments). The volume of W was determined *via* refinement of the X-ray diffraction patterns and the pressure was then determined using the Vinet EOS for W [37] with K_0 = 296 GPa and $K_0^{'}$ = 4.3.

Synchrotron X-ray diffraction measurements were carried out at ID27, ESRF. A monochromatic beam (λ = 0.3738 Å) was focused down to a 1.7 x 2.3 μm^2 area, allowing fine measurements to be collected without contamination of the XRD patterns by the Re gasket. Raw diffraction patterns were collected using a MAR CCD 165 or a MAR345 image plate and integrated using Fit2D [46]. Indexing of diffraction peaks was carried out using CRYSFIRE[5], with Le Bail refinements of diffraction patterns using GSAS [48] and EXPGUI [49] to determine unit cell parameters. Volume pressure relations were obtained using a third order Birch-Murnaghan equation of state [36] and refined further using a linearly reduced variable (F-*f*) plot.

3.3. Results

The volume *vs* pressure relations of Sn have been determined to P ~ 1.4 Mbar using angle dispersive X-ray diffraction (ADXRD) and with near hydrostatic conditions using He loadings in the diamond anvil cell (Figure 3.4). From close to ambient conditions (P = 0.2 GPa) we observe a series of phase transformations up to 137 GPa from *ß-Sn* > *bct* > *bco* > *bcc*. The *bco* (body centred orthorhombic) structure is a previously unreported structure that has only been able to be observed due to the high-quality and high-

---

[5] R. Shirley , The CRYSFIRE System for Automatic Powder Indexing

resolution data we have collected along with near hydrostatic conditions. Observed are crystallographic signatures of the *bco* structure along with the *bcc* structure in the pressure range of 40-70 GPa, similar to the coexistence regions described in the literature [55,71]. These two key results will be discussed in detail below. For each phase a new Birch-Murnaghan EOS (expanded to the third order) has been determined, with linearized F-*f* analysis providing final values for bulk modulus.

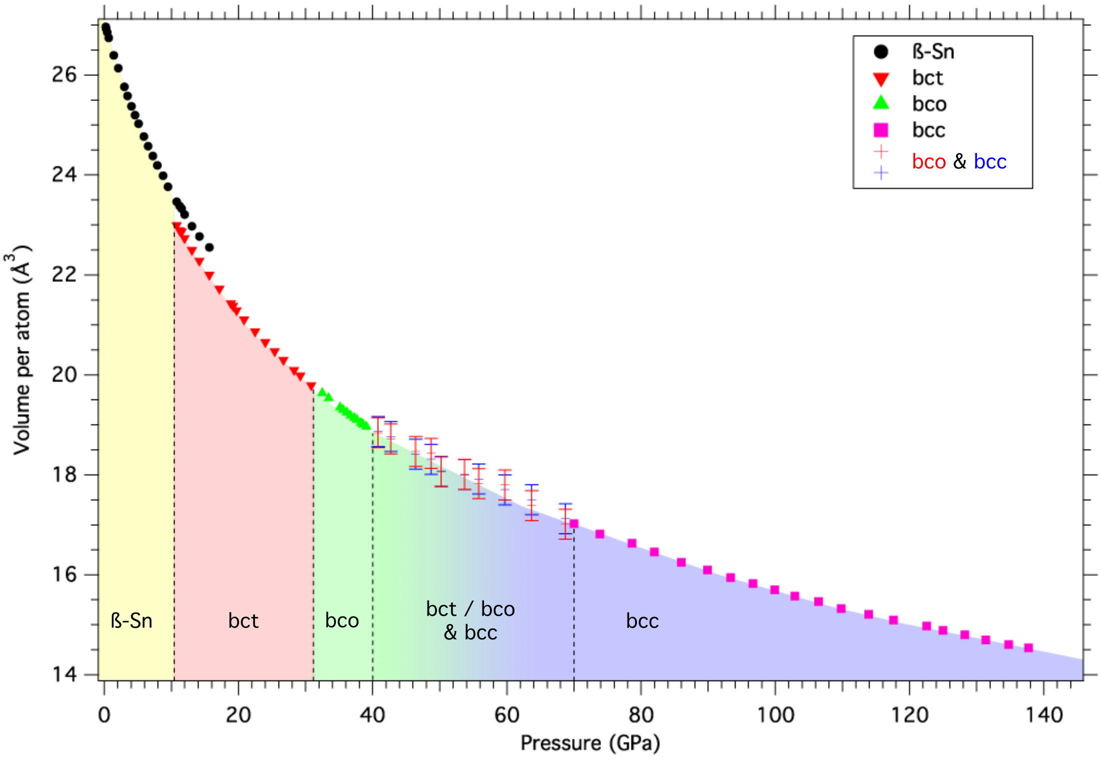

Figure 3.4 The volume-pressure relations of Sn phases between 10-137 GPa at room temperature. The ß-Sn polymorph is stable below 9.7 GPa and coexists metastably with bct structured up to 15.7 GPa under nearly hydrostatic conditions and external pressurisation. Coexistence of bco and bcc structures is visible in the X-ray diffraction patterns between 40 and 70 GPa. The difference in volume determined by individual peak refinements (see Figure 3.10) is used to apply boundaries to the volume relations in this region. Above 70 GPa only the bcc polymorph is observed.

3.3.1. ß-Sn

From P = 0.2 GPa and room temperature, the metallic *ß-Sn* phase (*I41/amd*) exists, which has a *bct* structure with atoms at (*0,0,0*) and (*a/2,0,c/4*). Upon compression the *ß-Sn* phase persists up to a maximum pressure of 15.7 GPa, higher than any previous observations from experiment [55,66]. Above P ~ 10 GPa the *ß-Sn* phase coexists with the new *bc*t phase (*I4/mmm*), which has atoms at (*0,0,0*) and (*1/2,1/2,1/2*). The coexistence between 10 and 15.7 GPa confirms the first order nature of this transition, with a volume reduction of ~ 2.0 %. The V(P) relations were first fit with a third order Birch-Murnaghan EOS [36] between 0.2 and 10 GPa (the pressure range where only *ß-Sn* was observed). Bulk modulus values were determined giving values of K_0 = 61.0(3) GPa, $K_0^{'}$ = 3.4(4) with V_0 = 26.96(2) Å^3. These values were then refined using a linearly reduced variable F-*f* plot, giving values of K_0 = 50.2(5) GPa, $K_0^{'}$ = 4.9(1) using a V_0 = 26.9(3) Å^3. Both the BM and F-*f* fits to the data are shown in Figure 3.5 The F-*f* plot allows us to fit the data using a linear equation that takes into account the weighted error of all the data collected together. There are larger errors associated with the first few data points with small compressions since the change in volume compared to the initial volume is small and so errors are magnified. The data are also shown in Table 1 presenting the increase in *c/a* ratio with increasing pressure and the decrease in volume.

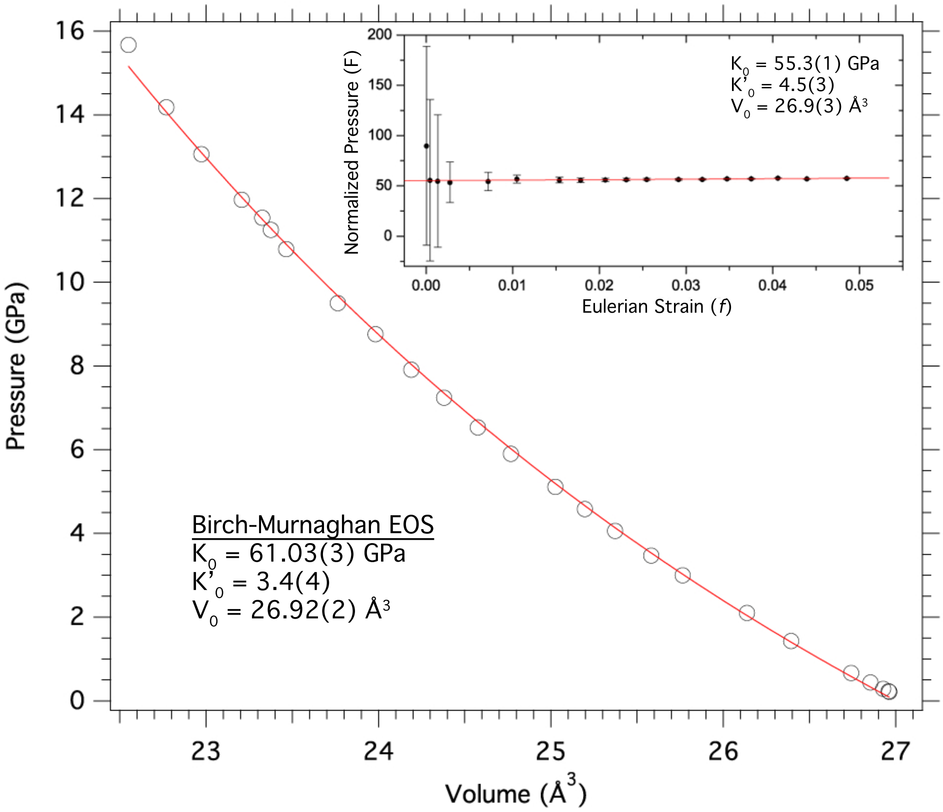

Figure 3.5 Birch-Murnaghan and F-f fits to P(V) data collected for the metallic β-Sn phase. Least square fitting is applied to fit the data (circles) to a third order Birch-Murnaghan equation of state. Inset shows a linear fit to an F-f plot, where the intercept reveals the bulk modulus K_0 and the slope gives its pressure derivative K'_0.

Table 1: Unit cell parameters, c/a ratio and volume per atom for the ß-Sn phase.

Phase	Pressure (GPa)	a (Å)		c		c/a ratio	Volume (per atom)	±
ß-Sn	0.215	5.8259	(5)	3.1776	(4)	0.54542	26.9630	(5)
ß-Sn	0.23	5.8256	(7)	3.1774	(5)	0.54542	26.9585	(8)
ß-Sn	0.29	5.8235	(5)	3.1760	(4)	0.54538	26.9268	(5)
ß-Sn	0.44	5.8184	(7)	3.1729	(5)	0.54531	26.8535	(8)
ß-Sn	0.665	5.8107	(6)	3.1680	(5)	0.54521	26.7413	(8)
ß-Sn	1.43	5.7863	(6)	3.1531	(4)	0.54493	26.3930	(8)
ß-Sn	2.1	5.7682	(8)	3.1421	(6)	0.54473	26.137	(1)
ß-Sn	3.0	5.7416	(6)	3.1262	(4)	0.54447	25.7643	(7)
ß-Sn	3.47	5.7285	(8)	3.1183	(6)	0.54435	25.582	(1)
ß-Sn	4.06	5.7132	(4)	3.1093	(4)	0.54422	25.3725	(2)
ß-Sn	4.58	5.7003	(9)	3.1017	(6)	0.54413	25.197	(1)
ß-Sn	5.11	5.6879	(9)	3.0943	(6)	0.54401	25.026	(1)
ß-Sn	5.9	5.669	(1)	3.0830	(7)	0.54386	24.768	(1)
ß-Sn	6.53	5.6543	(9)	3.0747	(9)	0.54378	24.5760	(7)
ß-Sn	7.24	5.6397	(5)	3.0662	(5)	0.54368	24.3805	(5)
ß-Sn	7.91	5.6253	(6)	3.0578	(5)	0.54358	24.1905	(7)
ß-Sn	8.76	5.6096	(5)	3.0487	(4)	0.54348	23.9833	(5)
ß-Sn	9.5	5.5927	(8)	3.0390	(6)	0.54339	23.764	(1)
ß-Sn	10.79	5.5696	(6)	3.0257	(6)	0.54326	23.4648	(5)
ß-Sn	11.25	5.5628	(9)	3.0218	(8)	0.54321	23.3765	(8)
ß-Sn	11.54	5.559	(1)	3.020	(8)	0.54319	23.326	(1)
ß-Sn	11.97	5.549	(1)	3.014	(1)	0.54323	23.207	(1)
ß-Sn	13.06	5.531	(3)	3.004	(3)	0.5431	22.973	(3)
ß-Sn	14.18	5.515	(7)	2.994	(6)	0.54293	22.770	(6)
ß-Sn	15.67	5.48	(2)	3.000	(2)	0.54723	22.55	(1)

3.3.2. bct and bco Sn

The *bct* phase of Sn (*I4/mmm*) exists from 10 GPa onwards. Le Bail refinements show good fits to the tetragonal phase up to P ~ 30 GPa. Above this point the Le Bail refinements reveal deviations from the ideal tetragonal structure, with peak positions lying slightly to the left or right of the *I4/mmm* fit. This deviation is very small at first and is not easily observable when looking at the whole Le Bail fit (Figure 3.6). However, upon closer inspection of the higher reflections the deviation becomes more clear (Figure 3.7). By adjusting the *a*,*b* and *c* lattice parameters from the *I4/mmm* phase the deviation could be accounted for. At this stage I looked at whether this was due to non-hydrostatic effects in the diamond cell but the ruby peaks revealed no signs of change from hydrostatic conditions. Through indexing of all peak positions using the CRYSFIRE software package, we obtained an orthorhombic solution as a strong candidate (body-centred). From the reflection conditions (Table 4) I was able to identify possible space groups from the international tables for crystallography [72]. Only one spacegroup was identified that matched all of the reflection conditions revealing the *Immm* (71) spacegroup. The *Immm* spacegroup is one of the maximal non-isotropic subgroups of the *I4/mmm* spacegroup, which provides evidence that we are observing a lowering of symmetry in the system. The X-ray diffraction data show an improved fit with the body-centred orthorhombic (*bco*) structure (shown in Figure 3.7).

The *bct* phase is fit with a BM EOS and further refined using F-*f* analysis between 15.7 and 32 GPa. The *bco* phase is fit between 32 and 40 GPa. The *bct* fit reveals elastic parameters of K_0 = 61.1(6) GPa, $K_0^{'}$ = 4.0 with V_0 = 26.31(4) Å^3 and K_P = 118(3) GPa, $K_P^{'}$ = 3.7(2) for the F-*f* fit. The higher value for K_P in the F-*f* fit is a result of the *bct* fit occurring at high pressure, where a reference pressure and volume (P_0 and V_P) are defined, instead of ambient pressures/volumes, with values of 15.7 GPa and 22.51(1) Å^3

respectively. For the *bco* phase we determined K_0 = 63(2) GPa, K_0' = 4.0 with V_0 = 26.2(1) Å^3 and K_P = 176(4) GPa, K_P' = 3.5(5) for the F-*f* fit using P_0 = 32 GPa and V_P = 19.637(8) Å^3.

Table 2: Unit cell parameters, c/a ratio and volume per atom for the bct phase.

Phase	Pressure (GPa)	*a* (Å)	*c* (Å)	*c/a* ratio	Volume (Å^3)
bct	10.79	3.6939	3.37043	0.91244	22.994
bct	11.25	3.6879	3.36601	0.91273	22.8895
bct	11.54	3.6860	3.36595	0.91316	22.867
bct	11.97	3.67777	3.36158	0.91403	22.7345
bct	13.06	3.66283	3.35375	0.91562	22.4975
bct	14.18	3.64907	3.34685	0.91718	22.2830
bct	15.67	3.6310	3.33736	0.91912	22.0005
bct	17.16	3.61328	3.32783	0.921	21.7240
bct	18.88	3.59413	3.31799	0.92317	21.4305
bct	19.2	3.59099	3.31602	0.92343	21.3805
bct	19.72	3.5853	3.31257	0.92394	21.2900
bct	20.83	3.5734	3.30589	0.92514	21.107
bct	22.49	3.5579	3.29697	0.92666	20.868
bct	24	3.54382	3.28917	0.92814	20.6540
bct	25.41	3.53189	3.28233	0.92934	20.4725
bct	26.71	3.52056	3.27563	0.93043	20.2995
bct	28.29	3.5071	3.26781	0.93177	20.0970
bct	29.22	3.4998	3.26323	0.93241	19.9850
bct	30.85	3.4869	3.25577	0.93372	19.7925
bct	31.545	3.4816	3.2518	0.93399	19.709

Table 3 Unit cell parameters, c/a ratio and volume per atom for the bco phase.

Phase	Pressure (GPa)	*a* (Å)	*b* (Å)	*c* (Å)	*b/a* ratio	*c/a* ratio	Volume (Å^3)
bco	32.48	3.469709	3.48234	3.250449	1.0036	0.9368	19.6370
bco	33.44	3.462651	3.47571	3.24625	1.0037	0.9375	19.5350
bco	35.03	3.449728	3.46308	3.239274	1.0038	0.9390	19.3491
bco	35.295	3.448451	3.45829	3.237004	1.0028	0.9387	19.3020
bco	35.945	3.443799	3.45611	3.234665	1.0035	0.9393	19.2500
bco	36.575	3.436396	3.45344	3.233488	1.0049	0.9410	19.187
bco	37.1	3.434026	3.45067	3.230117	1.0048	0.9406	19.1379
bco	37.63	3.430356	3.44750	3.230595	1.0049	0.9418	19.1030
bco	38.23	3.426127	3.44299	3.228219	1.0049	0.9422	19.0401
bco	38.7	3.424642	3.43959	3.227908	1.0043	0.9426	19.0110
bco	39.33	3.420558	3.43584	3.227031	1.0044	0.9434	18.9629
bco	39.7	3.425033	3.40673	3.218368	0.9941	0.9396	18.776

Table 4 Reflection conditions for orthorhombic solution found through indexing of d-spacing peak positions

Bragg peak	h	k	l	Reflection conditions
011	0	k	l	$k + l = 2n$
110	h	k	0	$h + k = 2n$
101	h	0	l	$h + l = 2n$
020	0	k	0	$k = 2n$
002	0	0	l	$l = 2n$
200	h	0	0	$h = 2n$
112	h	k	l	$h + k = 2n$
121	h	k	l	$h + l = 2n$
211	h	k	l	$k + l = 2n$

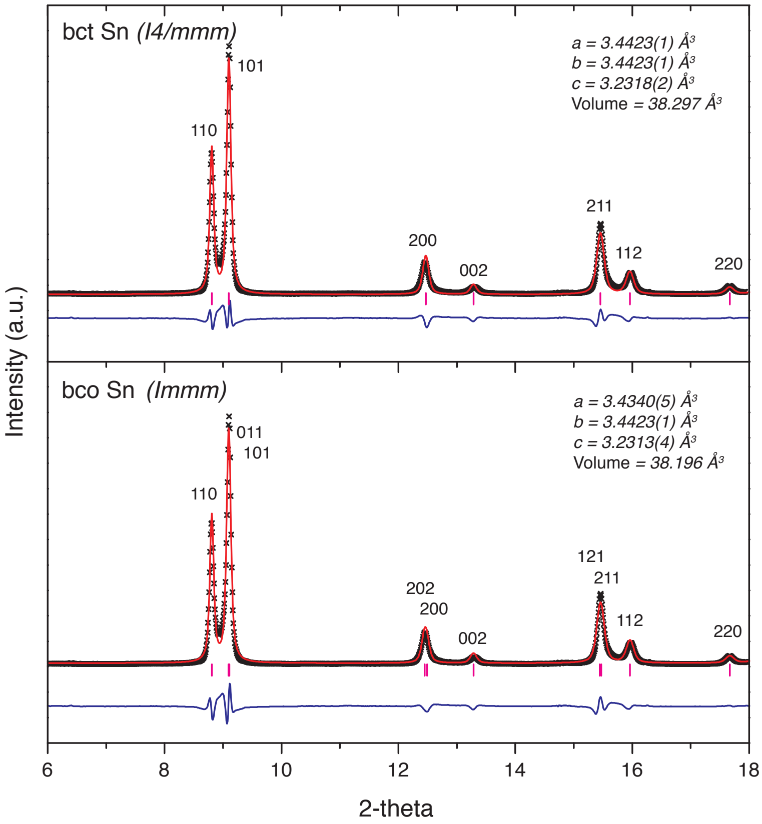

Figure 3.6 Refinement of bct and bco structures across the whole 2θ range. Individual Bragg reflections are labeled in both. Across the whole diffraction pattern there appears to be little difference between the two refinements. ($\lambda = 0.3738Å$).

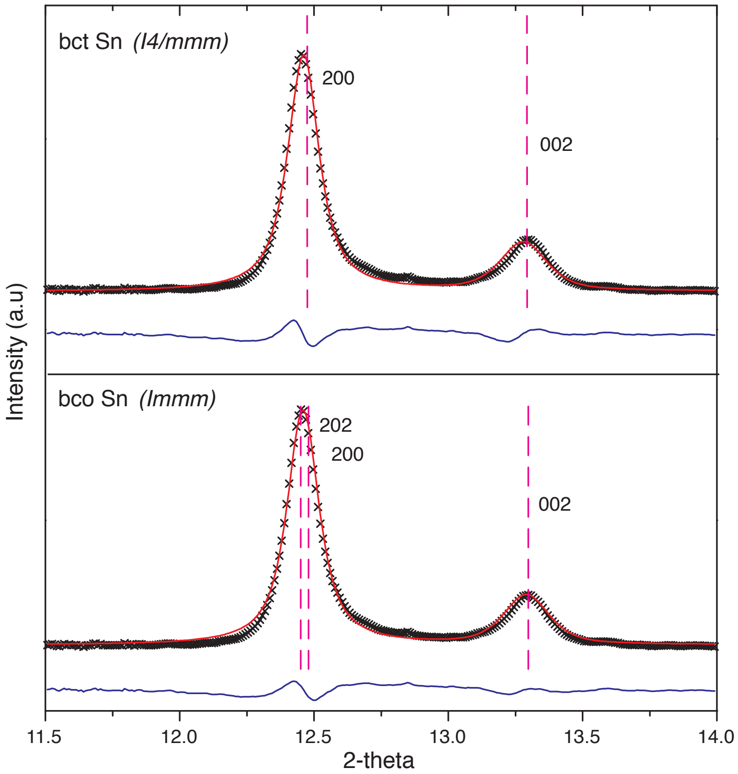

Figure 3.7 Close up of the bct 200 and 002 reflections from Figure 3.6. Fitting the bco (Immm) shows improved fit due to splitting of 200 peak to 202 and 200. (λ = 0.3738Å

The transformation to an orthorhombic structure is further supported by the analysis of the *d*-spacing values as a function of pressure (Figure 3.8). The *d*-spacing values are determined by using single peak fitting procedures. The triangles in Figure 3.8 represent the doublet reflections of an ideal tetragonal structure and the circles represent the 101 *bcc* reflection. There are two changes in slope of the *d*-P values occurring at 30 and 40 GPa. The first is identified from the black dot - dash guideline and the red dash line identifies the second. For clarity there is no guideline drawn for the points between 30 and 40 GPa. These two discontinuities are associated with the transformation to the *bco* structure and the onset of the *bcc* structure. The change in *d*-spacing against pressure is identical for the *bco* and *bcc* reflections from 40 GPa onwards. The *c/a* ratio is calculated in this region using the refined unit cell parameters (Figure 3.9).

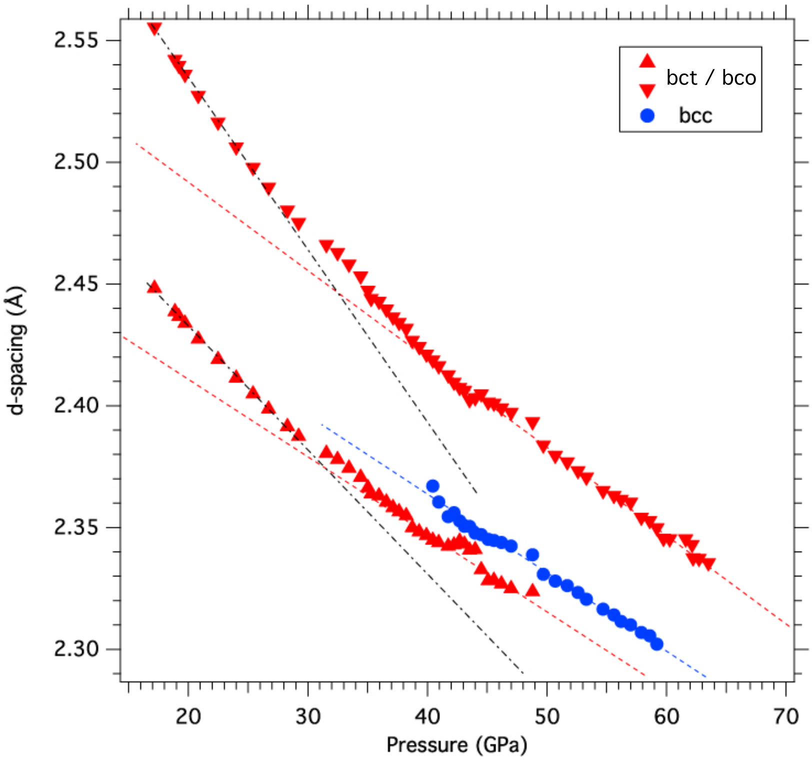

Figure 3.8 d-spacing versus pressure of bct 110 (red upward triangle), bct 101 (red downward triangle) and bcc 110 (blue circle) from the integrated X-ray diffraction patterns diffraction patterns. Changes in gradient are observed at 30 GPa and at the onset of the bcc phase at 40 GPa.

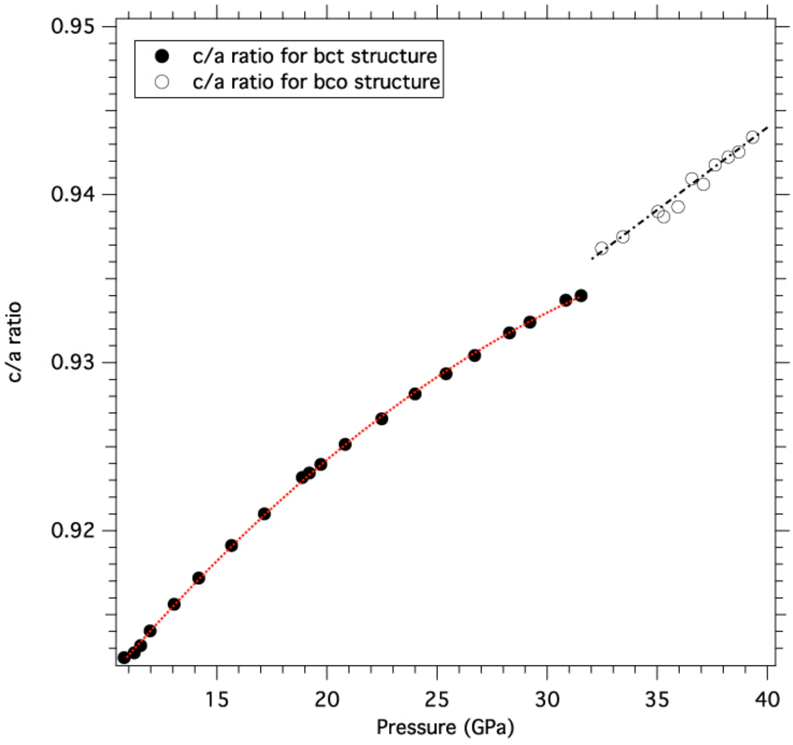

Figure 3.9 Axial (c/a) ratio as a function of pressure for bct and bco structures. The dip / jump can be explained as the bct structure no longer accurately fits to the X-ray diffraction patterns.

3.3.3. Coexistence of bco and bcc structures

Between 40 and 70 GPa there is evidence of new diffraction peaks that become more intense with increasing pressure. These peaks can be fit with the *bcc* (*Im-3m*) structure. From 40 GPa the reflections associated with *bcc* structure develop and the relative intensity of *bco* compared to the *bcc* peaks begin to decrease towards 70 GPa. The intensity of the *bco* peaks become very low and only *bcc* reflections are observed beyond 70 GPa. In this pressure range I could not determine reliable volumes for the respective *bco* and *bcc* structures using the refinement package. Overlapping Bragg peaks in the X-ray diffraction patterns resulted in the refinement package not being able to converge on a single accepted value for unit cell parameters. Instead, I tried to determine d_{hkl} values from individual peak analysis. However, the individual peak fitting revealed different values from each reflection when compared across the whole XRD pattern. The lattice parameter, *a* is shown in Figure 3.10 as a function of pressure. There is a clear difference between the value for *a* determined for the difference peak reflections for *bcc* structure, with a difference of 0.3 Å between the 200 and 110 reflection's value for *a* at P = 40 GPa. Above 70 GPa the difference in lattice parameter becomes smaller until they fall within the experimental error from refinements. Above the point at which the *bco* phase is no longer visible, the *bcc* peak reflections behave as expected and fit perfectly to the bcc structure. The bcc phase is fit from 70 GPa to 137 GPa giving K_0 = 92(4) GPa, $K_0^{'}$ = 4.0 with V_0 = 24.5(3) Å^3 and $K_P^{'}$ = 316(5) GPa, $K_P^{'}$= 3.9(2) for the F-*f* fit using P_0 = 70 GPa and V_P = 17.0231(2) Å^3. A summary of the equation of states determined for *ß-Sn*, *bct*, *bco* and *bcc* Sn phases are shown in Table 6.

Table 5 Lattice parameter and volume versus pressure data for the bcc phase of Sn

Phase	Pressure (GPa)	Lattice Parameter *a* (Å)	Volume (Å^3)
bcc	70.00	3.24108	17.0231
bcc	73.85	3.22778	16.81447
bcc	78.64	3.21579	16.62781
bcc	81.98	3.20465	16.45547
bcc	85.98	3.19118	16.24887
bcc	89.88	3.18106	16.09485
bcc	93.31	3.17125	15.9463
bcc	96.68	3.16294	15.82128
bcc	99.88	3.15477	15.69901
bcc	102.94	3.14646	15.57525
bcc	106.44	3.13905	15.46555
bcc	109.79	3.12971	15.3279
bcc	113.91	3.12157	15.20861
bcc	117.63	3.11379	15.0952
bcc	122.54	3.10558	14.97614
bcc	125.01	3.09950	14.88834
bcc	128.21	3.09354	14.80262
bcc	131.37	3.08621	14.69759
bcc	134.77	3.07965	14.60408
bcc	137.72	3.07489	14.53646

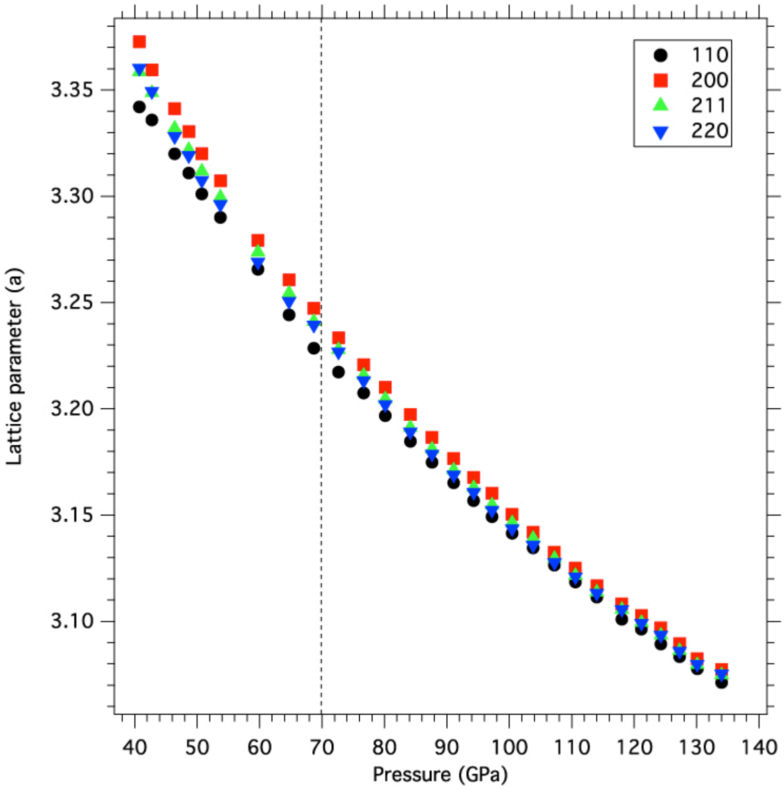

Figure 3.10 Lattice parameter of the bcc phase above 40 GPa determined by individual d_{hkl} values from the 110, 200, 211 and 221 peaks. The dashed line is a guide to the eye representing the boundary applied to observing only bcc structures in the XRD data.

Table 6 Bulk modulus values for all phases of Sn up to 137 GPa. Pressure dependent bulk modulus data are represented by (*).

Phase	**K_0 / K_P (*) (GPa)**	**K'_0 or K'_P (*)**	**V_0 or V_P (*) (Å^3)**	**P_0 (GPa)**
ß-Sn	50.2(5)	4.9(1)	26.9(3)	0
bct	118(3) *	3.7(2) *	22.51(1) *	15.7
bco	176(4) *	3.5(5) *	19.637(8) *	32
bcc	316(5) *	3.9(2) *	17.0231(2) *	70

3.4. Discussion

Recent improvements in high-pressure research have allowed us to generate quasi-hydrostatic conditions in the diamond anvil cell using He PTM, enabling higher-resolution data to be collected and observing previously undetected distortions in crystal structure. Thanks to the high-pressure gas loading system at UCL, we can now load He at high P (~ 1400 bar) into DAC without a catastrophic collapse in sample chamber as pressure was increased. With this technique pressures up to 137 GPa have been obtained (~ 1.4 Mbar). This has been the key tool in allowing us to identify the very small distortion from *bct* Sn to *bco* Sn above 32 GPa at RT. At these pressures, all previous experimental studies had already reached the hydrostatic limit of the PTM and the resolution of the XRD data was not on the same scale and so the data was assumed to represent *bct* Sn under non-hydrostatic stress.

In these experiments, non-hydrostatic stress in the sample chamber was thought to be a mechanism for the distortions from ideal tetragonal symmetry. However, repeat experiments using different pressure media (He or Ne) revealed the same behaviour occurring consistently at the same P. In some experiments, ruby fluorescence was used as a pressure standard and the R1 and R2 fluorescence lines of ruby gave us information on the hydrostatic conditions inside the sample chamber. Usually, when the two peaks begin to merge or begin to change in peak profile, this is a sign that the PTM has lost its hydrostaticity and there is shear stress in the sample chamber. The FWHM and peak shapes of the ruby peaks were monitored as a function of pressure and found no deviations in the 30-40 P range where the onset of the orthorhombic distortion starts. Also, full-width at half maximum (FWHM) analysis were performed on the XRD peaks, revealing a change in slope of the FWHM for 200 and 211 Sn reflections (Figure 3.11) but not the 112 reflection. The 200 and 211 peaks are the reflections that are most affected by a distortion to *Immm* symmetry. Further evidence for ruling out non-hydrostatic stresses as a mechanism for this distortion comes from the behaviour of the *bcc* phase above 70 GPa. If non-hydrostatic stresses were causing distortions of the *bct* phase, we would expect this distortion to remain present at even higher pressures for the *bcc* phase also. Instead the *bcc* structure can be indexed perfectly, with no signs of distortions due to non-hydrostatic conditions.

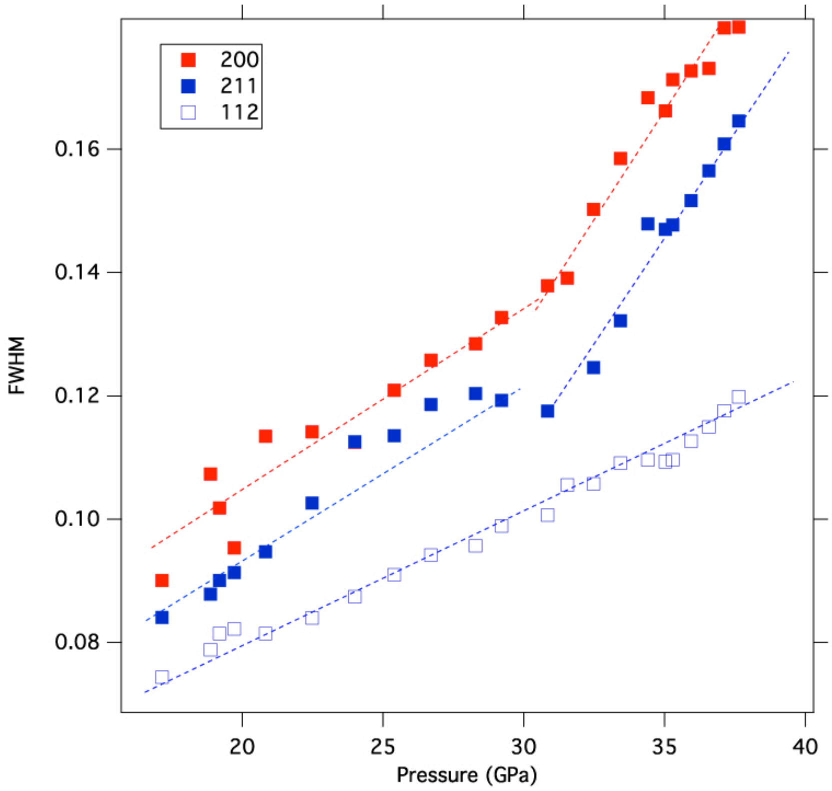

Figure 3.11 Full width at half maximum analysis of bct / bco reflections.

The pressure volume relations for Sn across the whole pressure range appears to look like a normal equation of state with no deviation from a BM fit, however we know this is not the case as there are small volume changes associated with the transformations from *bct* to *bco* structure and later to *bcc* structures. The various regions of P-V space that represent *bct*, *bco*, and *bcc* Sn have different values of bulk modulus determined after separate F-*f* analysis. However, by applying the F-*f* analysis over the whole pressure range we are able to distinguish these regions with a greater clarity (Figure

3.12). There is a large jump in F-*f* values at *f* ~ 0.05 corresponding to the ß-Sn to *bct* Sn transition. The next three dashed lines represent the transformation pressures to *bco, bco* + *bcc* and *bcc Sn* respectively. A small but noticeable jump in F-*f* is observed first, followed by a significant change in slope in the 40-70 GPa second and finally a final change in slope at the *bcc* only boundary. The deviations in F-*f* slopes in this figure do not provide us with any physical information; instead only show us with much greater clarity the minor changes in P-V relations that are occurring spanning a pressure range into the megabar range.

The X-ray diffraction data obtained between 40-70 GPa clearly shows the presence of reflections assigned to *bco* and *bcc* structures. The relative weight of the two sets of diffraction features changes continuously throughout the pressure range, which could be interpreted as indicating the occurrence of a phase transformation between two closely related structures with coexistence over a wide pressure range. However, upon assigning the new crystallographic signatures as the cubic *bcc* phase, with which I could extrapolate various determinations of the unit cell parameter *a* using the XRD data, there was an observed difference in the volumes that were extracted from the various crystallographic signatures. This does not describe an ideal cubic system that we would expect to see in the near hydrostatic conditions in the sample chamber. Above 70 GPa the behaviour becomes more ideal and all reflections converge and I can index the whole system as the cubic *bcc* phase with no deviation.

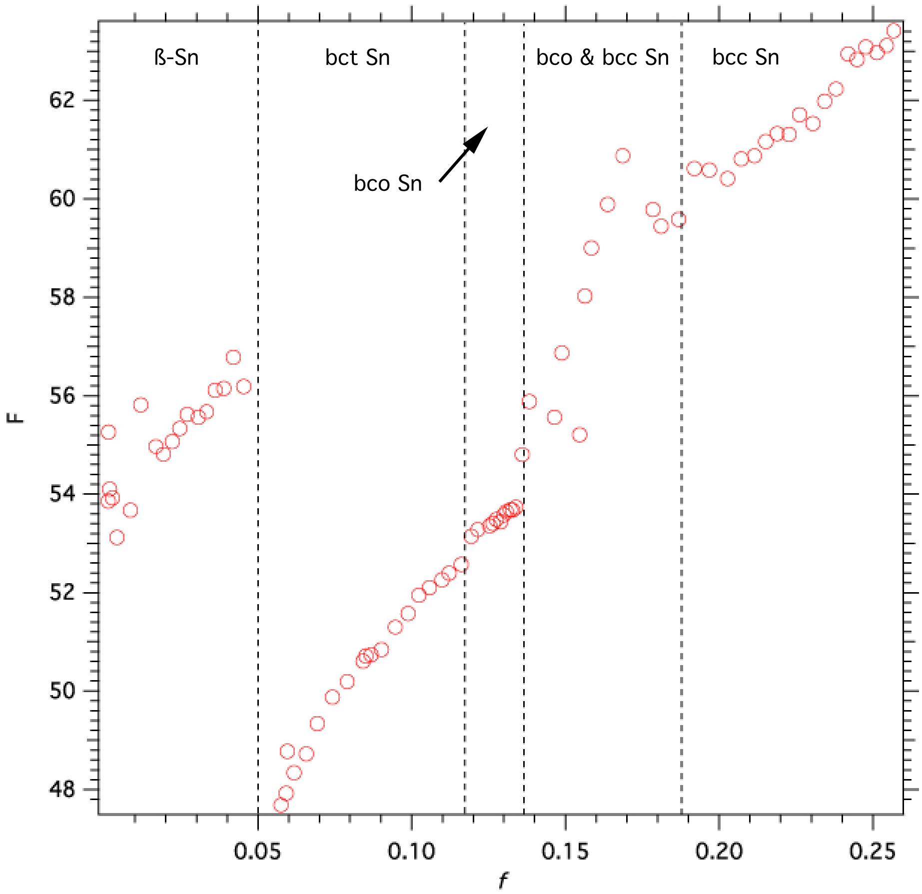

Figure 3.12 F-f plot of PV relations over the whole pressure range from ~0.2 GPa to 137 GPa. The transformations are easier to observe in this plot than the PV plot which shows no significant changes in PV relation. Here the jumps in F-f represent the transformations to bct, bco, bco + bcc and bcc Sn.

Figure 3.13 shows a stack plot of the integrated X-ray diffraction patterns focused around the 101 *bcc* reflection from 36-69 GPa. It is obvious that both *bco* and *bcc* structures are present, as highlighted in blue and red circles presenting the *bco* and *bcc* peak assignments. The inset of Figure 3.13 shows the raw diffraction peaks. The *bcc* reflection is recorded at the same azimuthal position as the parent *bco* reflection. There is no change in the relative intensities of the *bco* and *bcc* peak reflections recorded at different places in the sample, but the azimuthal width of the *bcc* single crystal spots is larger than the *bco* single crystal spots. The implications of these features suggest that the *bcc* structure develops from the parent *bco* structure, growing within regions of strain or crystallographic defects within the Sn crystal. This accounts for the deviation in volumes determined by individual peak analysis, as there is implied stress in the system not from the PTM, which remains near hydrostatic, but in fact from the sample itself. Within the 'coexist' region of 40-70 GPa I could not analyze the diffraction patterns to obtain stable solutions in terms of the *bco* and *bcc* fitted structures. For that reason I could not determine reliable unit cell parameters and volumes throughout this range, represented by the error bars in Figure 3.4. I attempted to force fit a BM fit across the entire data set from 15.7 GPa to 147 GPa. However that result could not reproduce the V(P) behaviour of either the upper limits or the lower pressure data. I then tried to extrapolate V(P) solutions from the *bco* data upwards and the reverse for *bcc* data. Again, I could not reliably match all data points.

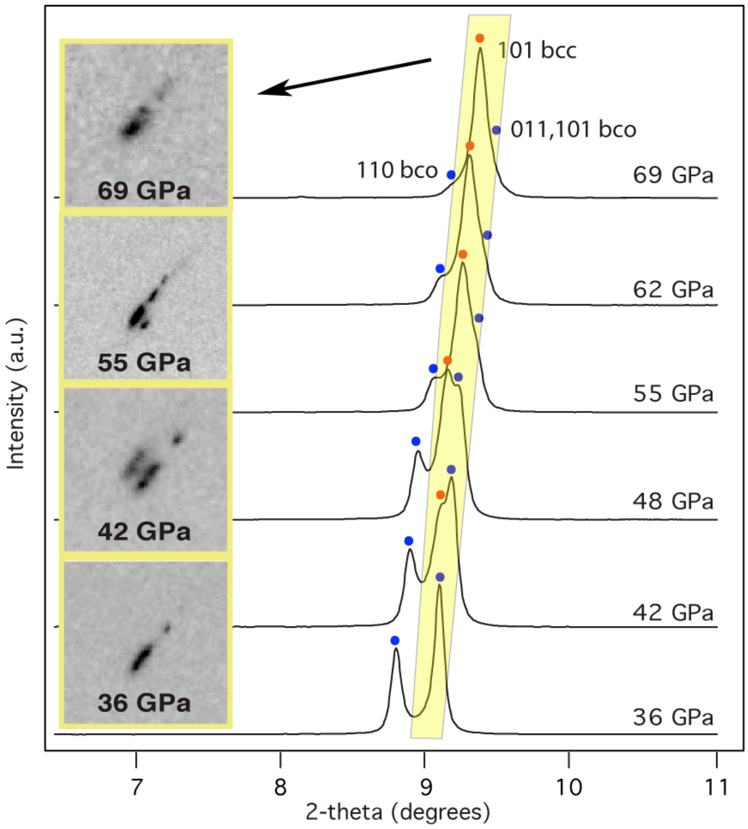

Figure 3.13 Stack plot showing the apparent coexistence of two phases. Inset shows the crystal spots from the raw diffraction patterns. As we can see from 42 GPa to 55 GPa, the bcc structures are orientated from the same crystallographic axes as the bco structure (that then becomes diminished). (λ = 0.3738 Å)

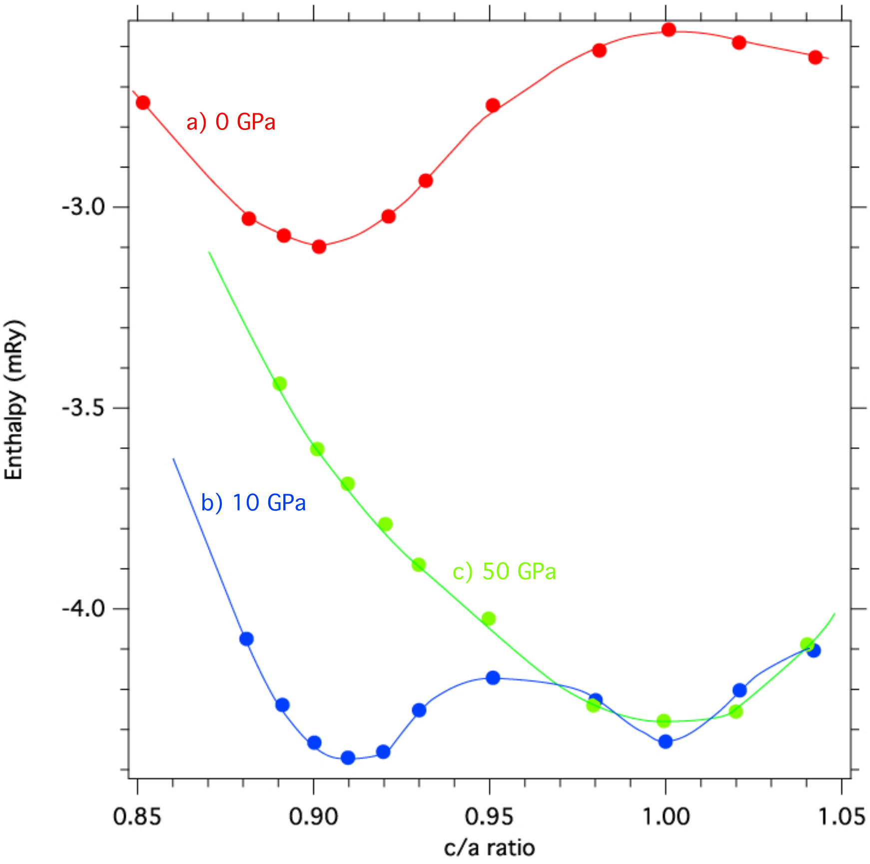

Figure 3.14 Enthalpy versus axial ratio at a) 0 GPa, b) 10 GPa and c) 50 GPa retrospective pressures (estimated from the volumes used in the calculations). Above 10 GPa, there is a minimum in enthalpy representing the stable bct structure as well as a second minimum that develops further with increasing pressure. As pressure increases the minimum associated with the bct structure becomes very flat until only the c/a = 1 minimum becomes stable. From [55].

The peculiarity that Sn does not transform into the highly coordinated *bcc* structure from the ß-Sn structure was examined theoretically by Christensen and Methfessel [73]. These authors used full potential muffin tin orbital techniques to calculate the total energy as a function of volume and coaxial *c*/*a* ratio up to P ~ 50 GPa. Tetragonal splitting occurs from the splitting of the *p*-state H_{15} level which lowers the energy for lower volumes corresponding to regions where *bct* Sn is observed experimentally. With decreasing volume (increasing pressure) a minima corresponding to *c*/*a* = 1 begins to develop until it becomes the dominant minima at higher pressures (Figure 3.14). Between the lower and higher pressures the energy landscape is very broad, with the energy difference between *bct* and *bcc* structures < 3 meV. This barrier is extremely small and is smaller even that the thermal energy *k*T and the zero point energy (ZPE) of the system. At room temperature, these barriers would be smaller than the ZPE contribution and so the two minima can be sampled simultaneously, providing separate XRD signatures. This occurs over a wide pressure range between 40-70 GPa. Above and below these pressures the stable minima is deepened sufficiently such that only *bct*/*bco* or *bcc* Sn structures are observed.

Chapter 4. **High Pressure Phase Diagram of Sn**

4.1. Melting Curve of Sn to P > 1 Mbar

4.1.1. Introduction

At ambient pressure Sn melts from the *ß-Sn* phase at ~ 232˚C, with the melting curve first studied at pressures up to 10.5 GPa by Dudley and Hall in 1960 [74]. The melting point was determined by a sharp rise in electrical resistance of the sample that was compressed in a tetrahedral-anvil press. A triple point was found at P = 3.8 GPa and T = 591 K. Following on from this investigation Stager, Balchan and Drickamer measured a discontinuity in resistance at a reported pressure of ~ 11.4 ± 1 GPa at T = 25˚C, speculating that the transformation was to a cubic phase [75]. The first X-ray diffraction data that attempted to support a cubic phase was reported by Jamieson in 1963 showing the cubic phase existing at ~ 10 GPa [9]. However, there were contradictions by Barnett, Bennion and Hall who actually reported a *bct* structure for Sn with an axial *c*/*a* ratio ~ 0.91 at 3.9 GPa at 314˚C [76]. Jamieson later reported the *bct* phase at a pressure of 12.0 GPa at 25˚C [63]. A combination of these data indicated a new phase line on the phase diagram of Sn (Figure 4.1).

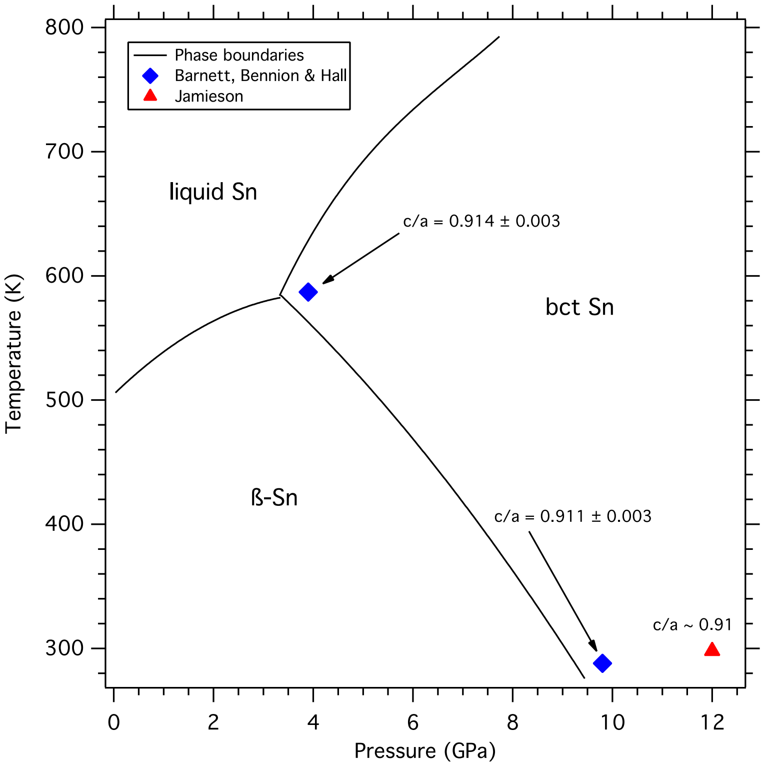

Figure 4.1 Phase diagram of Sn to 10 GPa. Solid lines represent the phase boundaries determined by Kennedy and Newton [77]. Also shown are data points collected by Barnett et al. and Jamieson that were the first indications of a transition from ß-Sn to bct Sn.

Bernard and Maillet calculated the melting curve and Hugoniot of Sn up to 50 GPa using first-principles and classical molecular-dynamics (MD) simulations [78]. The melting curve was calculated by direct phase co-existence, with its Hugoniot curve calculated up to 200 GPa using an equilibrium MD technique. These authors faced difficulties in calculating the Hugoniot since they were unable to simulate the solid-solid phase transition from *ß-Sn* to *bct* Sn. Theoretical studies by Feng *et al.* revealed a much lower melting curve using the a different theoretical model [79]. In this investigation, the phase diagram of Sn was split into two zones representing ß-Sn and γ-Sn, which treats the whole pressure range above 10 GPa as a single phase. The melting curve agrees well up to approximately 20 GPa at which point the melting points become lower than previous results (almost 700 K by 50 GPa). By taking the whole P range above 10 GPa as a single phase they are therefore unable to account for the underlying phase transitions and new phases occurring above 10 GPa that would have drastic effects on the shape of the melting curve.

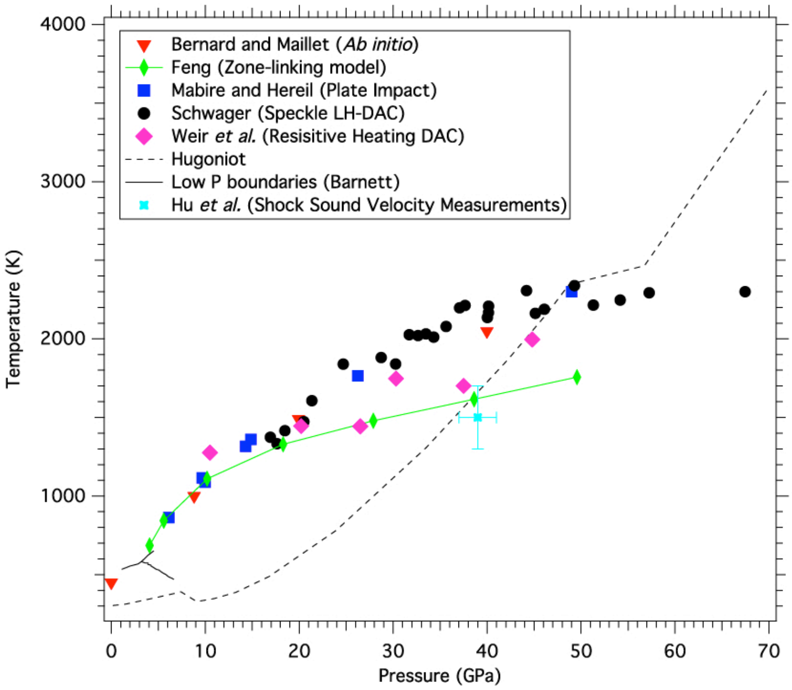

Figure 4.2 Previous results on the melting curve of Sn. The majority of data show a steady increase in slope of the melting curve, with LH-DAC speckle data (circles) showing a flattening of the melting slope at around 40 GPa.

The melt curve has been determined in plate impact (shock) experiments by Mabire and Hereil [80]. Melting was determined upon isentropic release from the shockwave, with discontinuities in the measured sound velocity indicating the onset of melting. Incipient melting (the point at which the Hugoniot crosses the melting curve) was reached at P ~ 49 GPa and T ~ 2300 K. Recently Hu *et al.* performed similar shock impact experiments looking at the sound velocity measurements as a diagnostic technique to indicate the onset of melting or other phase transformation phenomena [81]. However, the pressure and temperature at which they record incipient melting is significantly lower than that of Mabire by almost 1000 K and 10 GPa (P ~ 39 ± 2 GPa with T ~ 1500 K).

The first static experiments to push the pressure boundaries to above 50 GPa were performed in 2011 by Schwager *et al.* using the laser speckle method [82]. The melting curve was studied to P ~ 68 GPa and showed the melting temperature plateau with a near constant value of T ~ 2300 K. The results match very well with the shock melting results by Mabire, and represent the only data collected above 50 GPa. Weir *et al.* carried out resistively heated measurements in the DAC later up to melting temperatures and showed discontinuities associated with the melting temperatures. A combination of all the previous melting data is shown in Figure 4.2.

4.1.2. Experimental Methods

Melting experiments were carried out at beamline ID27 of the European Synchrotron Radiation Facility. The high X-ray flux and fast read out times of the X-ray source, combined with the double-sided laser-heating facilities make this one of the only synchrotrons in the world where we can perform these high P melting experiments. A total of ~ 20 days worth of beamtime were used to complete this experiment. Samples of pure Sn (99.99% Aldrich) were pre-compressed into a foil approximately 5-10 μm thick and loaded into cylindrical or membrane driven DACs under inert conditions. NaCl or KBr were used as a pressure-transmitting medium (PTM) and to thermally insulate the diamond anvils. The PTM was first loaded into the sample chamber and packed tightly by closing the DAC, compressing the PTM inside. A small amount of PTM was then evacuated from the chamber using a micro-needle and the sample was loaded into this hole (and away from the gasket). The PTM was then packed back on top of the sample creating a suitable amount of insulation between the sample and diamond anvil culets.

Diamond anvils with 300, 200, and 150/300 (beveled) μm culets were used for attaining pressures up to ~ 60, 80 and 100+ GPa respectively. Re was used as gasket material and pre-indented to ~ 25-40 μm with holes drilled ranging from 40-100 μm diameter. Pressures were determined initially using ruby fluorescence and from the equation of states for NaCl or KBr. The final values for the pressure were determined from the equation of state of Sn as determined in Chapter 3.

Samples were taken to desired pressures at room temperature before alignment of the IR lasers began (Nd:YAG IR lasers: λ = 1064 nm). The alignment of the IR lasers is a crucial step in melting experiments, as it is important to ensure the sample is heated at the same area as where X-ray diffraction (XRD) patterns are collected. To align the lasers we increase the laser power slowly until we see the first signs of thermal emission from the sample. This usually occurs at temperatures near 1500 K. By viewing the sample from upstream and downstream cameras we can align the heating lasers to the same spot on the sample. The IR lasers are slightly defocussed on each side to reduce thermal gradients throughout the sample.

The X-ray beam was focused to a 2 x 2 μm^2 area at the centre of the hotspot using X-ray fluorescence from the PTM. All lights are turned off and a diode is used to observe fluorescence from the PTM caused by the X-ray beam. The X-ray spot is then moved until it is perfectly aligned with the pinhole and hence aligned with the centre of the laser heating spot. Thermal emission spectra were recorded from the same 2 x 2 μm^2 area and fitted to Planck and Wien functions to determine T. XRD measurements were taken with 1 s exposures every few seconds, collecting hundreds of diffraction patterns in a single melting run. We were able to monitor the raw XRD patterns *in situ* to monitor the state of the sample continuously, increasing the laser power steadily. XRD patterns were then integrated as a function of 2θ using FIT2D [46]. XRD refinements were carried out using POWDERCELL [47] or GSAS/EXPGUI [48,49]. The disappearance of crystalline peaks followed by the appearance of liquid scattering signatures in the XRD patterns was taken to indicate the onset of melting.

Figure 4.3 shows a series of raw XRD images that we use to determine the melting point. A sample at pressure was heated using the two IR lasers that started to show emission at T ~ 1600 K. Once heating well from both sides (and at ~ the same T) the laser power is ramped up, collecting thermal emission readings every few seconds. At the same time, we are collecting XRD patterns with the time stamps of the two files synched. This allows us to determine the temperature for any given XRD pattern. A stack plot of the XRD patterns allows us to look for the first sign of liquid scattering, though in many cases this is easily observed from the raw XRD patterns (Figure 4.3). Pattern 1 shows a powder sample in a crystalline state. With increasing temperature the peaks become visibly weaker in intensity (pattern 2) just before melting, at which point we observe the broad diffraction ring due to liquid scattering (pattern 3).

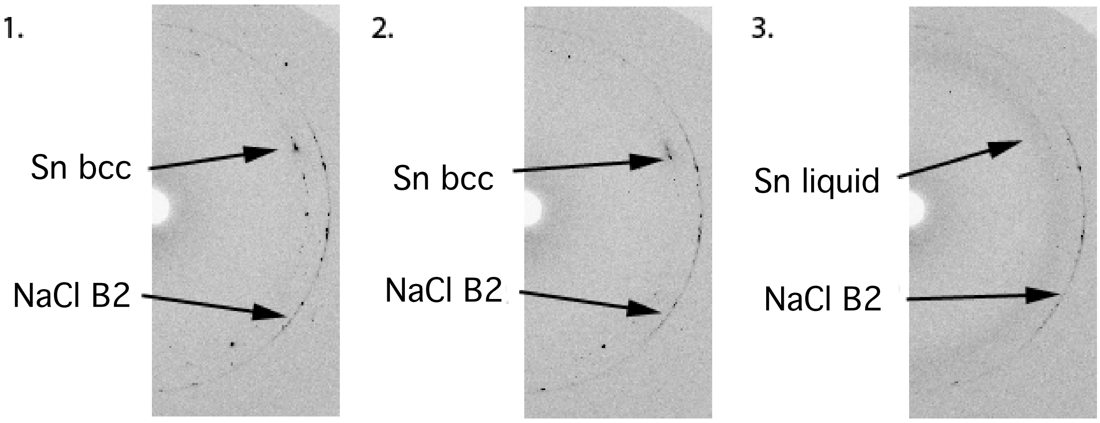

Figure 4.3 Determination of the melting point. The crystalline sample (in this case bcc Sn) is monitored as temperature increases. Frame 1 shows the powder ring in a crystalline state, frame 2 shows the sample just before the melting point where peak intensities decrease and finally frame 3, which shows the first sign of liquid scattering in the diffraction patterns.

4.1.3. Results

Figure 4.4 shows a series of X-ray diffraction patterns focused on the most intense powder diffraction rings of *bcc* Sn, showing the way we determine the melting point. The dashed black line is the Sn sample at high temperature (T ~ 2200 K) and with increasing T the next two patterns are taken from just below the melting point (blue line with T ~ 2600 K) and after melting with the sample in a liquid state (red line with T ~ 2800 K). The first observation of liquid scattering in the XRD patterns is taken as the melting point. The temperatures were determined using Planck and Wein fits to the thermal emission data and collecting every few seconds throughout the experiments. The temperature profile for this particular experiment is shown in Figure 4.5. The points (1), (2) and (3) refer to the three XRD patterns shown in Figure 4.4. The laser power is increased steadily over time as we are collecting XRD patterns and the thermal emission data are fit to Planck or Wein functions to determine T. The inset of Figure 4.5 shows the three XRD patterns in the raw format, with liquid scattering easily observed by a broad halo.

The melting curve of Sn has been measured to P > 1 Mbar using laser-heated diamond anvil cell techniques combined with *in situ* synchrotron X-ray diffraction. The melting point was measured from P ~ 20 GPa up to a maximum pressure of ~ 105 GPa. We observe a rise in the melting slope 20 GPa with a steady dT/dP ~ 40 K GPa^{-1}. This matches well with the static measurements determined by the speckle method. Between 40 and 60 GPa we too observe a flattening of the melt curve before an unexpected rise in melting relation above 70 GPa. The rise in melting relation is extremely sharp with a value of dT/dP ~ 80 K GPa^{-1}, reaching a maximum melting temperature of 5500 ± 500 K at ~ 105 GPa. This result could not have been predicted from the previous experiments or from theoretical calculations.

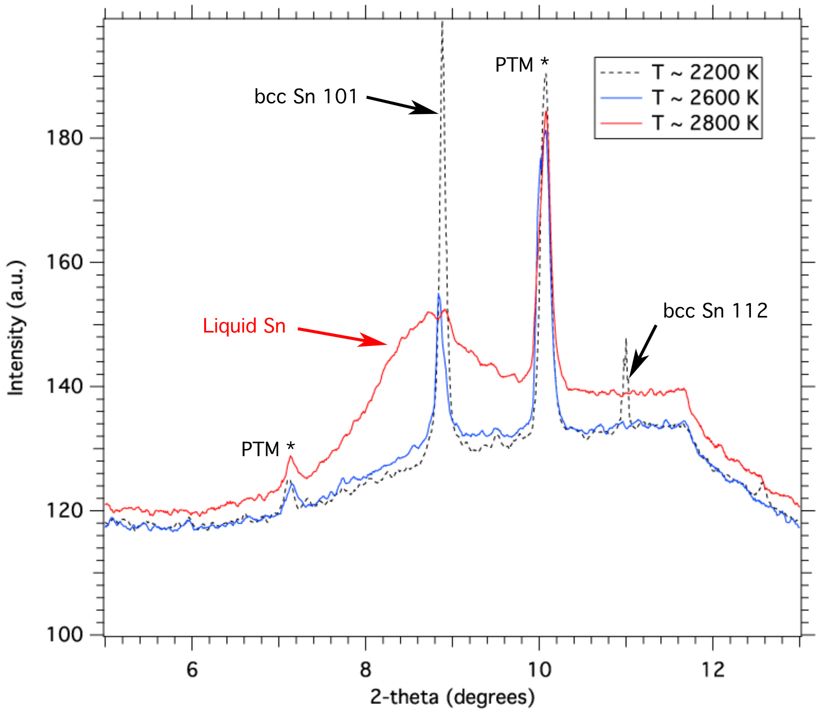

Figure 4.4 Determination of the melting point from integrated X-ray diffraction patterns. The temperatures are taken from figure 4.5. Diffuse scattering of liquid Sn is observed in red. The melting point is taken as the first observation of diffusing scattering in the X-ray diffraction patterns.

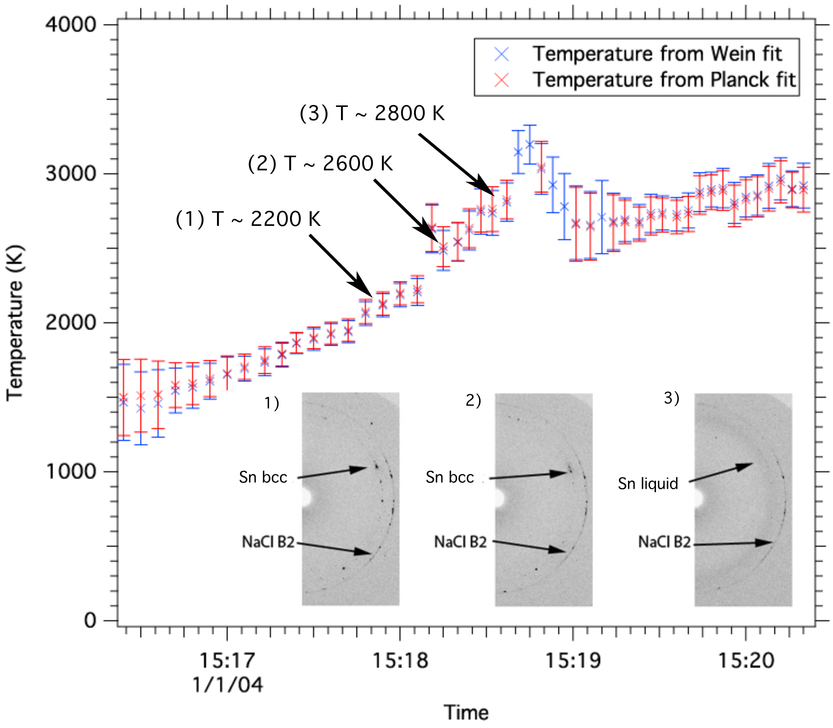

Figure 4.5 Temperature profile for experimental run on bcc Sn. Inset shows the corresponding X-ray diffraction patterns for the three temperatures highlighted.

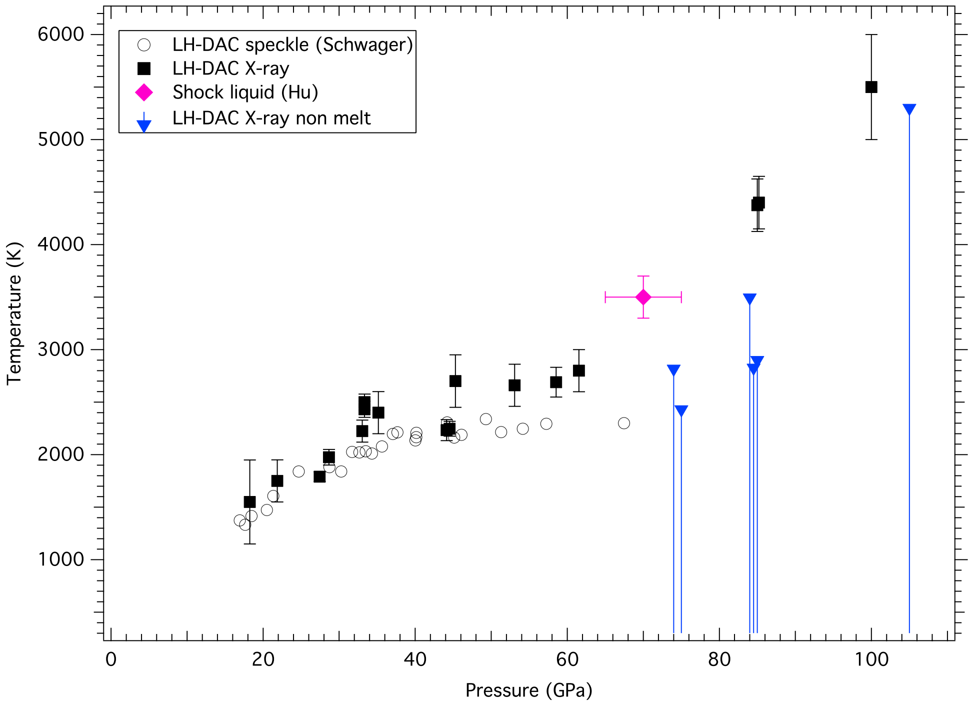

Figure 4.6 Melting curve of Sn determined by LH-DAC techniques combined with X-ray diffraction. Blue triangles and drop lines represent non-melting events where only crystalline Sn is observed, giving further evidence to the high melting slope observed.

4.2. High temperature studies of Sn

4.2.1. Introduction

The intrinsic thermodynamic properties of pressure and temperature are linked together to form a phase diagram that describes the boundaries between different states, whether they are solid-solid or solid-liquid (melting). With the advent and development of the diamond anvil cell and other high pressure techniques, one can probe regions of P,T space and using analytical techniques such as X-ray diffraction these boundaries can be identified. This section combines some of the laser-heating data from the previous section, with resistively heated data revealing key information on the crystalline state of Sn at high temperature. Using this information the first construction of the phase diagram of Sn to beyond 1 Mbar in pressure has been determined.

The detection of *bco* and *bcc* structures present in X-ray diffraction data collected at room temperature match well with the observation of multiple minima in potential energy calculations at T = 0 K [73]. To observe this same behaviour, even at ~ 300 K, has stoked interest in whether this persists at even higher temperatures approaching the melt. The phase diagram above pressures of ~ 10 GPa has mostly been limited to room temperature compression runs, as previously discussed, but also to studies on the melt curve [82,83]. However, information below the melt curve remains mostly unexplored across a very broad P,T range. Shock wave studies are limited to studying P,T regions along the Hugoniot and upon release from shock [81,83], but are not able to tell us key information such as crystal structures.

Shock-induced melting experiments by Hu *et al.* revealed discontinuities in the longitudinal sound velocity that they associated with a *bct* to *bcc* transition and incipient melting of the sample occurring at 34 ± 2 GPa and 39 ± 2 GPa respectively [81]. The incipient melting point of 39 ± 2 GPa and melting temperature ~ 1600 K do not match with recent LH-DAC experiments on the melting curve of Sn [82,84]. Interestingly though, the two points occur at the same pressures that our recent observations of an orthorhombic distortion (32 GPa) and onset of *bcc* signatures alongside *bco* (40 GPa) during room temperature compression. No static high-pressure measurements have been performed in this pressure range at high temperature. By varying the pressure and temperature through resistively and laser heated diamond anvil cell (DAC) techniques, we have set out to map out the P,T region below the melt curve using *in situ* synchrotron X-ray diffraction to determine the crystal structure.

4.2.2. Experimental Methods

Resistive heating experiments were carried out at I15 of Diamond Light Source to probe the crystalline state of Sn below the melt curve in the pressure region where coexistence was seen to occur. The resistive heating DAC had to be seated on a special ceramic sample holder as the DAC heated significantly during prolonged heating experiments (Figure 4.7). This was to ensure there was no thermal expansion of the sample stage causing the alignment to drift during experiments. Diamond anvils with culets of 300 or 200 μm were used. Sn samples (Aldrich 99.99%) were loaded into the RH-DAC with NaCl or LiF as pressure-transmitting medium (PTM). Re gaskets were pre-indented to ~ 35-40 μm before holes of 90 and 150 μm were drilled. Pressure was increased using a pressure driver that filled N_2 into the gas membrane. Pressure was determined from the equation of states of the appropriate PTM, with the EOS of Sn used for final pressure determination. To generate the high temperatures we increased the voltage across the heater between collections and let the T settle across the sample chamber for ~ 5 mins. The temperature was read from a thermocouple connected directly to the lower diamond anvil. Temperature drift during exposures was never more than ~ 2 K.

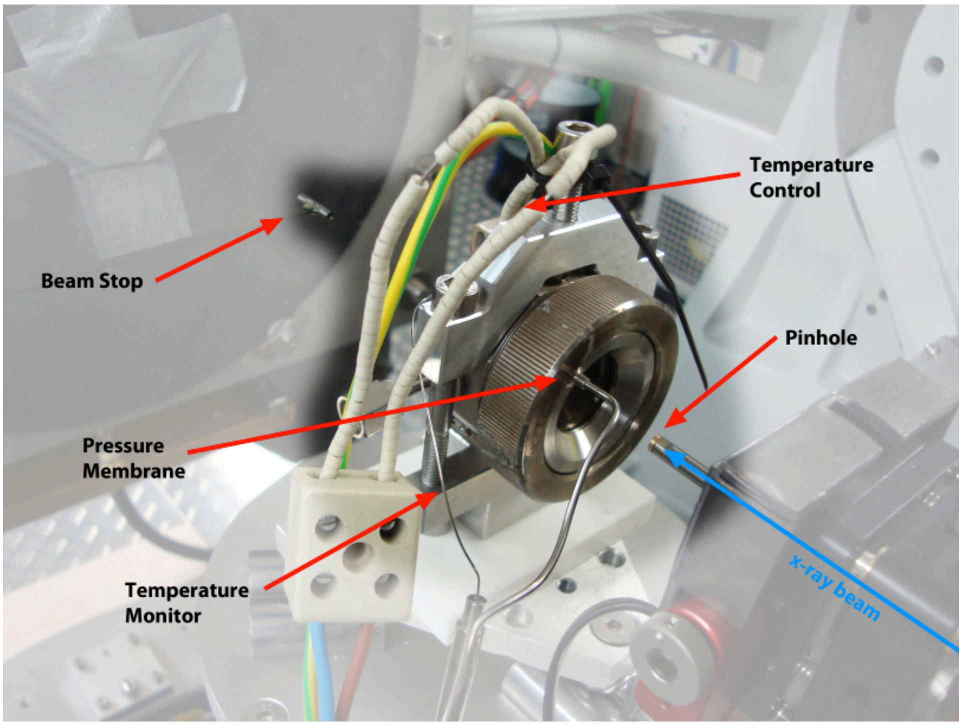

Figure 4.7 Resistive heating DAC online at I15, Diamond Light Source. The temperature was controleld from a voltage control box, with T read directly from a thermocouple touching the diamond. The pressure membrane is attached that drives the piston and increases the pressure in the sample chamber.

For laser-heating experiments, performed at ID27 ESRF, diamond anvils with culet sizes of 300, 200 and 150/300 μm were used to obtain pressures up to 60, 85 and 105 GPa respectively. Re was used as gasket material with indents ranging from 25 – 40 μm. Samples of Sn were loaded with NaCl or KBr as PTM and to thermally insulate the sample. Exposure times were constrained to 1 s as the focus was to look for visible signs of melt from the RAW and integrated X-ray diffraction patterns. Doubled-sided laser-heating was carried out using two IR Nd:YAG lasers. Fitting Planck or Wein functions to thermal emission data determined the temperatures.

4.2.3. Results

X-ray diffraction patterns of Sn have been collected up to P ~ 105 GPa and temperatures up to ~ 5500 K using resistively heated and laser-heated DAC techniques. RH methods allowed us to reach a maximum T ~ 750 K with data of higher resolution in comparison to LH data (covering the T range ~ 1500 – 5500 K). From RH experiments at DLS I observe evidence for coexistence of *bct* and *bcc* structures from the integrated XRD patterns. Upon heating these peaks remain present in the XRD patterns even at prolonged exposures to high T. These results are backed up via LH data collected in the 1500-3000 K temperature range; where some evidence of *bct* peaks is still present in the diffraction patterns towards melt. It should be noted that the *bct* structure at room temperature shows a slight deviation from the ideal tetragonal structure *I4/mmm* and is most likely the *bco* structure *Immm* we discovered in the previous section. However, due to the use of LiF or NaCl as PTM, the conditions in the sample chamber are non-hydrostatic and shear stress in the sample environment could explain the deviations from ideal tetragonal structure instead of an orthorhombic distortion observed in near-hydrostatic conditions.

Figure 4.8 shows an example of one of the RH experimental runs carried out at DLS. The dashed XRD pattern represents room temperature Sn at 44 GPa before heating. The co-existence of *bct*/*bco* with *bcc* is observed inset as a small shoulder on the inside of the *bct* 101 peak (*). With increasing temperature this peak becomes more pronounced and its relative intensity, compared with that of the *bct* peaks, increases. This is also observed *via* full width at half maximum (FWHM) analysis of the peaks where a decrease in FWHM of *bcc* peaks and an increase in FWHM of *bct* peaks shows the bcc structure becoming further dominant at higher temperatures.

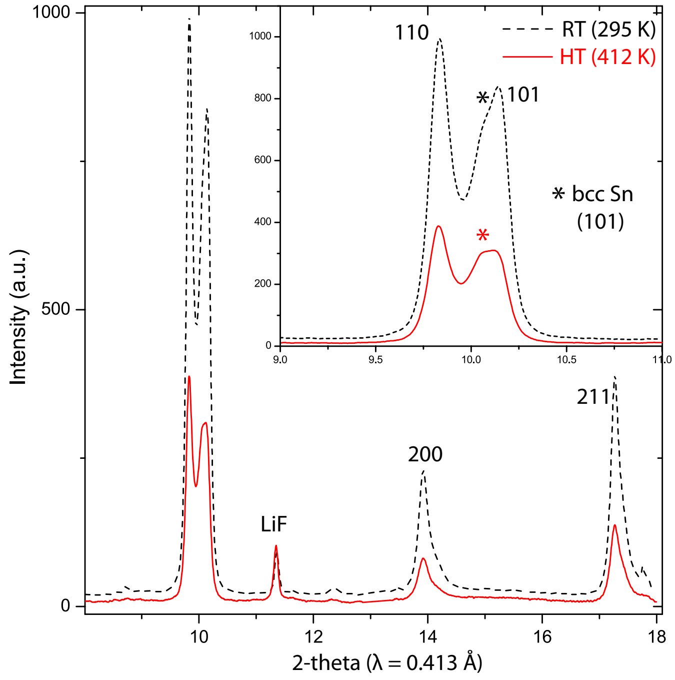

Figure 4.8 Comparison of X-ray diffraction patterns collected at room temperature (dashed line) and high temperature (solid red line). The star in the figure represents the bcc structure that develops as temperature increases. P = 44 GPa.

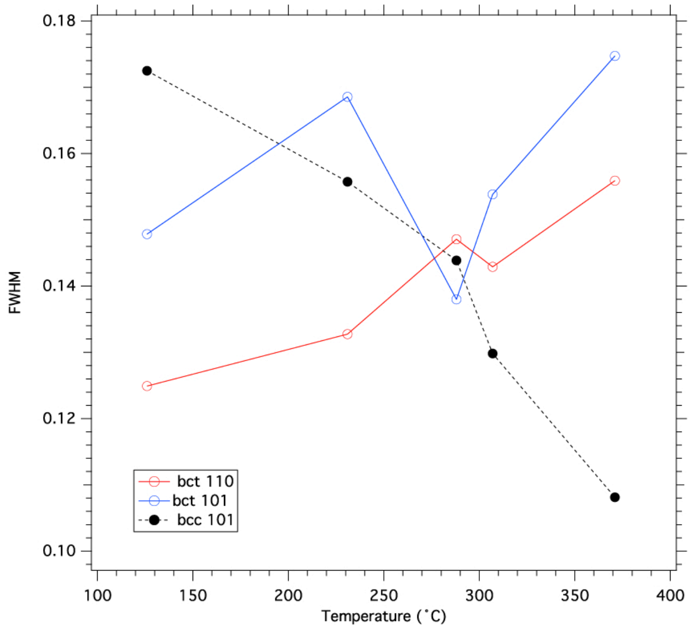

Figure 4.9 FWHM analysis of the 110 and 101 reflections of bct Sn and the 101 reflection of bcc Sn. With increasing temperature the FWHM decreases for the bcc structure, indicating the structure becoming dominant and increasing in relative intensity compared to the bct structure.

4.3. Discussion

All previous data on the melt curve stop near to where the shock Hugoniot crosses the melting curve at P ~ 55 GPa. The static melting results from speckle experiments show a flat melting curve up to the maximum obtainable pressure of ~ 68 GPa. A significant number of melting curves determined by speckle techniques reveal flat melting behaviour [85,86]. However, my results do agree well with the speckle melting up to P ~ 60 GPa. Within experimental errors of both data, the melting point at 70 GPa could also be quite close to these melting temperatures and so cannot be said to be incorrect. One of the main problems with speckle techniques is the lack of *in situ* characterization of the sample. With NaCl and KBr PTM I did not see any reaction with the Sn samples, however, MgO was used as PTM in the speckle experiments and so there is a possibility that the speckle motion observed could have been reaction between Sn and the MgO PTM forming a tin oxide or from melting of the surround PTM. The melting data presented here match the speckle data revealing a flat melting relation between 40 and 60 GPa before a sudden rise in melting slope at 70 GPa revealing high melting temperatures.

There are several problems that can be associated with generating temperatures above ~ 3500 K. When loading the DACs you try to ensure there is a large amount of insulation between the sample and diamonds. However, this can be problematic when gasket sizes approached smaller dimensions (for the higher pressure melting experiments). Some runs showed good loadings with the sample away from the gasket, but laser heating only worked on one side or no sides. This indicated the sample had migrated towards the diamond anvil. Any attempt to increase the laser power and hence temperature resulted in the diamonds taking all the heat away from the sample and we saw a plateau in the temperature between 3000 and 3500 K. In many cases I was still able to collect important information about the crystalline state of the sample. To determine the melting points at around 80 and 100 GPa, there were several runs where I could not generate enough temperature to take the sample above melting. However, I was still able to reliably say that the sample was in a solid state based on the XRD data that was observed (Figure 4.10).

For convenience I will refer to the *bct* only region as region I (which also includes the transformation to *bco*), the pressure range where *bct*/*bco* and *bcc* structures are present as region II and finally region III as the pressure range where only *bcc* is present. By mapping out the P,T space using synchrotron X-ray diffraction in the DAC, one can start to develop a picture of where these different structures exist (Figure 4.10). Region I extends from the transition from *ß*-Sn to *bct* Sn at ~ 10 GPa up to 40 GPa at room temperature. The onset of region II at 40 GPa extends at high temperature all the way up to the melt curve, with some evidence of region II occurring at P ~ 39 GPa and temperatures > 1900 K. Region II extends from 70 GPa up to melting temperatures, at which point only region III is observed at room temperature and high temperature.

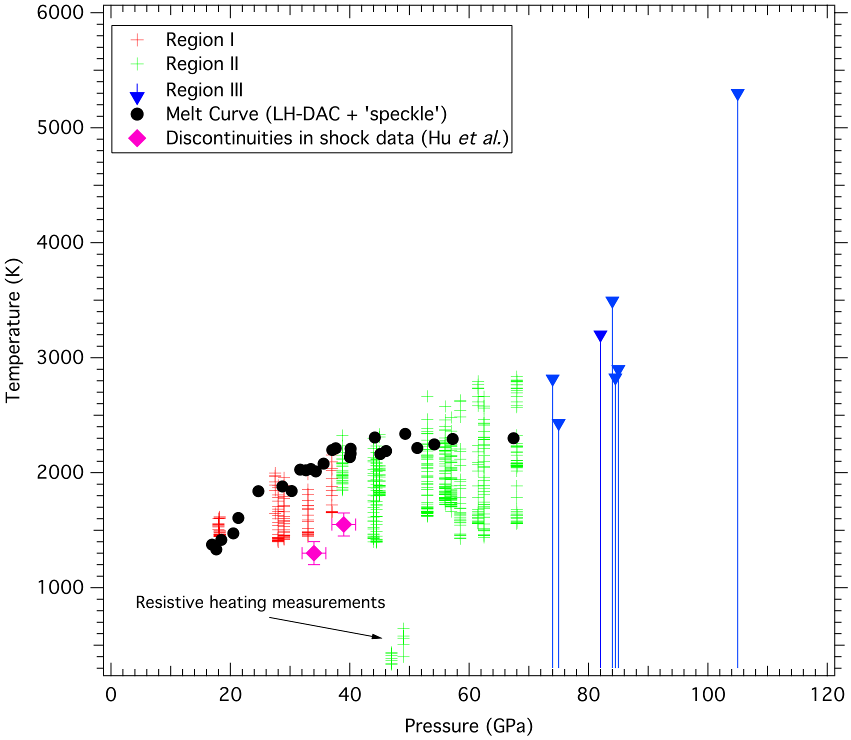

Figure 4.10 P-T plot of crystalline Sn regions to P > 1 Mbar. Region 1 describes bct/bco only, region II describes bct/bco + bcc Sn (coexisting) and region III describing bcc Sn only. The melting curve from LH-DAC + speckle measurements is shown alongside the two shock discontinues discussed. All data shown above in red, green and blue represent X-ray diffraction patterns revealing crystalline Sn only and show no signs of melting.

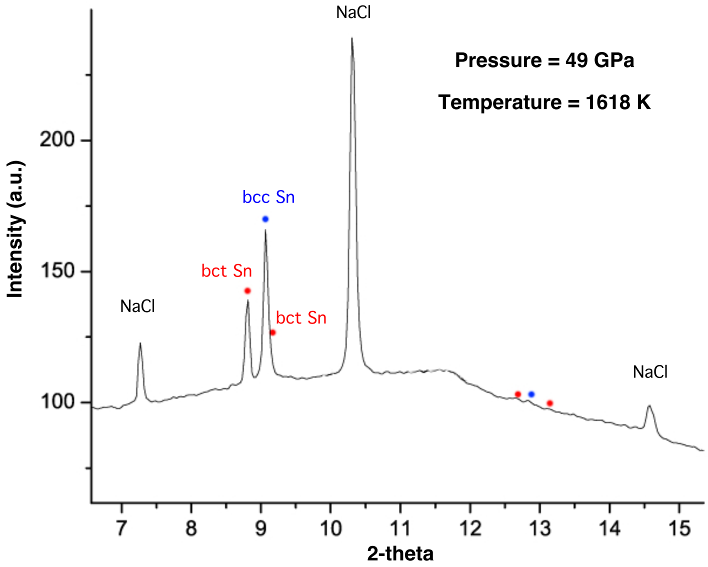

Figure 4.11 X-ray diffraction pattern at P = 49 GPa and T = 1618 K revealing both crystalline bct & bcc Sn. (λ = 0.3738 Å)

A dip in the melting slope followed by a sudden rise in melting relation is usually indicative of an underlying solid-solid phase transition occurring in the system and an associated triple point. This is the case for the *β-Sn* to *bct* transition. The onset of *bcc* structures in coexistence occurs at 40 GPa and room temperature. If a triple point was present in the system associated with the *bct* / *bcc* transition then we would expect an extremely large Clapeyron slope from RT leading up to the rise in melting relation at 70 GPa and T ~ 3400 K. However, from the high temperature data we have collected we know that this is not the case. The *bct/bco* and *bcc* structures remain in coexistence even at high temperature and show no signs of a Clapeyron slope that would result in a triple point on the melt curve near 70 GPa. Even if the *bct*/*bco* to *bcc* transition resulted in a triple point near P ~ 70 GPa, the volume change associated with the transition (< 0.5 %) could not explain the sudden rise in slope to such high melting values. The Clapeyron equation is the relationship between pressure, volume, temperature and entropy given by dT/dP = ΔV/ΔS where ΔV is the difference in volume between the two phases (e.g. $V_{liq} – V_{solid}$). When the melt curve begins to flatten at around 30 GPa, the relation dT/dP begins to decrease towards 0. This would imply that for higher pressures either the volume of the liquid is compressing faster than the volume of the solid or that the relative entropies are changing (with the entropy of the liquid increasing faster than the entropy of the solid). However, there is almost no change in volume associated with the transformation from *bct* to *bco* Sn at P ~ 32 GPa. Equally, we would expect the entropy of *bct* and *bco* Sn crystals to be very similar. A significant decrease in volume would actually increase the melting relation in this region. Only two literature references attempt to construct a *bct* / *bcc* transition line from shock sound speed measurements [81] and from resistive heating measurements on the melting curve [87]. Both suggest a negative melting slope for a Clapeyron equation hitting the melt curve above 30 GPa. This is highlighted in (Figure 4.12), where the two points are plotted along with a 'transition line' drawn from the mid-point of the *bct/bcc* coexistence range. However, this disagrees with the majority of the laser-heating data collected in this study that reveal both structures present in XRD patterns up to the melting point. Figure 4.11 shows an example of an XRD pattern at P = 49 GPa and T = 1618 K, almost 700 K above the implied *bct/bcc* transition line. All temperatures above this XRD pattern revealed *bct* Sn and *bcc* Sn structures up to T_m. Instead, this transition line is more likely to represent the first onset of *bcc* Sn developing in coexistence with the *bct/bco* Sn. Matching this information with the high temperature data shown in Figure 4.10 I could then construct the first high pressure phase diagram for Sn up to 1 Mbar (Figure 4.13).

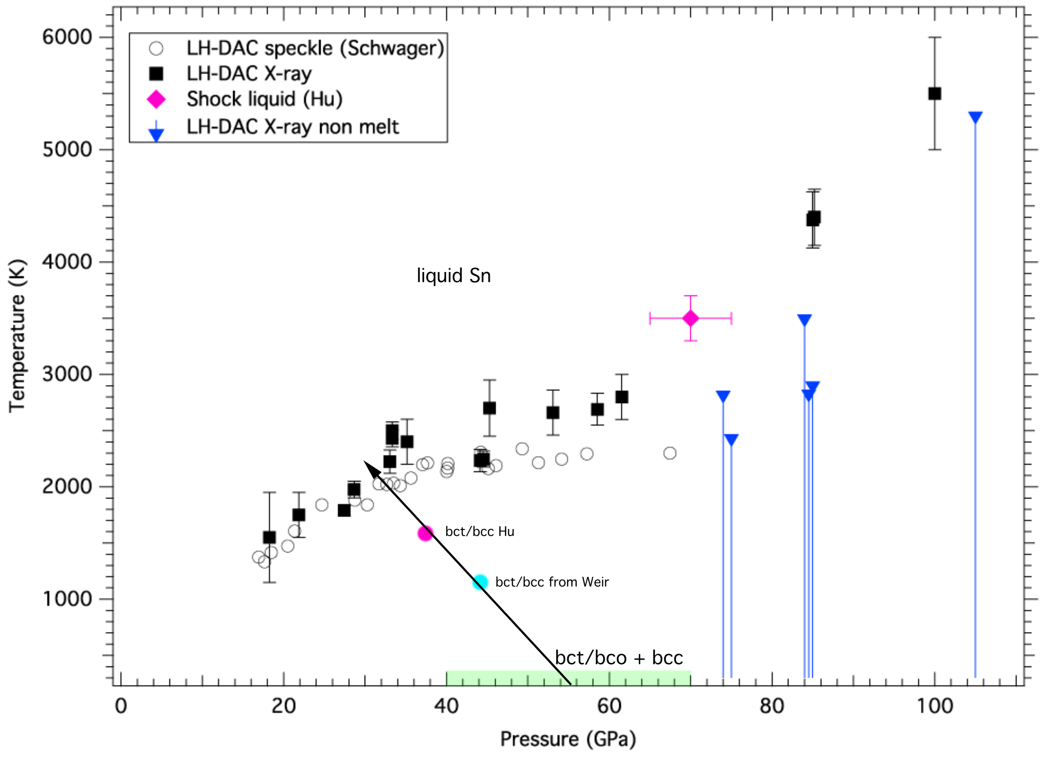

Figure 4.12 Melt curve of Sn showing the suggested bct/bcc transition line from sound velocity measurements (pink circle) and from resistive heating measurements (blue circle). Green shading is the bct/bco & bcc coexistence range from Chapter 3.

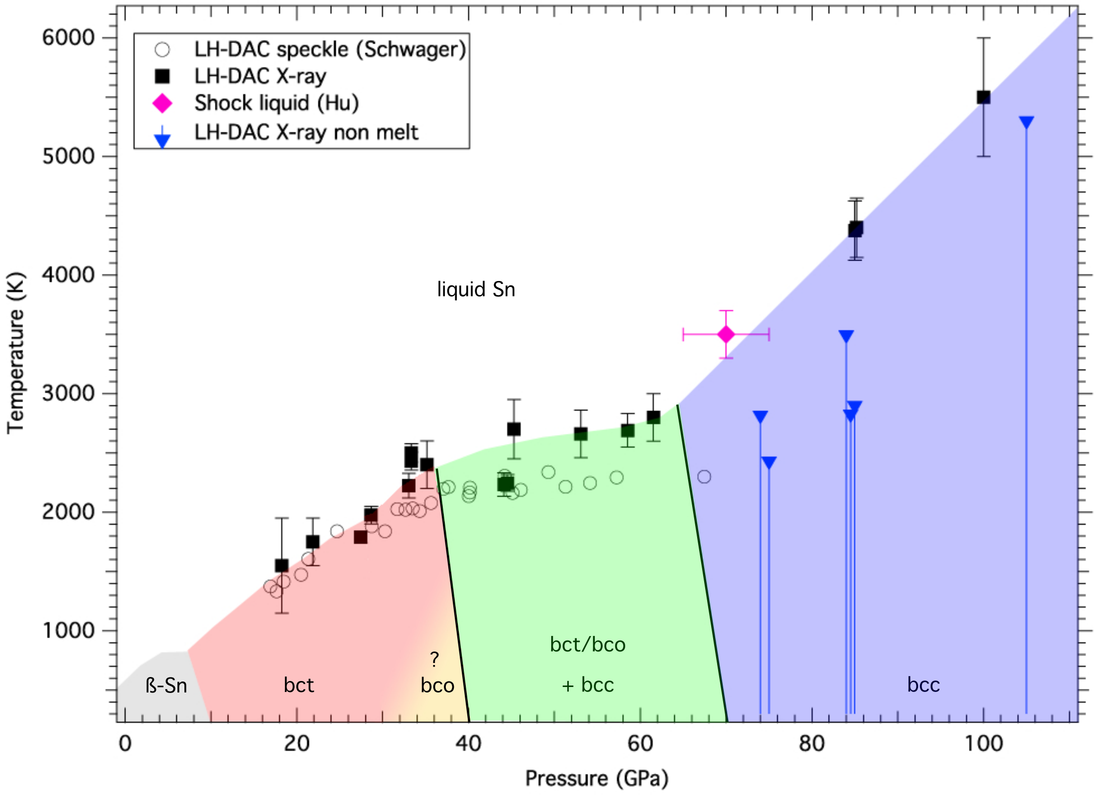

Figure 4.13 Phase diagram of Sn. The shaded yellow region represents a region of uncertainty since no quasi-hydrostatic experiments have been performed in this region above room temperature.

To investigate the dip followed by rise in the melting curve a literature search revealed similar melting behaviour for Xe (determined by the speckle technique) [88]. Above a certain pressure the melting points determined showed a deviation from the corresponding states theory (where the melting curve of the noble gases are scaled up from the melting curve of Ne. It was found that diffraction lines indexed to a *hcp* structure appear and coexist with the *fcc* structure over a wide pressure range starting between 3.7 GPa - 14 GPa and ending near P ~ 70 GPa. Throughout the pressure range the ratio of *hcp*/*fcc* increases until only the *hcp* structure exists. In the melting paper by Boehler *et al.* they employed a mixing model where they treat the onset of *hcp* structures as impurities in the crystal. Impurity atoms that exist in the host crystal actually lower the melting temperature with respect to the pure crystal. In the case of Sn this exists for Sn/Pb alloys, commonly used as soldering material, where the melting temperatures are lower than pure Sn. An expression exists that describes the change to the melting temperature, written as $T_m = T_0 (1 - x(1 - x))$ where T_0 is the temperature according to corresponding states model and x is the mole fraction associated with the impurity given by $x = (P - P_L)/(P_U-P_L)$, where P_U and P_L are the upper and lower limits of the coexistence region. The experimental observation of *hcp* and *fcc* lines can be explained by stacking faults that occur where changing from *ABCABC* stacking (*fcc*) to *ABABAB* stacking (*hcp*). The same authors performed total energy calculations for several close packed structures revealing the *fcc* and *hcp* are within numerical accuracy (± 1 mRy/atom) up to 50 GPa. This is a similar result to the difference in energy between *bct* and *bcc* Sn structures at room temperature [89]. Applying this model to Sn we can apply a model that spans the whole pressure range (up to 1 Mbar) and including the mixing regions of *bct/bco* and *bcc* as the upper and lower limits of this mixing model.

Sound velocity measurements by Hu *et al.* revealed two discontinuities in the longitudinal sound velocity occurring at 34 ± 2 GPa and 39 ± 2 GPa. These were assigned to the *bct* to *bcc* transition and to incipient melting respectively. They noted no kink in the bulk sound velocity for the discontinuity at 34 GPa, indicating that there is no significant volume change associated with the transition. Beyond 39 GPa, the bulk sound velocity drops towards 0 at P ~ 80 GPa. There is no liquid scattering observed in the whole region above 39 ± 2 GPa suggesting there is no solid – liquid coexist. Wu *et al.* suggested a shear induced plastic flow that occurs just below the melting temperatures for the case study of Ta [90]. In that paper, the authors observe the calculated shear stress of Ta decrease to a constant value of approximately 1.8 GPa just before the point at which the sample approaches the liquid (a shear stress of 0 GPa indicates a liquid sample). This relates directly to what is observed by Hu *et al.* where the sound speed velocity approaches the bulk speed above 40 GPa, where a decrease in shear strength is observed similar to Ta [81]. This suggests that the decrease in shear strength in Sn is not a solid-liquid coexist region, which is backed up by the X-ray diffraction results presented here that show no signs of liquid in this region, but in fact a consequence of plastic flow occurring due to deformations in the crystal. Based on our experimental work carried out at room temperature, new conclusions can be drawn from the Hu data. The first discontinuity could be associated with the subtle distortion from the *bct* to *bco* structure, which does not come with a noticeable change in volume (Chapter 3). The second discontinuity, though described as incipient melting, would therefore be due to the onset of *bcc* structures alongside *bco* structures, hence the jump in longitudinal sound velocity. In terms of the results presented here this would be the transition line between region I and region II. At this pressure and temperature, we observe no signs of liquid in the X-ray diffraction patterns. The incipient melting point determined by Mabire is significantly higher (49 GPa and 2300 K) [83] and matches well with static measurements [82], thus providing further evidence this kink is actually associated with the onset of region II. Above this pressure the longitudinal sound velocity gradually transforms to the bulk sound velocity in the range of 39 ± 2 GPa to ~ 70 ± 5 GPa. From Wu *et al.* this could be interpreted as plastic flow occurring during to crystal defects at the grain boundaries.

4.4. Conclusions

The melting curve of Sn to P > 1 Mbar has been presented, revealing unusual melting behaviour whereby the melting relation shows a plateau between 40 and 70 GPa followed by a sharp rise in slope at 70 GPa. The results link well with those presented in Chapter 3 on the room temperature compression of Sn to 137 GPa. The observed plateau in the melt curve occurs in the same pressure range as the observation of *bct/bco* and *bcc* structures from X-ray diffraction patterns collected at room temperature. The high temperature data collected shows coexistence of diffraction signatures associated with *bct* and *bcc* Sn in the 40-70 GPa pressure range up to the melting temperatures. The behaviour is analogous to that which has been suggested for Xe melting, where coexistence of *fcc* and *hcp* structures due to stacking faults can be fitted with a mixing model that treats the *hcp* structures as impurities in the *fcc* crystal, thus lowering the melting temperature. In the case of Sn, nanoscale domains develop as a consequence of the flat potential energy landscape, giving rise to X-ray diffraction signatures even at very high temperatures that cause a dip in the melting relation due to their enthalpy signatures.

Chapter 5. **Melting Curve of TaC**

5.1. Introduction

Tantalum carbide has the highest known ambient pressure melting point of any binary compound at $T_m \sim 4175$ K [91]. TaC_x samples are prepared by heating a mixture of tantalum and graphite powders under vacuum or inert atmosphere conditions. Heating is applied around 2000˚C using either conventional furnaces or using arc-melting apparatus [92]. The bonding between Ta and C atoms has a strong covalent component, making tantalum carbides extremely hard and brittle materials. Its high hardness (9-10 Mohs) and durability makes it a perfect material for use in industrial applications such as cutting tools and hard coatings. Despite the important industrial applications, there exists very little research on TaC at high pressures. Shock wave studies up to 1 Mbar found no signs of phase transitions up to 109 GPa [93]. There has been only one static high-pressure investigation at room temperature revealing the NaCl type structure (*Fm-3m*) existing at all pressures up to 76 GPa [94].

Interest in the melting of carbides has become of major significance in recent years since the melting of Ta using *in situ* X-ray diffraction techniques revealed the formation of TaC during laser-heating [95]. Lower melting points were found *via* the laser 'speckle' method, where continuous motion of the interference pattern created by an incident laser was inferred as melting at the sample surface [86]. The same group also performed heating experiments followed by SEM measurements to search for visual signs of melting [85]. These points differ by thousands of Kelvin at higher pressure to those determined by X-ray diffraction. The transformation of Ta to TaC begins at similar temperatures to the lower melting points for Ta. The only source of carbon available to form TaC in this case was from that of diamond anvils (Figure 5.2). By insulating the diamond anvils with Al_2O_3 coatings for X-ray diffraction experiments, no formation of carbide was observed and the high melting points matched well with those of theoretical studies by Taioli *et al.* [96]. It is therefore suggested that the lower melting points during speckle experiments could be a consequence of surface recrystallization due to formation of TaC. At ambient pressure, the introduction of carbon into the tantalum lattice lowers its melting point by ~ 300 K at 8 % atomic percent C (Figure 5.3) [97]. Melting from this type of composition could explain the reasons for lower melting points observed during speckle experiments.

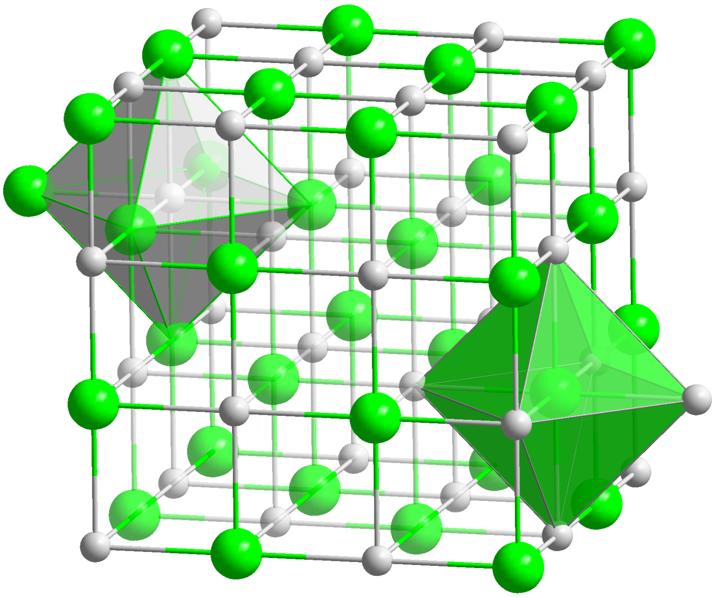

Figure 5.1 The NaCl-type structure of TaC (Fm-3m). Ta atoms are shown in green and C atoms are shown in grey.

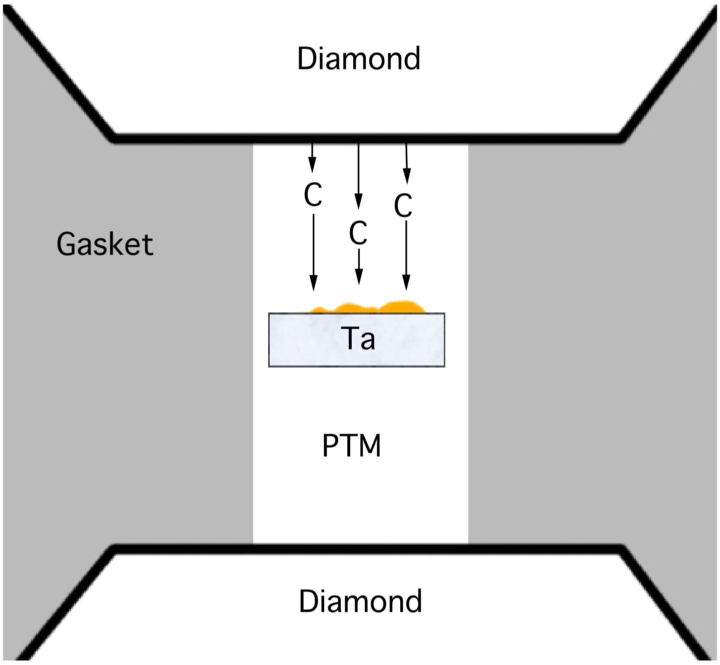

Figure 5.2 Schematic diagram showing the possible mechanism for formation of TaC (yellow) during Ta melting experiments. PTM of Al_2O_3 or MgO resulted in faster formation of the TaC. The only possible source of C comes from the diamond anvils.

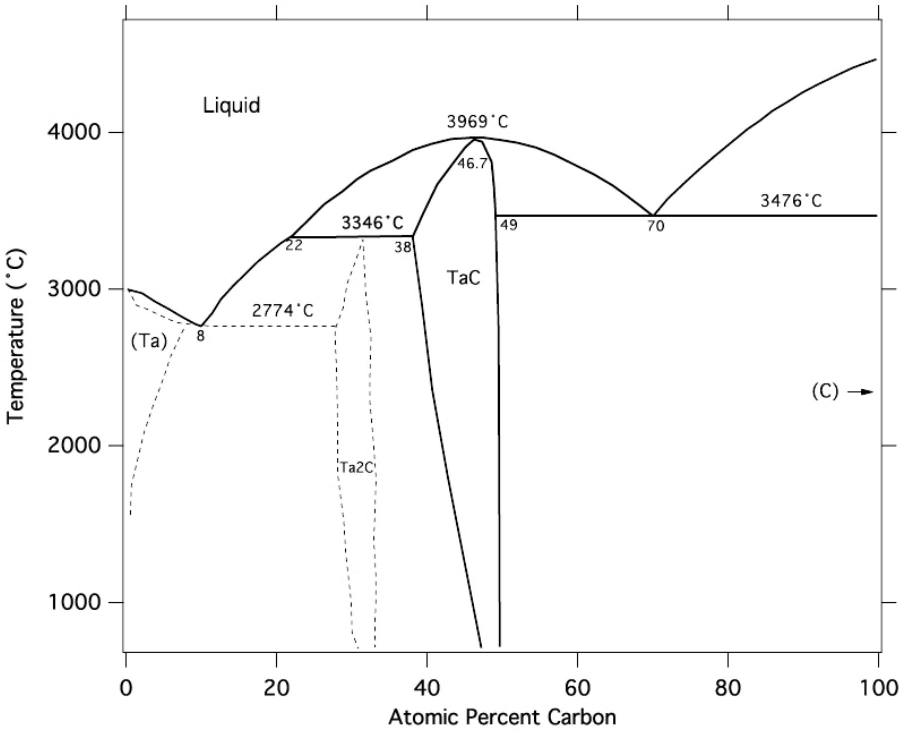

Figure 5.3 Tantalum - carbon composition phase diagram at ambient P. The melting temperatures of Ta with 8 % atomic carbon is lower by ~ 300˚C [97].

5.2. Experimental Methods

Experiments were carried out at the GSECARS beam line of the Advanced Photon Source, Argonne, USA. Powdered samples of TaC (Goodfellow 99.99%, Alfa Aesar 99.99%) were pre compressed into thin foils of ~ 5 µm thickness. Diamond anvils with 300 or 200 µm culets were used for reaching pressures up to 60 GPa. Re was used as gasket material, pre-indented to 30-40 µm before being drilled with 100 or 80 µm holes using a spark eroder. The gasket was indented to slightly larger thickness than traditionally used to ensure the TaC sample is surrounded my sufficient insulation, as high melting temperatures were expected. MgO and KBr were used as thermal insulation and as a pressure standard in addition to the equation of state of TaC [94]. Ruby was used in some cases to determine the pressure at UCL before travelling to the APS. Loadings were also performed at the APS without ruby in the sample chamber, as the EOS of MgO, KBr or TaC was sufficient to measure pressure *in situ*. Samples were compressed to the target pressure in a total of eight DACs and tested for heating at UCL. All samples were shown to heat from both sides with a strong hot spot.

The double-sided laser-heating system at GSECARS has recently been updated to bring it to the forefront of high pressure and high temperature experiments. Two random polarized, diode pumped fiber lasers were used with tunable power up to 200 W (1.064 µm). The shape of the laser beam was also adjusted using new optics. An initial input laser beam with a Gaussian profile is shaped to a Flat top format as the beam passes along the optical path before being focused at the sample with a hot spot width of ~ 10 µm. This creates a more stable laser heating spot that heats both side of the sample simultaneously with reduced temperature gradients.

Samples were compressed to the target pressure and heated from both sides by the two fibre optic lasers. The laser beams were focused to ~ 10 µm area, with the X-ray beam focused on the centre of the hotspot with a beam size of 5 x 5 µm at 40 keV (exposure times of 3-5 s were used). Temperatures were calculated by fitting grey body Planck functions to the thermal emission spectra. X-ray diffraction (XRD) patterns were integrated as a function of 2θ using FIT2D. The integrated XRD patterns *in situ* allowed observation of any chemical reaction occuring between the sample and the pressure-transmitting medium. Loss of peak intensity of the TaC and large increase in background / diffuse scattering were taken as the onset of melting.

5.3. Results and Discussion

The melting point of tantalum carbide was studied using *in situ* synchrotron X-ray diffraction combined with laser-heated diamond anvil cell techniques. The melt curve was investigated from a starting pressure of 4 GPa up to a maximum pressure of ~ 50 ± 1 GPa, attaining maximum melting temperatures of ~ 6100 ± 500 K. In every melting event I observe a significant jump in background as well as large decreases in peak intensity of the TaC reflections (Figure 5.4). Samples were heated from the desired pressure with XRD patterns collected at ~ 5 s intervals showing the crystalline structure of TaC until melting. Upon cooling to room temperature (RT), the pressure difference was never more than 1 GPa and in most cases showed no significant change in pressure.

Initially, MgO was used for thermal insulation due to its high melting points [5], however, we observed a reaction between the MgO and the TaC. During laser heating above temperatures of ~ 1600 K, new peaks appeared in the XRD patterns that grew in intensity with increasing time and laser power. Seven out of the eight loadings we had prepared were loaded with MgO as PTM and each DAC showed the new peaks developing at high temperature. This included two loadings that were performed in the glovebox in an inert atmosphere. There was no reaction between the TaC and KBr PTM in the final DAC and so all cells were reloaded at APS using dried KBr as PTM. We were able to identify the new peaks as a high temperature phase of Ta_2O_5 (*A12/m1*, spacegroup 12) [98]. Figure 5.5 shows a Le Bail refinement of this phase with a = 3.91(1) Å, b = 3.88(2) Å, c = 36.14(3) Å and ß = 95.09(3)˚.

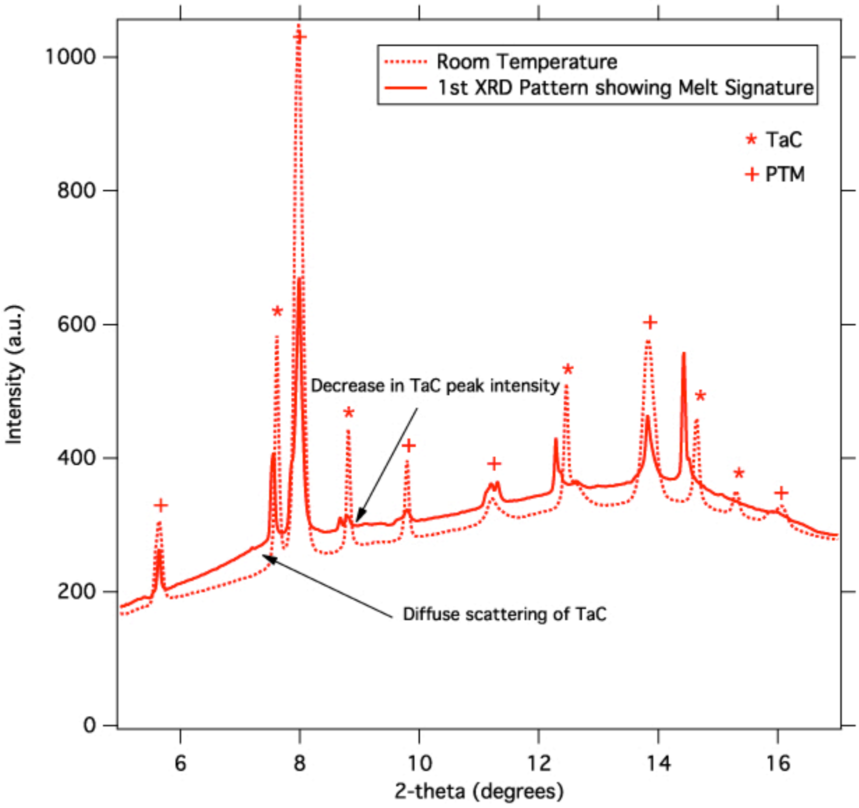

Figure 5.4 Comparison of X-ray diffraction patterns collected at room temperature (dashed black) and high temperature (red).

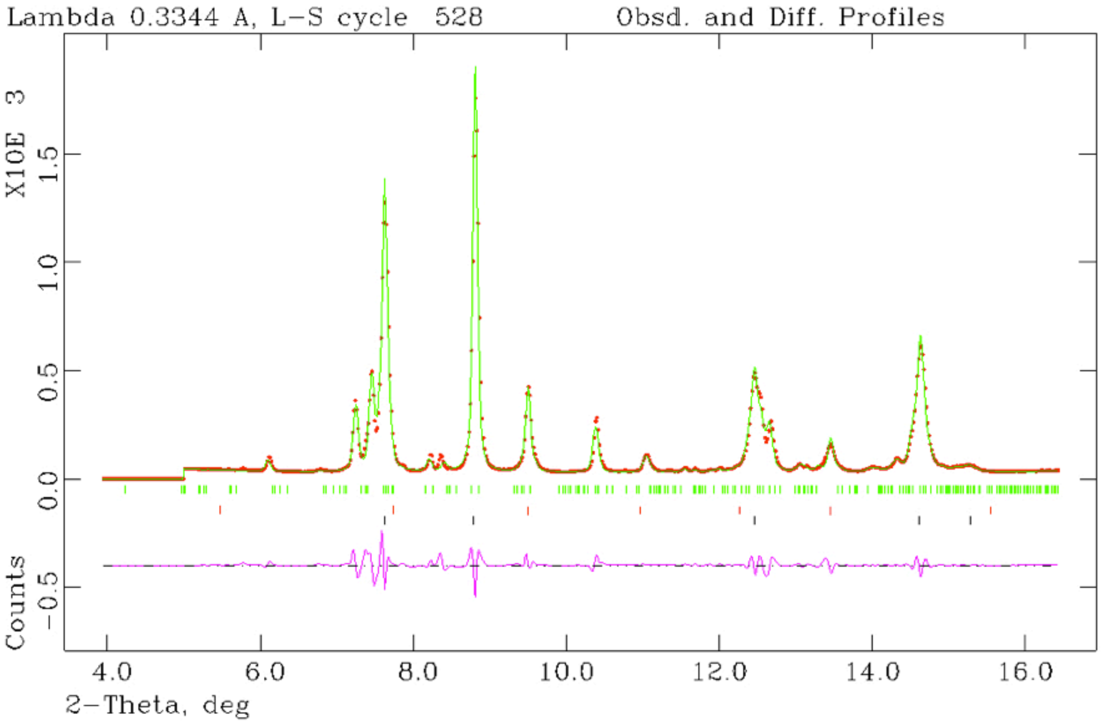

Figure 5.5 Le Bail refinement of TaC (blue ticks), MgO (red ticks) and Ta_2O_5 (green ticks). This transformation occurred at temperatures above T ~ 1600 K.

In all of the melting experiments I observe signs of melting from the KBr occurring before the melting of TaC. This was expected since TaC has the highest known ambient melting point of any element / binary compound, which is much higher than that of KBr. This did not effect the melting experiments, as I made sure there was sufficient KBr surrounding the TaC sample to protect the diamonds from the very high temperatures. The laser power was also ramped very quickly for higher temperature melting to ensure only a small amount of KBr melted to prevent sample migration. For the highest temperatures the laser power was set to a high laser power with the shutter closed. An XRD diffraction pattern was then collected at room temperature before starting a second scan with the laser shutter open. Thermal emission was collected rapidly (exposure times were less than 1 sec) during the 5 second X-ray exposure to determine the temperature. This rapid collection of data at specific laser powers (with temperatures remaining within 200-500 K) kept melting of the PTM to a minimum with the aim of looking for diffuse scattering of the TaC. The approximate melting temperatures of the KBr match well with the values given in the literature [99].

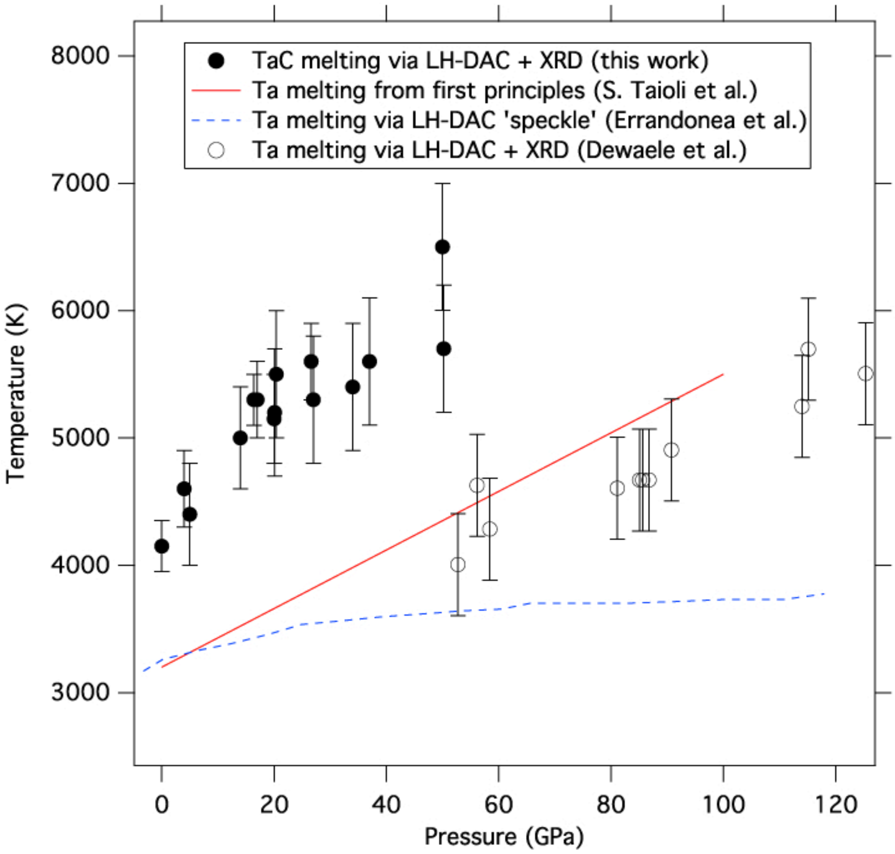

Figure 5.6 Melt curve of TaC. Also shown are the three melting curves for Ta from ab initio, speckle and X-ray diffraction.

Our melt data for TaC are shown in Figure 5.6 (black circles) alongside the melt curves of Ta from first principles (red line) [96], laser speckle (blue dash line) [86] and from X-ray diffraction (open circles) [95]. From ambient pressure there is a sharp and steady rise in melting temperature with dT/dP ~ 40 ± 7 K GPa^{-1}, in comparison to the melting curve of Ta from XRD techniques, which has a melting slope ~ 20 ± 2 K GPa^{-1}.

Figure 5.7 represents the possible tantalum – carbon phase diagram with melting data from Ta (X-ray), Ta (speckle), TaC (this work) and C all at P = 50 GPa. A tentative high pressure phase diagram has been constructed as a guide to the eye, but with no means for determining the composition phase diagram below the liquid. The yellow shaded region shows area of liquid for Ta, TaC and C at P = 50 GPa, with the lower melting points for 8 % and 70 % carbon content estimated from the 0 GPa phase diagram. The green shaded area is the liquid region at ambient pressure. Figure 5.7 provides a possible mechanism for the lower melting points of LH-DAC speckle measurements, with the melting point at 50 GPa transformed to represent melting from an 8 % atomic carbon composition.

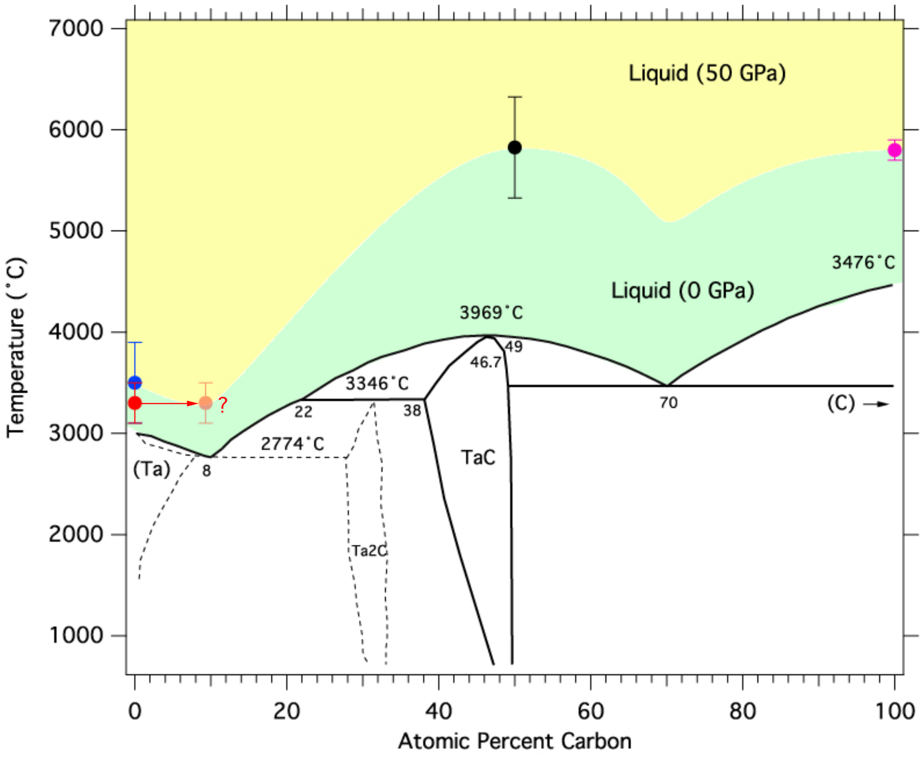

Figure 5.7 Possible phase diagram for the tantalum - carbon system at high pressure. The blue point is the high temperature X-ray melting points for Ta, the red point is the lower melting temperatures from speckle.

The formation of TaC in X-ray diffraction measurements was found to be fastest when MgO and Al_2O_3 were used as PTM. This could be due to the grain boundaries allowing diffusion of carbon from the diamonds. The new peaks that develop in the X-ray are not thought to be from Ta_2C as key reflections from this phase are missing. Interestingly, this reaction occurs below the Ta melting temperatures reported, suggesting the formation of tantalum carbide must follow a path along eutectic melting (Figure 5.7).

Following the lower melting temperature speckle measurements, further experiments were carried out by the same group using SEM as a diagnostic to look for visual signs of melting [85]. However, the identification of chemical reactions was only carried out visually using SEM and with no other analytical techniques (e.g. Energy Dispersive X-ray Spectroscopy). Melting is definitely observed as is clear from the observed molten sample but there is no *in situ* or *ex situ* chemical analysis carried out and so formation of TaC or even Ta_2C cannot be ruled out. Speckle measurements are heavily surface dependent and without proper analysis of the sample during or even following experiments there can be no guarantee that the observed shift in speckle motion or the molten sample following laser-heating is melting from the clean sample or from chemical reactions occurring in the sample chamber.

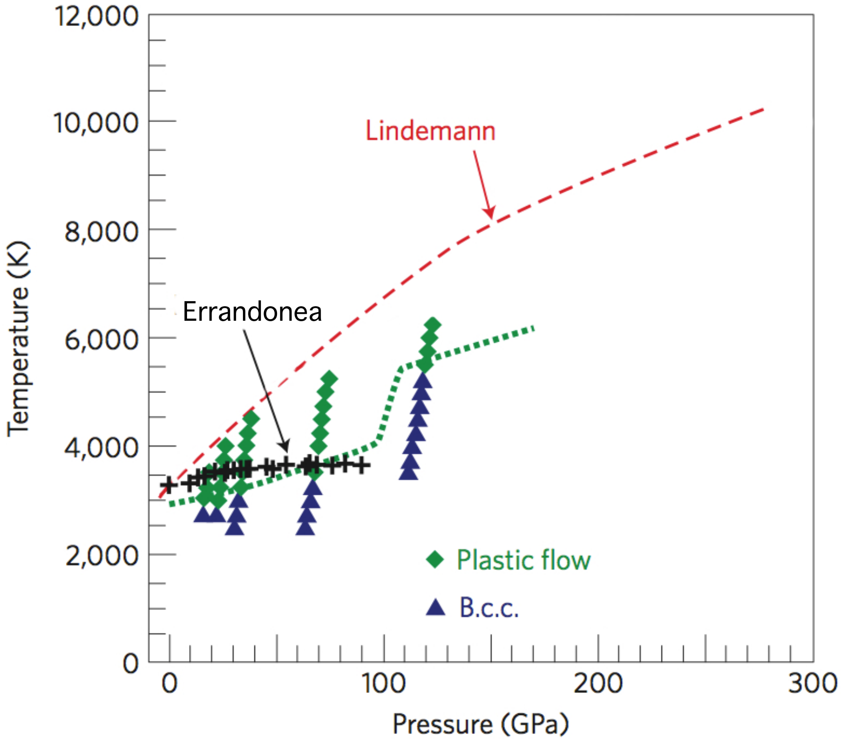

Figure 5.8 Melting curve of Ta revealing a region of plastic flow as determined by shear inducing calculations at high P-T by Wu et al.. The low melting points from speckle occur within a few hundred Kelvin of the onset of this plastic flow. From [90].

Ab initio calculations by Wu *et al*. reveal a thermal softening occurring just below the DAC melting temperature for Ta, that reveal a region of plastic flow as a consequence of severe strain in the system. The plastic flow begins as a transformation from an ordered *bcc* Ta lattice into a disordered viscous flow. The transition is shown in Figure 5.8 and is consistent with the DAC lower melting temperatures by Errandonea *et al.*.

5.4. Conclusions

The melting experiments performed here on TaC suggest high melting relations for the stoichiometric TaC composition. The melting relations show a high melting slope with $dT_m/dP = 40 \pm 7$ K GPa^{-1}, as compared to the Ta melting slope with $dT_m/dP \sim 20$ K GPa^{-1}, suggesting the lower DAC melting temperatures may be observing something other than melting of the sample. The speckle technique observes changes in the surface of the sample that may be due to chemical reactions occurring at the surface, or due to a plastic flow transition that occurs below the melting temperature as predicted by Wu *et al.*. The possible Ta – C phase diagram presented here (Figure 5.7) suggests that it is possible to form tantalum carbide below the melting temperature of Ta. Here the melting temperatures for stoichiometric TaC match well with the (higher temperature) melting relations for Ta and for C. The extremely high melting temperatures for TaC allow the potential application for indirect heating experiments in the DAC to be envisaged. Using TaC as an indirect heater, one can determine the melting temperature of other elements (e.g. Xe) that do not couple with the IR lasers directly and are predicted to have very high melting temperatures.

Chapter 6. **Melting of MgO**

6.1. Introduction

Magnesium oxide (MgO) has the rocksalt *Fm-3m* structure and constitutes approximately 37 % of the Earth's lower mantle at temperatures ranging between ~ 1000 – 4300 K at the core-mantle boundary [100]. Knowledge of the melting behaviour of MgO at high pressure and high temperature has major implications for the melting behaviour, phase relations and rheology of the Earth's lower mantle. However, the high P melting behaviour of MgO is still not been studied experimentally above above 35 GPa.

Ab initio MD simulations performed to date indicate the initial melting curve initially has a steep slope, achieving T_m ~ 4000 K by around 10 GPa, rising to T_m ~ 6000 K by 50 GPa [5]. However, this disagrees with the only experimental investigation carried out using LH-DAC techniques combined with CO_2 laser heating that reveal melting temperatures extending up to only ~ 4000 K at 50 GPa [3]. This is unacceptable for such an important compound. This chapter provides the first attempt at applying the techniques used for studying melting curves of elements and compounds using *in situ* synchrotron X-ray diffraction methods. These were some of the first experiments to be carried out at ID27 using the newly installed CO_2 laser for *in situ* heating of the sample.

6.2. Experimental Procedure

In order to carry out melting experiments of MgO the existing beamline at ID27 had to be modified to implement a CO_2 laser. I was directly involved in the installation of this and later applied for beamtime to study the melting of MgO. For direct heating of the MgO sample, a near IR CO_2 laser was used (10.6 µm wavelength). A CO_2 laser was installed onto the optics table at ID27 (Figure 6.1). The typical SiO_2 lenses used to focus IR lasers (e.g. Nd:YAG/Nd:YLF) heavily absorb the CO_2 laser radiation and cannot be used to focus the beam. Initially, a red diode laser is introduced along the same optical path as the CO_2 laser (red line in Figure 6.1). Most CO_2 lasers come equipped with such a laser and only require fine adjustments at distances > 1 m away from the CO_2 source. A piece of paper or fireblock is used to align the red diode > 1 m by marking the position of the CO_2 burn on the paper / fireblock and aligning the red diode laser to the burn. We performed this method of aligned the red diode to a maximum distance of 4 m away from the CO_2 source, which more than covered the optical path distance to the sample. An IR camera was used to aid the alignment of the laser beam. Once aligned to the CO_2 source, the red diode is used to position the path of the CO_2 laser beam to the sample. Corrections for the refractive index of diamond for the different laser wavelengths are performed to correct the focal distance. A correction lens that adjusts the focal point of the red diode laser to accommodate this refractive index correction can be used before the ZnSe lens, but must be removed during experiments. No such correction lens was used in these experiments.

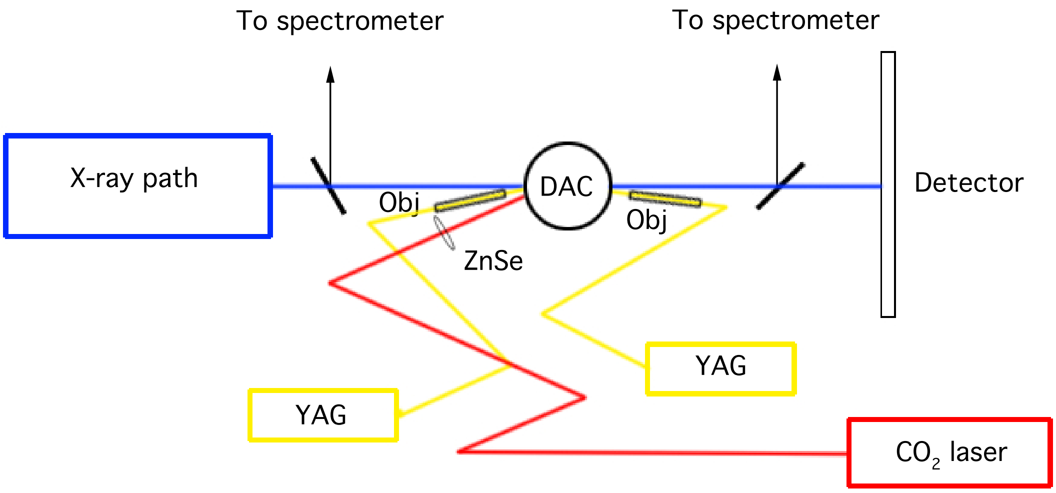

Figure 6.1 Schematic of the online CO_2 laser heating system at ID27.

The MgO sample must be surrounded by sufficient thermal insulation. However, careful considerations were taken to ensure the PTM was not a sufficiently high Z material, as the observed X-ray diffraction signature of the MgO, which has a lower Z number and weaker scattering, may be drowned out by that of the PTM. Of the potential alkali halides that are used in melting experiments, only LiF or NaCl were selected as PTM. LiF is the lowest Z material but also has a lower melting point than the NaCl [101]. If the *ab initio* melting curve is correct, then the melting temperatures will be towards 6000 K for higher pressure melting. Neither PTM has sufficiently high melting points to fully insulate the diamond anvils from the sample at these pressures and temperatures. For that reason the gasket holes needed to be larger than normal, to provide more insulation, though this would increase the quantity of PTM that contributes to the X-ray diffraction signature.

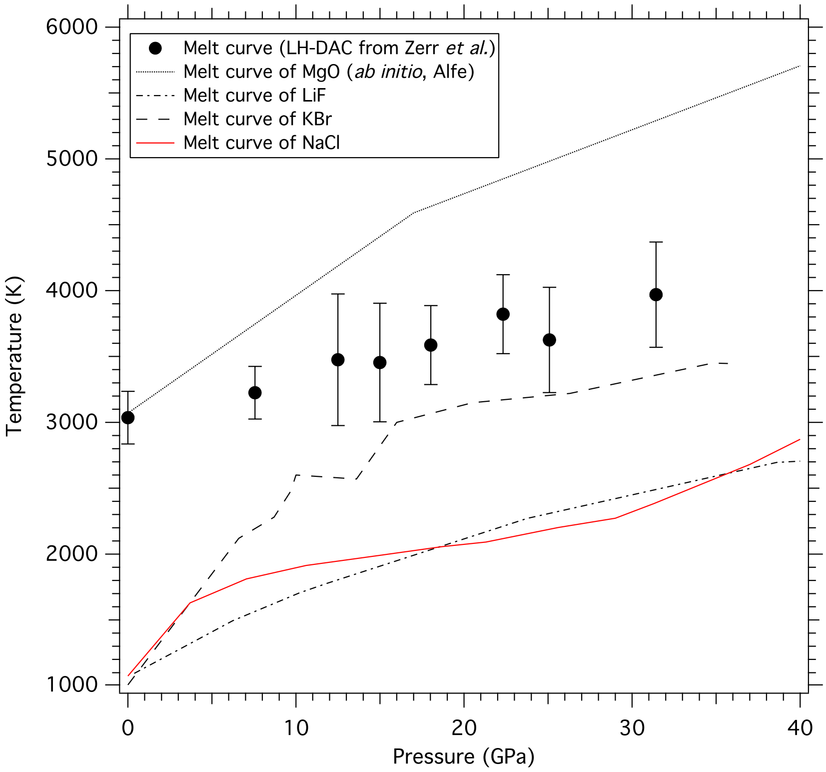

Figure 6.2 Melting curves of various PTM combined with experimental (solid circles) and ab initio (dots) results for MgO.

Melting experiments were carried out at beamline ID27 of the ESRF using the newly installed CO_2 laser heating system. Diamond anvil cells with 300 µm culets were used to obtain P < 50 GPa. Re gasket was used with thicker indents than usual to ensure enough insulation of the sample and diamond anvils at high temperatures. The thickness of the Re was between 40 and 50 µm for each DAC with a hole size of ~ 100-125 µm. MgO was pre dried in an oven at 600˚C for over 12 hours to remove any moisture, which could cause contamination. LiF and NaCl were also dried in an oven at 200˚C for 12 hours. The powdered samples were pre-indented into a disk (~ 15 x 15 μm^2) and loaded in a glovebox at UCL, with several glovebox loadings also performed at the ESRF. A small amount of ruby was added for initial P measurements, with final pressures determined from the MgO EOS [17].

Once loaded the DAC was placed onto the optics bench and the CO_2 laser was aligned with the MgO sample. The laser has a large spot size (> 50 µm) and couples with the sample directly, heating the whole sample area. Thermal emission measurements were taken *in situ* from a 2 x 2 µm^2 area to determine T whist X-ray measurements were taken from the same spot. The CO_2 laser was controlled manually from the experimental hutch, with the power increased at a variable rate depending on the T readout.

6.3. Results and Discussion

Powdered samples of MgO were loaded in the diamond anvil cell and taken to several different pressures before laser-heating with a CO_2 laser online at beamline ID27 of the ESRF. X-ray diffraction patterns were collected with 5 second exposure times and the crystalline state of the MgO sample was monitored as the laser power was increased (with gradual temperature rise). No signatures of melting were observed in any of the high-pressure runs. In all experiments, crystalline diffraction peaks were observed up to the highest recorded temperatures.

Figure 6.3 shows a series of diffraction patterns collected with increasing laser power. The highest temperature recorded was T = 3270 K before the temperature reached a plateau. At this point the surrounding thermal insulation (from the LiF) became too small and heat was removed by the diamond anvils. This was also observed visually by the optical camera viewing the sample area, which glowed brightly with a pulsing rhythm. Beyond this point there was no increase in temperature with increasing laser power and the experiment came to an end. The XRD patterns show only the LiF insulating material and the MgO and no reactions were observed.

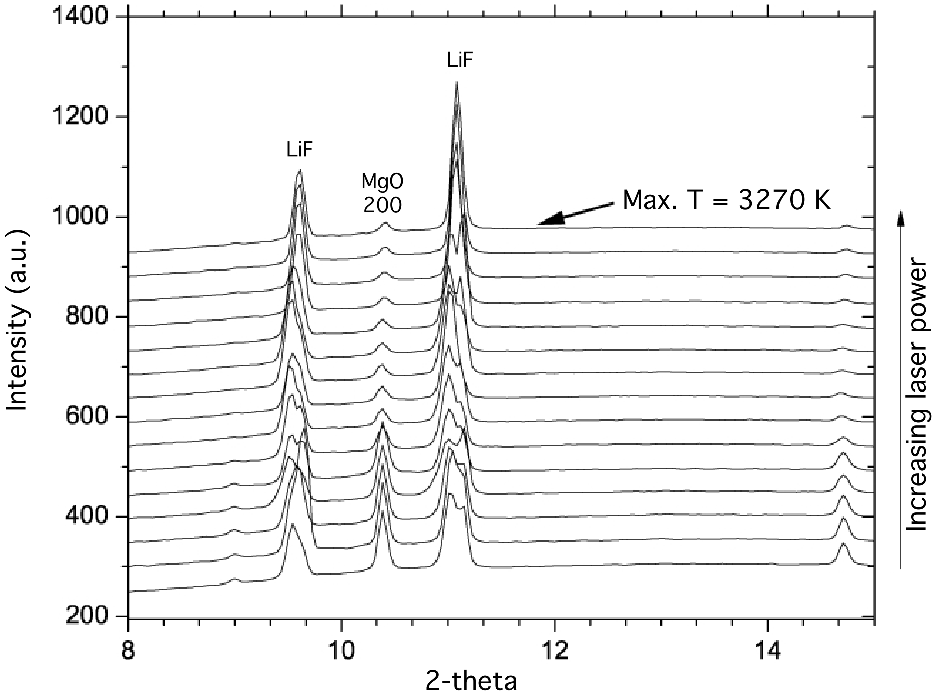

Figure 6.3 X-ray diffraction measurements collected up to a maximum temperature of T = 3270 K. No signs of melting from MgO were observed.

The non-melting data are shown in red in Figure 6.4 in addition to the experimental melting points determined by Zerr and Boehler, as well as theoretical melting by Alfe. The data presented here lie, within experimental error, directly on the melting curve determined by Zerr. These results therefore provide lower bounds for the melting temperature of MgO.

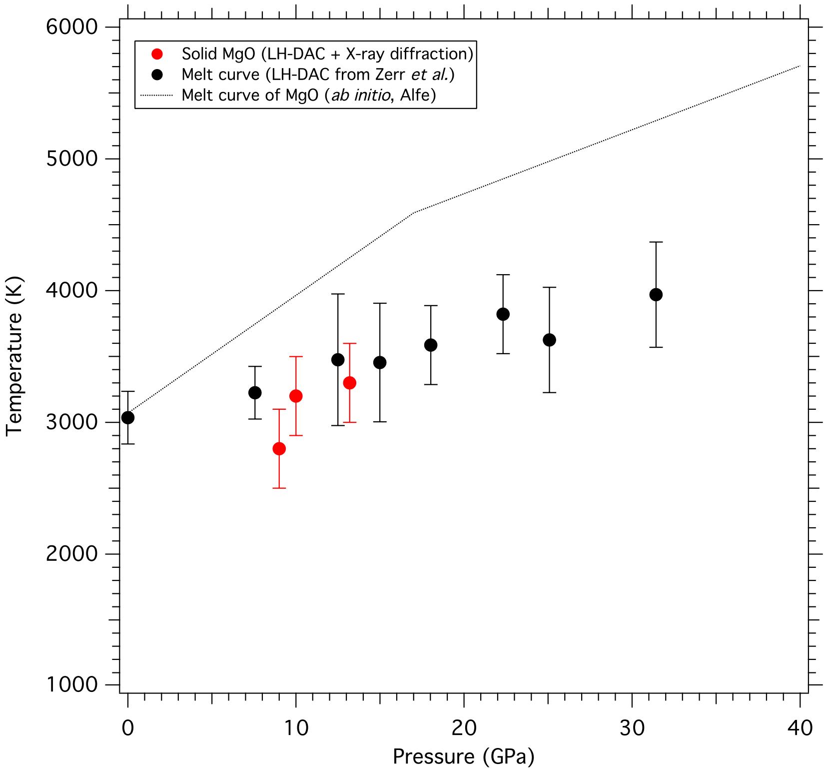

Figure 6.4 Melt curve of MgO revealing the three experimental runs where temperatures were close to the Zerr melting data. Only solid MgO was observed at these temperatures (red).

Since the start of this investigation there have been two key papers published at the end of 2012 (McWilliams *et al.*, Science [102]) and at the start of 2013 (Boates & Bonev, PRL [103]). Both papers investigate the phase diagram of MgO into the terapascal range (1 TPa = 1,000 GPa). McWillams *et al.* performed laser shock experiments that determined the shock temperature and shock velocity (U_s) directly, with the particle velocity (U_p) calculated from U_s. From the particle velocity the corresponding pressure and volume states were derived. Their results revealed an anomaly in the pressure-temperature curve with a minimum near 0.45 TPa and 8500 K (Figure 6.5). The higher melting temperatures shown in Figure 6.5 are supported by the theoretical calculations by Boates and Bonev [103]. DFT techniques combined with generalized gradient approximations and hybrid exchange-correlation functionals determined the B1-B2-Liquid triple point to be 0.364 TPa and 12,000 K. An extrapolation of the Zerr melt curve (shown in Figure 6.5 as upside down circles and reference 6) does not agree with the laser shock results or the Boates phase diagram. The theoretical melting curve by Alfé provides a closer match to those results (triangles and reference 7 in Figure 6.5).

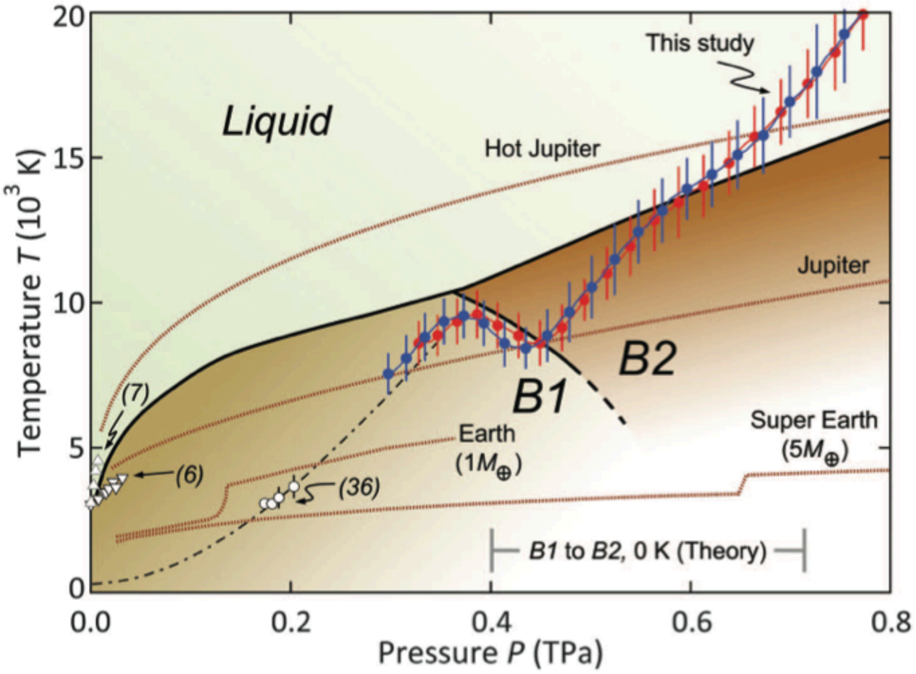

Figure 6.5: Phase diagram of MgO as determined by laser shock experiments (taken from [102]). Lower melting points by Zerr are shown as upside down triangles (6) [3]. Higher temperature melting points through theoretical calculations by Alfe are shown as triangles (7) [5]. Extrapolations of the experimental results by Zerr do not agree with the solid-liquid phase boundary inferred by these laser shocks.

6.4. Conclusion

I have carried out CO2 laser-heating at ID27, ESRF on MgO at high pressure, revealing solid MgO at temperatures < 3270 K ± 300 K that lie within experimental error of the Zerr melting curve [3]. Two recent investigations now support the previous theoretical predictions of high melting temperatures for MgO contradicting the only experimental investigation carried out by Zerr & Boehler [3]. The results in this chapter can only provide a lower bound on the melting temperature. However, solid MgO at these pressures and temperatures would be consistent with the new results reported by McWilliams *et al.* [102] and Boates and Bonev [103]. The new CO_2 laser-heating setup at ID27, ESRF has been shown to work consistently, providing time resolved X-ray diffraction alongside *in situ* CO_2 laser-heating and temperature measurements. The preliminary results shown here must be investigated further to established the first melting measurements using X-ray diffraction for this important mineral.

Chapter 7. **General Conclusions and Future Work**

In this thesis I have investigated the melting relations of three important materials: Sn, TaC and MgO (Figure 7.1). *In situ* synchrotron X-ray diffraction has been used as a definitive probe of the crystalline state of the sample during high pressure and high temperature experiments. The melting point using this technique is defined by the first observation of diffuse scattering in the X-ray diffraction patterns. The pressure and melting temperature are determined by ruby fluorescence / X-ray standards and by thermal emission from the sample respectively. By using X-ray diffraction as a diagnostic I have been able to investigate a large portion of P-T space to look for possible indications of new phase behavior in these materials.

Melting experiments on TaC revealed very high melting temperatures at moderate pressures. Comparing to the melting temperatures of Ta and C, I have been able to postulate a possible mechanism for the 'lower' melting temperatures observed by Errandonea *et al.* through carbide formation (Figure 5.7) [86]. However, the formation must occur first through the formation of Ta_2C composition in order to accommodate the lower melting temperatures, since stoichiometric TaC, as studied here, presents high melting temperatures. The melting relation of stoichiometric TaC increases steadily as observed for the 'higher' Ta melting relations [95]. The simulations by Wu *et al.* may also provide a reliable mechanism for the lower 'melting' temperatures, where the onset of a plastic flow region could explain the rapid changes in speckle motion. We observed no significant changes in the crystalline X-ray diffraction patterns at high temperature below the melting temperatures. These results are some of the highest melting temperatures observed in laser-heated diamond anvil cell experiments to date. The high melting points could have a big impact in the high pressure community, allowing indirect melting experiments to be performed on other materials such as Xe, which is predicted to have high melting temperatures where as experiments to date revealed a dip in the melting relation (W or Re was used as an indirect heater).

MgO has a melting curve predicted to exhibit extremely high melting temperatures [5]. However, only one experimental data set exists that actually show a lower melting slope [3]. The melting experiments performed here did not achieve melting of MgO, but do provide an upper bound on the solid region that sit close to the Zerr melting line. Recent experiments by McWilliams *et al.* and a theoretical study by Boates & Bonev have shown the phase diagram of MgO into the TPa region, with the B1-B2 transition in MgO highlighted. Both reveal a solid-liquid phase boundary that agrees with the previous theoretical papers, but do not agree with the experimental results for melting by Zerr and Boehler. These experiments were some of the first to use the online CO_2 laser-heating system at ID27, ESRF with *in situ* synchrotron X-ray diffraction and thermal emission measurements.

Future Work: The high melting temperatures predicted for MgO and their implications for the Earth's lower mantle composition and rheology result in the melting curve of MgO becoming increasingly important and attractive for new and state of the art X-ray diffraction experiments. The preliminary results in this thesis (Chapter 6) lie very close to the only experimental melting results and actually reveal solid diffraction of MgO at the highest temperatures. With rapid CO_2 laser heating and further insulation between the sample and the diamond anvils, this experiment could be investigated further. Indirect heating of a MgO sample could be explored as well as direct laser heating from a CO_2 laser, with advanced diagnostics of the melting event.

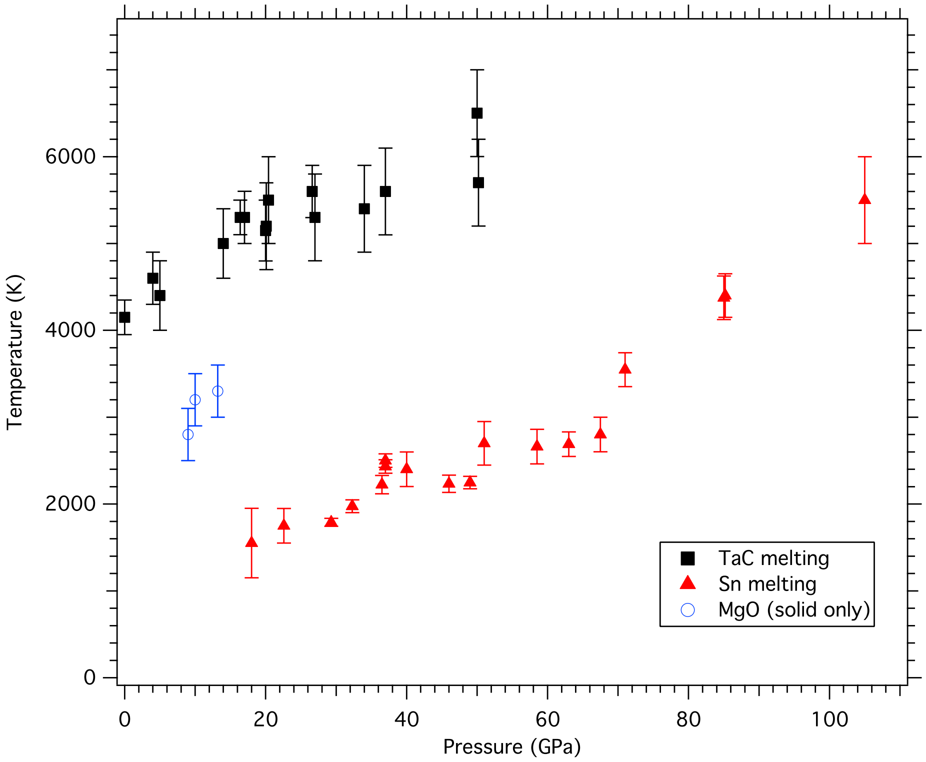

Figure 7.1 Melting curves of TaC and Sn, with 3 points for MgO that show lower bounds on the melting curve.

The melting of Sn to > 1 Mbar revealed an unusual dip in the melting relation between 40 and 70 GPa. At P ~ 1 Mbar T_m reached ~ 5500 ± 500 K. Between 40-70 GPa coexistence of bct and bcc polymorphs are observed in the X-ray diffraction patterns, even at high temperature. The sharp rise in melting relation above 70 GPa immediately open the way for further shock experiments. A laser shock experiment into the liquid followed by a ramp wave could possibly find recrystallization into crystalline Sn. Laser ramp compression can also probe a large region of P-T space below the melt curve to look for signs of new phases. Without these new results one would assume such experiments would only be able to probe the liquid state of Sn (from extrapolations of previous melt curves).

I have also performed a room temperature compression experiment on Sn up to 137 GPa that revealed a previously unreported distortion of the *bct* Sn (*I4/mmm*) structure to an orthorhombic structure (*bco* Sn: *Immm*). These results also reveal coexistence occurring in the same range as a dip in melting relation is observed. The flat potential energy landscape, discovered by Christensen [73], allows nanoscale domains to develop within the sample at these pressures (between 40 and 70 GPa) that persist at high temperature and can cause the dip in the melting curve.

Future Work: Room temperature compression of Sn using a quasi-hydrostatic pressure environment revealed a previously unreported structure occurring in Sn at 32 GPa (Chapter 3). All high temperature experiments in this thesis (Chapter 4, 5 and 6) have been carried out using pressure-transmitting medium that are non-hydrostatic at high pressure (e.g. NaCl, KBr). To investigate the new orthorhombic structure (*Immm*) of Sn at 32 GPa at high temperature would give an indication of a possible Clapeyron slope and a phase boundary between the bct (*I4/mmm*) phase. This can only be carried out in the best hydrostatic conditions possible using He PTM. Isothermal compression at several different temperatures may be able to map the phase behavior of Sn across a wide pressure range below the melting curve and would back up our observation of coexistence of bct/bco & bcc Sn X-ray signatures at high temperature below melt.

References:

[1] P. W. Bridgman, *The Physics of High Pressure* (1958).

[2] G. J. Piermarini and S. Block, Review of Scientific Instruments **46**, 973 (1975).

[3] A. Zerr and R. Boehler, (1994).

[4] J. A. Akins, S. N. Luo, P. D. Asimow, and T. J. Ahrens, Geophys. Res. **31**, L14612 (2004).

[5] D. Alfè, Physical Review Letters **94**, 235701 (2005).

[6] R. Boehler, Reviews of Geophysics-Richmond Virginia Then Washington- **38**, 221 (2000).

[7] A. Dewaele, M. Mezouar, N. Guignot, and P. Loubeyre, Physical Review B **76**, 144106 (2007).

[8] D. Santamaría-Pérez, M. Ross, D. Errandonea, G. D. Mukherjee, M. Mezouar, and R. Boehler, J. Chem. Phys. **130**, 124509 (2009).

[9] J. C. Jamieson, A. W. Lawson, and N. D. Nachtrieb, Review of Scientific Instruments **30**, 1016 (1959).

[10] P. F. McMillan, Nature Materials **4**, 715 (2005).

[11] H. K. Mao, Y. Wu, L. C. Chen, J. F. Shu, and A. P. Jephcoat, Journal of Geophysical Research **95**, 21737 (1990).

[12] A. L. Ruoff, H. Luo, C. Vanderborgh, and Y. K. Vohra, Review of Scientific Instruments **63**, 4342 (1992).

[13] R. Boehler and K. De Hantsetters, High Pressure Research **24**, 391 (2004).

[14] H. K. Mao, R. J. Hemley, Y. Wu, A. P. Jephcoat, L. W. Finger, C. S. Zha, and W. A. Bassett, Phys. Rev. B. **60**, 2649 (1988).

[15] A. Dewaele and P. Loubeyre, High Pressure Research **27**, 419 (2007).

[16] P. M. Bell, *Degrees of Hydrostaticity in He, Ne, and Ar Pressure-Transmitting Media* (Carnegie Inst. Washington, 1981).

[17] P. I. Dorogokupets and A. Dewaele, High Pressure Research **27**, 431 (2007).

[18] A. Dewaele, A. Belonoshko, G. Garbarino, F. Occelli, P. Bouvier, M. Hanfland, and M. Mezouar, Phys. Rev. B. **85**, 013905 (2009).

[19] C. S. Zha and W. A. Bassett, Review of Scientific Instruments **74**, 1255 (2003).

[20] S. T. Weir, D. D. Jackson, S. Falabella, G. Samudrala, and Y. K. Vohra, Review of Scientific Instruments **80**, 013905 (2009).

[21] W. A. Bassett, A. H. Shen, M. Bucknum, and I. M. Chou, Review of Scientific Instruments **64**, 2340 (1993).

[22] O. Narygina, E. McBride, G. Stinton, and M. McMahon, Physical Review B **84**, 054111 (2011).

[23] R. Boehler and A. Chopelas, Geophys. Res. **18**, 1147 (1991).

[24] D. L. Decker, J. App. Phys. **42**, 3239 (1971).

[25] D. L. Decker and J. D. Barnett, J. App. Phys. **41**, 833 (1970).

[26] D. L. Decker and J. D. Barnett, Journal of Physical and Chemical Reference Data **1**, 773 (1972).

[27] T. H. Maiman, Nature **187**, 493 (1960).

[28] M. E. Innocenzi, R. T. Swimm, M. Bass, R. H. French, A. B. Villaverde, and M. R. Kokta, J. App. Phys. **67**, 7542 (1990).

[29] J. D. Barnett, S. Block, and G. J. Piermarini, Review of Scientific Instruments **44**, 1 (1973).

[30] H. Mao, P. M. Bell, J. W. Shaner, and D. J. Steinberg, J. App. Phys. **49**, 3276 (1978).

[31] H. Mao and J. Xu, J. Geophys. Res (1986).

[32] R. J. Hemley, C. S. Zha, A. P. Jephcoat, H. K. Mao, L. W. Finger, and D. E.

Cox, Physical Review B **39**, 11820 (1989).
[33] K. Syassen, High Pressure Research (2008).
[34] A. C. Ugural and S. K. Fenster, *Advanced Strength and Applied Elasticity*, 4(null) ed. (Prentice Hall, 2003).
[35] P. Vinet and J. Ferrante, Geophys. Res. **92**, 9319 (1987).
[36] F. Birch, Physical Review **71**, 809 (1947).
[37] A. Dewaele, P. Loubeyre, and M. Mezouar, Physical Review B **70**, 094112 (2004).
[38] E. Soignard, High Pressure - High Temperature Synthesis and Studies of Nitride Materials, University College London, 2003.
[39] W. L. Bragg, Proc. Cambridge Phil. Soc **17**, 43 (1913).
[40] M. Von Laue, Ann. Physik **41**, (1912).
[41] A. Dadashev, M. P. Pasternak, G. K. Rozenberg, and R. D. Taylor, Review of Scientific Instruments **72**, 2633 (2001).
[42] D. E. Baynham and B. E. Wyborn, IEEE Transactions on Magnetics **17**, 1595 (1981).
[43] M. Kunz, A. A. MacDowell, W. A. Caldwell, D. Cambie, R. S. Celestre, E. E. Domning, R. M. Duarte, A. E. Gleason, J. M. Glossinger, N. Kelez, D. W. Plate, T. Yu, J. M. Zaug, H. A. Padmore, R. Jeanloz, A. P. Alivisatos, and S. M. Clark, J. Synchrotron Rad. **12**, 650 (2005).
[44] E. Schultz, M. Mezouar, W. Crichton, S. Bauchau, G. Blattmann, D. Andrault, G. Fiquet, R. Boehler, N. Rambert, B. Sitaud, and P. Loubeyre, High Pressure Research **25**, 71 (2005).
[45] V. B. Prakapenka, A. Kubo, A. Kuznetsov, A. Laskin, O. Shkurikhin, P. Dera, M. L. Rivers, and S. R. Sutton, High Pressure Research **28**, 225 (2008).
[46] A. P. Hammersley, S. O. Svensson, M. Hanfland, A. N. Fitch, and D. Häusermann, International Journal of High Pressure Research **14**, 235 (1996).
[47] W. Kraus and G. Nolze, J Appl Cryst **29**, 301 (1996).
[48] A. Larson, Los Alamos National Laboratory (1994).
[49] B. Toby, Journal of Applied Crystallography (2001).
[50] D. Louaer, Journal of Applied Crystallography **24**, 987 (1991).
[51] P. E. Werner, L. Eriksson, and M. Westdahl, Journal of Applied Crystallography **18**, 367 (1985).
[52] A. Altomare, C. Giacovazzo, A. Guagliardi, G. G. Moliterni, R. Rizzi, and P. E. Werner, Journal of Applied Crystallography **33**, 1180 (2000).
[53] R. A. Young, *The Rietveld Method* (Oxford University Press, Oxford, 1995).
[54] H. M. Rietveld, Journal of Applied Crystallography **2**, 65 (1969).
[55] H. Olijnyk and W. B. Holzapfel, Journal De Physique **C8**, 153 (1984).
[56] A. Kuznetsov, V. Dmitriev, L. Dubrovinsky, V. Prakapenka, and H. P. Weber, Solid State Commun. **122**, 125 (2002).
[57] C. A. Vanderborgh, Y. K. Vohra, H. Xia, and A. L. Ruoff, Physical Review B **41**, 7338 (1990).
[58] A. Mujica, A. Rubio, A. Munoz, and R. J. Needs, Reviews of Modern Physics **75**, 863 (2003).
[59] M. J. P. Musgrave, Proceedings of the Royal Society of London. Series a, Mathematical and Physical Sciences **272**, 503 (1963).
[60] H. W. Kroto, J. R. Heath, S. C. O'Brien, R. F. Curl, and R. E. Smalley, Nature (1985).
[61] A. Jorio, G. Dresselhaus, and M. S. Dresselhaus, Topics in Applied Physics **111**, (2008).
[62] N. E. Christensen, S. Satpahy, and Z. Pawlowska, Physical Review B **34**, (1986).

[63] J. C. Jamieson, Report at the AIME Meetings, Dallas (1963).
[64] D. Barnett, V. Bean, and T. Hall, J. App. Phys. **37**, 875 (1966).
[65] M. Liu and L. G. Liu, High Temp-High Press **18**, 79 (1986).
[66] M. Liu and L.-G. Lui, High Temp-High Press **18**, 79 (1986).
[67] S. Desgreniers, Y. K. Vohra, and A. L. Ruoff, Physical Review B **39**, 10359 (1989).
[68] Y. Yao and D. D. Klug, Solid State Commun. **151**, 1873 (2011).
[69] A. Salamat, G. Garbarino, A. Dewaele, P. Bouvier, S. Petitgirard, C. Pickard, P. McMillan, and M. Mezouar, Physical Review B **84**, 140104 (2011).
[70] C. J. Pickard and R. J. Needs, J. Phys.: Condens. Matter **23**, 053201 (2011).
[71] J. Liu, T. Sekine, and T. Kobayashi, Solid State Communications **137**, 21 (2006).
[72] *International Tables for Crystallography* (2005).
[73] N. E. Christensen and M. Methfessel, Physical Review B **48**, 5797 (1993).
[74] J. D. Dudley and H. T. Hall, Physical Review **118**, 1211 (1960).
[75] R. A. Stager, A. S. Balchan, and H. G. Drickamer, J. Chem. Phys. **37**, 1154 (1962).
[76] J. D. Barnett, R. B. Bennion, and H. T. Hall, Science **141**, (1963).
[77] *Solids Under Pressure* (McGraw-Hill Book Company, Inc, 1963).
[78] S. Bernard and J. Maillet, Physical Review B **66**, 012103 (2002).
[79] X. Feng and C. Ling-Cang, Chinese Physics B **18**, 2898 (2009).
[80] P. L. Hereil and C. Mabire, J. Phys. IV France **10**, Pr9 (2000).
[81] (2009).
[82] B. Schwager, M. Ross, S. Japel, and R. Boehler, J. Chem. Phys. **133**, 084501 (2010).
[83] C. Mabire and P. L. Hereil, J. Phys. IV France **10**, Pr9 (2000).
[84] R. Briggs, D. Daisenberger, A. Salamat, G. Garbarino, M. Mezouar, M. Wilson, and P. F. McMillan, J. Phys.: Conf. Ser. **377**, 012035 (2012).
[85] J. Ruiz-Fuertes, A. Karandikar, R. Boehler, and D. Errandonea, Physics of the Earth and Planetary Interiors **181**, 69 (2010).
[86] D. Errandonea, B. Schwager, R. Ditz, C. Gessmann, R. Boehler, and M. Ross, Physical Review B **63**, 132104 (2001).
[87] S. T. Weir, M. J. Lipp, S. Falabella, G. Samudrala, and Y. K. Vohra, J. Appl. Phys. **111**, 123529 (2012).
[88] R. Boehler, M. Ross, P. Söderlind, and D. Boercker, Physical Review Letters **86**, 5731 (2001).
[89] N. E. Christensen, Solid State Communications **85**, 151 (1993).
[90] C. J. Wu, P. Söderlind, J. N. Glosli, and J. E. Klepeis, Nature Materials **8**, 223 (2009).
[91] H. Xiang, Y. Xu, and L. Zhang, Scripta Materiali (2006).
[92] E. Rudy, C. E. Brukl, and S. Windisch, Journal of American Ceramic Society **51**, 239 (1968).
[93] S. P. Marsh, LASL Shock Hugoniot Data (1980).
[94] H. Liermann, A. Singh, B. Manoun, S. K. Saxena, and C. S. Zha, International Journal of Refractory Metals and Hard Materials **23**, 109 (2005).
[95] A. Dewaele, M. Mezouar, N. Guignot, and P. Loubeyre, Physical Review Letters **104**, 255701 (2010).
[96] S. Taioli, C. Cazorla, M. Gillan, and D. Alfè, Physical Review B **75**, 214103 (2007).
[97] H. Okamoto, J. Phase Equilbria **19**, 88 (1998).
[98] X. Q. Liu, X. D. Han, Z. Zhang, L. F. Ji, and Y. J. Jiang, Acta Materialia **55**, 2385 (2007).

[99] R. Boehler, M. Ross, and D. B. Boercker, Phys. Rev. B **53**, (1996).
[100] *Earth's Interior* (1999).
[101] R. Boehler, M. Ross, and D. B. Boercker, Physical Review Letters **78**, 4589 (1997).
[102] R. S. McWilliams, D. K. Spaulding, J. H. Eggert, P. M. Celliers, D. G. Hicks, R. F. Smith, G. W. Collins, and R. Jeanloz, Science **338**, 1330 (2012).
[103] B. Boates and S. A. Bonev, Physical Review Letters **110**, 135504 (2013).